

# **IMPROVED NUMERICAL METHODS FOR TURBULENT VISCOUS RECIRCULATING FLOWS AEROTHERMAL MODELING PHASE II Final Report**

by K. C. Karki, S. V. Patankar,  
A. K. Runchal, and H. C. Mongia

**ALLISON GAS TURBINE DIVISION**  
General Motors Corporation

Prepared for  
**NATIONAL AERONAUTICS  
AND  
SPACE ADMINISTRATION**



**NASA LEWIS RESEARCH CENTER**  
**Contract NAS3-24350**

(NASA-CR-182169) IMPROVED NUMERICAL METHODS  
FOR TURBULENT VISCOUS FLOWS AEROTHERMAL  
MODELING PROGRAM, PHASE 2 Final Report  
(Electric Diesel Allison) 93 p CSCL 20D

N89-12010

Unclas  
G3/34 0170265



1. Report No. CR-182169		2. Government Accession No.		3. Recipient's Catalog No.	
4. Title and Subtitle Improved Numerical Methods for Turbulent Viscous Flows Aerothermal Modeling Program Phase II				5. Report Date June 1988	
				6. Performing Organization Code	
7. Author(s) K. C. Karki, S. V. Patankar, A. K. Runchal, and H. C. Mongia				8. Performing Organization Report No. EDR 13519	
9. Performing Organization Name and Address Allison Gas Turbine Division General Motors Corporation P.O. Box 420 Indianapolis, IN 46206-0420				10. Work Unit No.	
				11. Contract or Grant No. NAS3-24350	
12. Sponsoring Agency Name and Address National Aeronautics and Space Administration Lewis Research Center 21000 Brookpark Rd, Cleveland, OH 44135				13. Type of Report and Period Covered Final Report	
				14. Sponsoring Agency Code	
15. Supplementary Notes NASA Program Manager: Russel W. Claus					
16. Abstract <p>This report describes the details of a study, sponsored by NASA, to develop accurate and efficient numerical schemes to predict complex flows.</p> <p>In this program several discretization schemes were evaluated using simple test cases. This assessment led to the selection of three schemes for an in-depth evaluation based on two-dimensional flows. The scheme with the superior overall performance was incorporated in a computer program for three-dimensional flows.</p> <p>To improve the computational efficiency, the selected discretization scheme was combined with a direct solution approach in which the fluid flow equations are solved simultaneously rather than sequentially.</p>					
17. Key Words (Suggested by Author(s)) Numerical diffusion, discretization schemes, direct method, viscous flows				18. Distribution Statement	
19. Security Classif. (of this report) Unclassified		20. Security Classif. (of this page) Unclassified		21. No. of Pages 86	
				22. Price*	



# TABLE OF CONTENTS

<u>Section</u>	<u>Title</u>	<u>Page</u>
I	Introduction . . . . .	3
	1.1 Objectives . . . . .	3
	1.2 Approach . . . . .	3
	1.3 Outline of the Report . . . . .	3
II	Description of the Selected Discretization Schemes and Solution Algorithm . . . . .	5
	2.1 Finite Volume Method . . . . .	5
	2.2 Discretization Schemes . . . . .	6
	2.2.1 Power-Law Differencing Scheme (PLDS) . . . . .	6
	2.2.2 Locally Analytic Differencing Scheme (LOADS) . . . . .	8
	2.2.3 Linear Flux-Spline Scheme . . . . .	8
	2.2.4 Cubic Flux-Spline Scheme . . . . .	10
	2.2.5 Controlled Numerical Diffusion with Internal Feedback (CONDIF) . . . . .	10
	2.2.6 Mass-Weighted Skew Upwind Differencing Scheme (MWSUDS) . . . . .	11
	2.3 Preliminary Evaluation of the Schemes . . . . .	13
	2.3.1 Uniform Flow in a Pipe with a Heat Source . . . . .	13
	2.3.2 Solid Body Rotation with Logarithmic Temperature Distribution . . . . .	15
	2.3.3 Recirculating Flow with a Prescribed Heat Source . . . . .	16
	2.4 Summary . . . . .	19
	2.5 Solution of the Fluid Flow Equations . . . . .	19
III	Description of Selected Discretization Schemes . . . . .	21
	3.1 Linear Flux-Spline Scheme . . . . .	21
	3.1.1 One-Dimensional Convection-Diffusion . . . . .	21
	3.1.2 Discretization Equation for $\phi$ . . . . .	24
	3.1.3 Extension to Multi-Dimensional Situations . . . . .	25
	3.1.4 Solution Procedure . . . . .	26
	3.1.5 Fluid Flow Calculations . . . . .	27
	3.1.6 Notes on Computer Implementation . . . . .	27
	3.2 Cubic Flux-Spline Scheme . . . . .	29
	3.2.1 One-Dimensional Convection Diffusion . . . . .	29
	3.2.2 Discretization Equation in Two Dimensions . . . . .	33
	3.2.3 Solution Procedure . . . . .	34
	3.3 Controlled Numerical Diffusion with Internal Feedback (CONDIF) . . . . .	35
	3.3.1 Central Difference Scheme . . . . .	35
	3.3.2 Alternate Representation of CDS . . . . .	37
	3.3.3 Derivation of CONDIF Scheme . . . . .	38

## TABLE OF CONTENTS (CONT)

<u>Section</u>	<u>Title</u>	<u>Page</u>
IV	Evaluation of Selected Schemes . . . . .	40
4.1	Two-Dimensional Test Cases . . . . .	40
4.1.1	Scalar Transport . . . . .	40
4.1.2	Laminar Flows . . . . .	44
4.1.3	Turbulent Flows. . . . .	50
4.2	Summary of the Two-Dimensional Test Cases . . . . .	58
4.3	Selection of a Scheme for Three-Dimensional Flows . . . . .	58
4.4	Three-Dimensional Test Cases . . . . .	59
4.4.1	Laminar Flow . . . . .	59
4.4.2	Turbulent Three-Dimensional Jet-Induced Flow in a Duct . . . . .	61
4.5	Summary of Three-Dimensional Test Cases . . . . .	70
V	Direct Solution Strategy for Fluid Flow Calculations . . . . .	73
5.1	Description of the Method . . . . .	73
5.2	Treatment of the Turbulence Quantities . . . . .	75
5.3	Performance of the Algorithm . . . . .	75
5.4	Plane-by-Plane Marching Procedure for 3-D Flows . . . . .	77
5.5	Evaluation of the Plane-by-Plane Solution Technique . . . . .	78
5.5.1	Three-Dimensional Sudden Expansion . . . . .	78
5.5.2	Flow in a Box with Transverse Jets . . . . .	80
5.6	Cost Comparison . . . . .	80
5.7	Note on the Use of Flux-Spline Scheme . . . . .	80
VI	Concluding Remarks . . . . .	83
6.1	Summary of the Present Work . . . . .	83
6.1	Recommendations for Further Work . . . . .	83
	References . . . . .	85

# LIST OF ILLUSTRATIONS

<u>Figure</u>	<u>Title</u>	<u>Page</u>
1	Control volume for the two-dimensional situation . . . . .	6
2	Grid configuration for a one-dimensional situation . . . . .	7
3	Piecewise linear distribution of J . . . . .	9
4	A typical control volume arrangement . . . . .	12
5	Average error for the one-dimensional flow with a source . .	14
6	The solid body rotation problem: the geometry and control volume . . . . .	15
7	Average error for the solid body rotation problem . . . . .	17
8	Recirculating flow with prescribed heat source . . . . .	18
9	Piecewise linear distribution of J . . . . .	21
10	Two adjacent control volumes . . . . .	22
11	Control volume in two dimensions . . . . .	25
12	Definition of a u-control volume . . . . .	28
13	A one-dimensional situation . . . . .	36
14	$\phi$ -profiles at the midsection of the cavity; recirculating flow with a prescribed source . . . . .	41
15	Transport of a step change in $\phi$ in a uniform velocity region . . . . .	42
16	Convective transport of a step change in $\phi$ ; profiles at the vertical midsection of the computational domain . .	43
17	Flow over a backward facing step . . . . .	44
18	Axial velocity profiles for $Re = 100$ . . . . .	46
19	Axial velocity profile for $Re = 715$ . . . . .	48
20	A driven cavity . . . . .	50
21	The u-velocity profile at the vertical midsection of the cavity . . . . .	51
22	The v-velocity profile at the horizontal midsection of the cavity . . . . .	52
23	Temperature profile at the vertical midsection of the cavity . . . . .	53
24	Temperature profile at the horizontal midsection of the cavity . . . . .	54
25	Geometry for turbulent flow over a backward facing step . .	55
26	The u-velocity profiles along the vertical midsection of the cavity . . . . .	56
27	The u-velocity profiles along the vertical midsection of the cavity . . . . .	56
28	Turbulence kinetic energy profiles along the vertical midsection of the cavity . . . . .	57
29	Turbulence viscosity profiles along the vertical midsections . . . . .	57
30	Three-dimensional cubic cavity . . . . .	59
31	The u-velocity profile along the vertical centerline of plane $z = 0.5$ . . . . .	60
32	The v-velocity profile along the horizontal centerline of plane $z = 0.5$ . . . . .	60

# LIST OF ILLUSTRATIONS (CONT)

<u>Figure</u>	<u>Title</u>	<u>Page</u>
33	Shear driven cavity; flow pattern in the y-z plane at x = 0.5 . . . . .	61
34	Geometry for an annular jet-induced flow in a duct . . . . .	62
35	Axial velocity profiles at z = 0 plane, coarse grid . . . . .	63
36	Variation of the centerline axial velocity, coarse grid . . . . .	64
37	Axial velocity profiles at z = 0 plane, fine grid . . . . .	65
38	Variation of centerline axial velocity, fine grid . . . . .	66
39	Flow geometry for "a row of jets in crossflow" . . . . .	67
40	Axial velocity profiles for coarse grid . . . . .	68
41	Axial velocity profiles for fine grid . . . . .	69
42	Predicted velocity vectors in the x-y plane through the jet center line (z = 0) for the coarse grid . . . . .	71
43	Predicted velocity vectors in the x-y plane through the jet center line (z = 0) for the fine grid . . . . .	72
44	Structure of the coefficient matrix . . . . .	74
45	Test cases for 3-D flows . . . . .	79
46	Rate of convergence for 3-D sudden expansion . . . . .	81
47	Rate of convergence for a jet in a rectangular box . . . . .	82

# LIST OF TABLES

<u>Table</u>	<u>Title</u>	<u>Page</u>
I	The function A (P) for various schemes . . . . .	7
II	Turbulent flow over a backward facing step--calculated reattachment lengths [ $x_R/h$ ] . . . . .	52
III	Test cases . . . . .	75
IV	Number of iterations required and execution times . . . . .	75



## SUMMARY

This report describes the details of the work performed under Element A, "Improved Numerical Methods for Turbulent Viscous Recirculating Flows," of NASA sponsored Hot Section Technology (HOST) program. The objective in this study is to develop accurate and efficient numerical schemes for predicting complex flows.

Five discretization schemes were selected for preliminary evaluation based on simple flows. These schemes were evaluated on the basis of accuracy, stability, and ease of extension to multidimensions. This initial evaluation led to the selection of three schemes--linear flux-spline, cubic flux-spline, and controlled numerical diffusion with internal feedback (CONDIF) for further evaluation in two-dimensional flows. The accuracy was assessed by solving a series of test problems that included scalar transport, laminar flows, and turbulent flows. The numerical results were compared with analytical solutions, experimental data, and fine grid numerical solutions. For these test problems, the linear flux-spline scheme was superior to other schemes and was selected for incorporation into a computer program for three-dimensional flows. This scheme was further evaluated by solving three-dimensional flows.

To improve the computational efficiency, a coupled solution approach for the fluid flow equations was adopted. This algorithm was incorporated in conjunction with the linear flux-spline scheme. For two-dimensional flows, this approach led to a factor of 2-3 reduction in execution times compared with the sequential algorithms. To extend the coupled solution approach to three-dimensions, a plane-by-plane solution strategy was followed. For sample flows, such a procedure was robust and fast convergent.



## I. INTRODUCTION

### 1.1 OBJECTIVES

The overall objective of the hot section technology (HOST) aerothermal modeling program--Phase II is to improve the accuracy of the current aerothermal models for gas turbine combustors. Specifically Element A, Improved Numerical Methods for Turbulent Viscous Recirculating Flows, seeks improvements in the accuracy of the differencing schemes and the computational efficiency of the solution algorithms. Improvements in these areas would allow accurate predictions of complex flows in a cost-effective manner without requiring an excessively large number of grid points. Further, the use of improved differencing schemes, which do not suffer significantly from the false diffusion problem, will allow an objective evaluation of various models of gas turbine combustion processes.

### 1.2 APPROACH

The approach followed in this study was to select a number of discretization schemes and solution algorithms and assess them on the basis of accuracy, computational efficiency, stability, and ease of extension to multidimensions. For this preliminary evaluation, test problems with known analytical solutions were selected. Based on the results of these test problems, three discretization schemes were chosen for an in-depth evaluation for two-dimensional flows. In addition, a coupled solution approach for the fluid flow equations was considered.

The selected differencing schemes were incorporated into computer programs for two-dimensional flows. The accuracy characteristics of these schemes were assessed by solving a series of test problems, which included scalar transport, laminar flows, and turbulent flows. The scheme with superior performance was then combined with the coupled solution approach for the fluid flow equations. For some sample flows, this coupled solution approach was compared with an iterative sequential algorithm.

The selected discretization scheme and solution algorithm were then incorporated into a computer program for three-dimensional flows. The improvements in accuracy and computational efficiency were demonstrated by solving some sample three-dimensional test problems.

### 1.3 OUTLINE OF THE REPORT

In Chapter II, an overview of the finite-volume procedure is presented. This is followed by a brief description of the selected differencing schemes and the coupled solution strategy. The results of these schemes for sample test problems are presented. The schemes are evaluated on the basis of various criteria mentioned earlier.

In Chapter III, the three differencing schemes with superior performance are described in detail. In the development, the expressions have been given for one coordinate direction only; expressions in other directions can easily be obtained by simple axis transformation.

In Chapter IV, the results of two- and three-dimensional test cases are presented. For two-dimensional problems, the numerical results have been compared

with available analytical, experimental, and fine-grid numerical solutions. The scheme with superior performance in two-dimensional situations was used to solve three-dimensional problems.

In Chapter V, a coupled solution approach for fluid flow equations is described. For sample flows the performance of such an approach has been compared with that of an iterative procedure.

In Chapter VI, the present work is briefly reviewed and suggestions for further work are given.

## II. DESCRIPTION OF THE SELECTED DISCRETIZATION SCHEMES AND SOLUTION ALGORITHM

### 2.1 FINITE VOLUME METHOD

This section includes preliminary details of the finite- (control-) volume method. The main objective of this discussion is to prepare a common framework within which various schemes, to be discussed later, can be accommodated. For ease of presentation, the development has been restricted to two-dimensional steady flows in Cartesian coordinates.

The conservation equation for a dependent variable  $\phi$  can be expressed in the following general form (Ref 1\*):

$$\frac{\partial J_x}{\partial x} + \frac{\partial J_y}{\partial y} = S \quad (1)$$

where

$$J_x = \rho U \phi - \Gamma \frac{\partial \phi}{\partial x} \quad (2)$$

$$J_y = \rho V \phi - \Gamma \frac{\partial \phi}{\partial y} \quad (3)$$

$\Gamma$  is the "effective" diffusion coefficient and  $S$  is the source of  $\phi$ .

Integrating equation (1) over the control volume around the grid point P (see Figure 1) gives:

$$J_e - J_w + J_n - J_x = (S_c + S_p \phi_p) \Delta x \Delta y \quad (4)$$

where the source term  $S$  has been linearized. The quantities  $J_e$ ,  $J_w$ ,  $J_n$ , and  $J_s$  are integrated fluxes over the control-volume faces. That is,

$$\begin{aligned} J_e &= \int J_x \, dy \text{ over the interface } e \\ &= (\rho U \phi - \Gamma \frac{\partial \phi}{\partial x})_e \Delta y \end{aligned} \quad (5)$$

To estimate the value of the flux at the control-volume faces, approximations for the convected value  $\phi_e$  and the gradient  $(\partial \phi / \partial x)_e$  are needed. These two approximations are the essence of any differencing scheme. A differencing scheme, via a profile assumption for  $\phi$ , leads to an expression for the flux at a control-volume interface that involves the values of  $\phi$  at grid points in the vicinity of the face. When the expressions for fluxes are substituted in equation (4), an algebraic equation involving  $\phi$ 's is obtained. This equation can be expressed in a general form as:

$$a_p \phi_p = \sum a_{nb} \phi_{nb} + b_{f1} + b_s \quad (6)$$

---

\*References are listed at the end of this report.

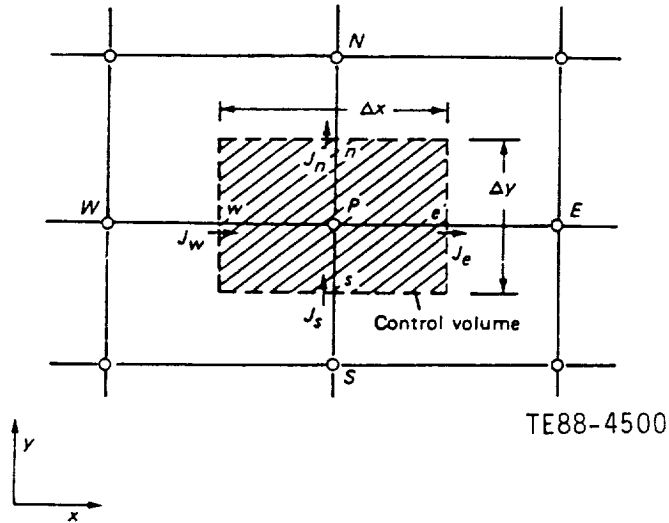


Figure 1. Control volume for the two-dimensional situation.

where nb refers to the neighbors of the grid point P under consideration (nb = E, W, N, S),  $b_s$  includes the physical sources, and  $b_{f1}$  is an apparent source. The expression for  $b_{f1}$  involves either distant neighbors along a coordinate line or adjacent lines or fluxes at control volume interfaces.

## 2.2 DISCRETIZATION SCHEMES

The discussion of the discretization schemes selected in this study is mostly qualitative. The mathematical details have been kept to a minimum. Instead, emphasis has been placed on the features of each scheme that result in better accuracy, the computational molecule involved, and the factors leading to spatial oscillations and the possibility of lack of convergence.

The following five discretization schemes were selected for a preliminary assessment of their accuracy:

1. locally analytic differencing scheme (LOADS)
2. linear flux-spline scheme
3. cubic flux-spline scheme
4. a modified central differencing scheme, CONDIF
5. mass weighted skew upwind differencing scheme (MWSUDS)

The Power-law differencing scheme (PLDS) has been chosen as the representative of all lower-order schemes based on the one-dimensional convection-diffusion equation without a source.

### 2.2.1 Power-Law Differencing Scheme (PLDS)

The Power-law differencing scheme (Ref 1) is based on a curve fit to the exact solution of one-dimensional convection-diffusion equation in the absence of a source. For the situation shown in Figure 2, the final discretization equation may be expressed as:

$$a_P \phi_P = a_E \phi_E + a_W \phi_W + b \quad (7)$$

where

$$a_E = D_e A(|P_e|) + \max[-F_e, 0] \quad (8a)$$

$$a_W = D_w A(|P_w|) + \max[F_w, 0] \quad (8b)$$

$$a_P = a_E + a_W - S_P \Delta x \quad (8c)$$

$$b = S_c \Delta x \quad (8d)$$

$$F = (\rho U) \quad (8e)$$

$$D = \Gamma / \delta x \quad (8f)$$

and

$$P = F/D \quad (8g)$$

The function  $A(P)$  is defined as:

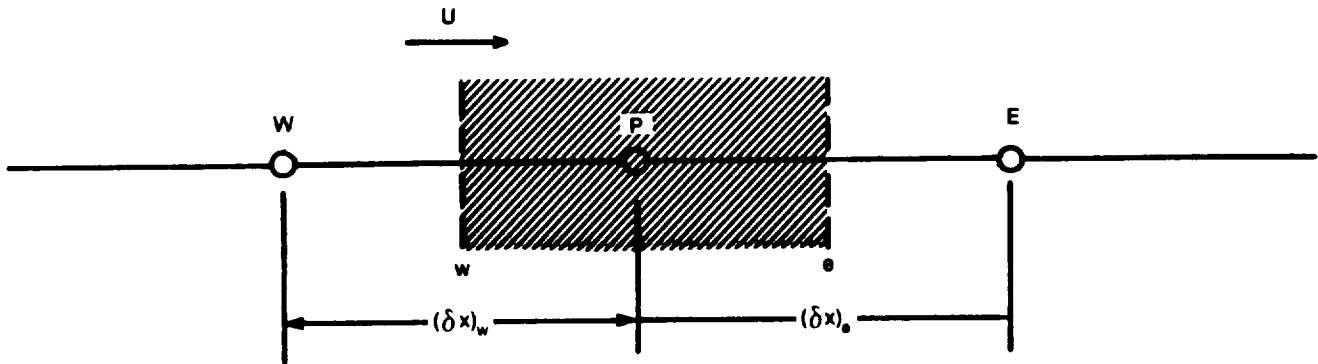
$$A(|P|) = \max[0, (1 - 0.1|P|)^5] \quad (9)$$

where  $\max[ \quad ]$  stands for the largest of the quantities contained within it.

Note that by a proper choice of  $A(|P|)$ , other schemes can also be recovered. For the commonly used schemes, function  $A(|P|)$  is listed in Table I.

Table I.  
The function  $A(P)$  for various schemes.

<u>Scheme</u>	<u><math>A(P)</math></u>
Upwind	1
Hybrid	$\max[0, 1 - 0.5 P ]$
Exponential	$P / [\exp( P ) - 1]$
Power-law	$\max[0, (1 - 0.1 P )^5]$
Central	$1 - 0.5 P $



TE88-4501

Figure 2. Grid configuration for a one-dimensional situation.

Since the Power-law differencing scheme is based on a purely one-dimensional flux balance, it is expected to perform well in the regions in which the flow is aligned along the grid lines and in which convection is balanced primarily by streamwise diffusion rather than cross-stream diffusion or sources. If such idealized conditions are not encountered, the locally one-dimensional assumption gives rise to significant numerical errors (false diffusion). The improved schemes attempt to include the effect of flow-to-grid skewness, lateral transport, and the source in the  $\phi$ -distribution between the grid points.

### 2.2.2 Locally Analytic Differencing Scheme (LOADS)

LOADS (Ref 2) takes into account the influence of the lateral transport processes and source terms in the derivation of the  $\phi$ -distribution between two grid nodes.

The scheme is based on the solution of the equations:

$$\frac{\partial}{\partial x} (\rho U \phi - \Gamma \frac{\partial \phi}{\partial x}) = [S - \frac{\partial}{\partial y} (\rho V \phi - \Gamma \frac{\partial \phi}{\partial y})] = K_x \quad (10)$$

$$\frac{\partial}{\partial y} (\rho V \phi - \Gamma \frac{\partial \phi}{\partial y}) = [S - \frac{\partial}{\partial x} (\rho U \phi - \Gamma \frac{\partial \phi}{\partial x})] = K_y \quad (11)$$

where  $K_x$  and  $K_y$  can be viewed as source terms for flows in  $x$  and  $y$  directions, respectively. They take into account the actual source and the apparent source in a given direction due to the net transport in the other direction. The quantities  $K_x$  and  $K_y$  are evaluated from the numerical solution currently available and are assumed to be constant between two grid points. This leads to a  $\phi$ -distribution along a direction (say  $x$ ) of the form:

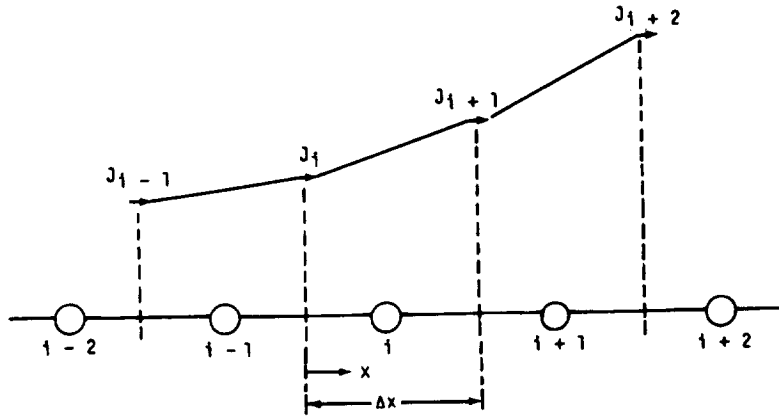
$$\phi = A + B \exp \left( \frac{\rho U}{\Gamma} x \right) + Cx \quad (12)$$

The coefficients in the final discretization equation are identical to those resulting from the exponential scheme except for an additional source that is a function of Peclet numbers in the  $x$  and  $y$  directions.

The computational molecule for LOADS involves 5 points in two dimensions (7 points in 3-D). The influence coefficients are always positive and the algebraic equations are diagonally dominant. The source terms  $K_x$  and  $K_y$ , however, are calculated from nonconverged (incorrect) solutions and are treated explicitly. Such a practice may lead to convergence difficulties, especially if the equations are strongly coupled. The presence of the apparent source may also result in spatial oscillations in the numerical solution.

### 2.2.3 Linear Flux-Spline Scheme

The lower-order schemes, such as hybrid and exponential schemes, represent the solution of the one-dimensional convection diffusion equation with zero source. These schemes, therefore, are based on the assumption of constant total (convection and diffusion) flux within a control volume and do not respond to the presence of sources or sinks and multidimensional effects. The linear flux-spline scheme (Ref 3) removes this shortcoming by assuming a linear variation for the total flux, as shown in Figure 3.



TE84-1679

Figure 3. Piecewise linear distribution of  $J$ .

Thus, the  $\phi$ -profile in the  $x$ -direction for this scheme is the solution of the equation:

$$\rho U \phi - \Gamma \frac{\partial \phi}{\partial x} = J_i + \frac{J_{i+1} - J_i}{\Delta x} \cdot x \quad (13)$$

This can be written as:

$$\phi = A + B \exp\left(\frac{\rho U}{\Gamma} x\right) + Cx \quad (14)$$

where the coefficients  $A$ ,  $B$ , and  $C$  can be expressed in terms of  $\phi_i$ ,  $J_i$ , and  $J_{i+1}$ .

The influence coefficients for the linear flux-spline scheme are identical to those from the exponential scheme except that the linear flux-variation leads to an additional source term. This source term involves the difference of fluxes at the control-volume faces and thus allows the scheme to respond to the presence of sources and multidimensional effects.

The principles underlying the linear flux-spline and LOADS are very similar. They differ only in the manner in which the multidimensional effects are introduced in the  $\phi$ -profile; i.e., the definition of the apparent source. In LOADS the contribution of transport processes in other directions is calculated, within the iterative process, from the nonconverged flow and  $\phi$ -fields. The linear flux-spline scheme seeks a field solution for the fluxes also. So, during the iterative process, the fluxes are related to each other and satisfy the conservation principle; therefore, the linear flux-spline scheme is expected to be superior to LOADS. As with LOADS, the possibility of wiggles due to apparent source also exists in the linear flux-spline scheme. In addition, the details regarding the computational molecule are identical to those for LOADS.

#### 2.2.4 Cubic Flux-Spline Scheme

The cubic flux-spline scheme (Ref 4) is an improved variant of the linear flux-spline scheme. In this scheme, a cubic profile is assumed for the variation of the total flux of  $\phi$  and the mass flux ( $\rho U$ ) within a control volume.

These assumptions lead to a  $\phi$ -profile of the form:

$$\phi = A + B \exp\left(\frac{\rho U}{\Gamma} x\right) + Cx + Dx^2 + Ex^3 \quad (15)$$

As for the linear flux-spline scheme, the cubic flux-spline scheme also involves additional "flux" source terms that allow this scheme to respond to the presence of the source and multidimensional effects.

The rather sophisticated assumptions involved in the cubic flux-spline scheme make it computationally more complex than other schemes considered. The coefficients are no longer simple algebraic function of the Peclet number but involve numerical integration. In addition, field solution is required for the fluxes and their derivatives as well as the derivatives of the mass fluxes. Similar to the linear flux-spline scheme, this scheme also leads to a five-point formulation in two dimensions. The presence of apparent source may lead to wiggles.

Although the cubic flux-spline scheme involves more computational effort than other schemes, this disadvantage may be offset by its higher order of accuracy. Thus for comparable accuracy, the cubic flux-spline scheme would require fewer of grid points.

#### 2.2.5 Controlled Numerical Diffusion with Internal Feedback (CONDIF)

CONDIF (Ref 5) is a modified central differencing scheme (CDS) that retains the second-order accuracy of central differencing scheme but eliminates the overshoots and undershoots that occur if the grid Peclet number exceeds 2. The CONDIF modifies CDS by introducing a controlled amount of numerical diffusion based on local gradients.

CONDIF uses central differencing for points at which the grid Peclet number is less than 2. For points where the Peclet number exceeds 2 and the dependent variable exhibits a monotonic behavior, the central differencing scheme is modified as follows (for 1-D flows):

$$a_P \phi_P = a'_E \phi_E + a'_W \phi_W + b \quad (16)$$

where

$$a'_E = a_{E, \text{CDS}} + \frac{[|(\rho U)_e| + (\rho U)_e]}{4} + A_w/R \quad (17a)$$

$$a'_W = a_{W, \text{CDS}} + \frac{[|(\rho U)_w| - (\rho U)_w]}{4} + A_e R \quad (17b)$$

$$A_e = [|(\rho U)_e| + (\rho U)_e] / 4 \quad (17c)$$

$$A_w = [ |(\rho U)_w| - (\rho U)_w ] / 4 \quad (17d)$$

$$R = (\partial\phi/\partial x)_e / (\partial\phi/\partial x)_w \quad (17e)$$

In these expressions,  $a_E$ , CDS and  $a_w$ , CDS are the coefficients resulting from the central differencing scheme. At the nodes where the Peclet number exceeds 2 and the  $\phi$ -profile is nonmonotonic, the upwind scheme is used.

Since in most practical flows the dependent variables go through an extremum only at relatively few points, CONDIF uses the central differencing scheme in its original or modified form over most of the grid points. By using the CDS, the numerical diffusion is reduced.

The computational molecule for CONDIF involves only 5 points in two dimensions. The coefficients in the modified CDS become nonlinear since they involve the gradients of the dependent variable. As a result, the coefficients for a linear problem need to be recomputed within the iterative process. However, the possibility of wiggles has been eliminated by adding controlled amount of numerical diffusion in the regions of steep gradient. Unlike the previous schemes, CONDIF does not involve any apparent source in the discretization equation.

#### 2.2.6 Mass-Weighted Skew Upwind Differencing Scheme (MWSUDS)

This scheme (Ref 6) seeks to improve the original skew upwind differencing scheme (SUDS) (Ref 7), by ensuring the positivity of the coefficients and thus eliminating the spatial oscillations.

Before presenting the details of MWSUDS, the cause of negative coefficients in the skew upwind differencing scheme is analyzed. A typical control volume is shown in Figure 4. For illustration purposes, the variation of the south coefficient with the flow angle is examined. The value of  $\phi_s$  will appear in the convective fluxes through the east and south faces. The convective flux through the east face is given by:

$$m_e \phi_e = m_e [F_{xe} \phi_s + (1. - F_{xe}) \phi_p] \quad (18)$$

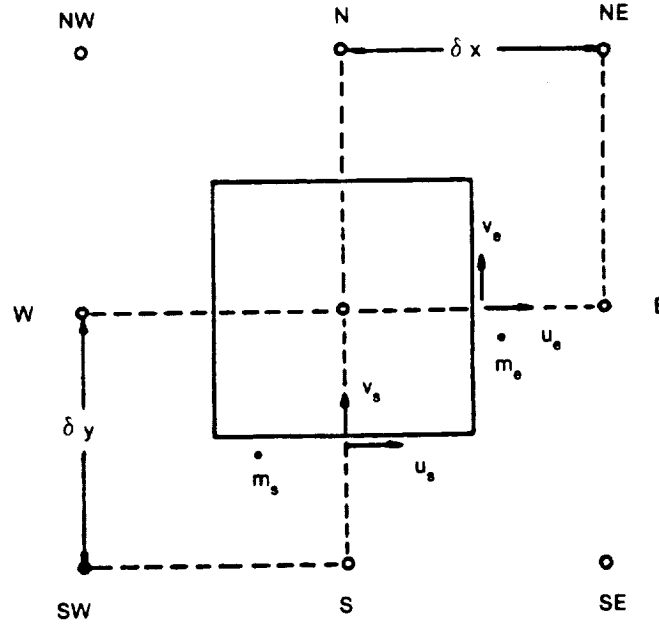
Similarly, the convective flux through the south face is:

$$m_s \phi_s = m_s [F_{ys} \phi_{sw} + (1. - F_{ys}) \phi_s] \quad (19)$$

In the above expressions,  $m_e$  and  $m_s$  are the mass flow rates through the east and south faces, respectively.  $F_{xe}$  and  $F_{ys}$  are weighting factors defined as:

$$F_{xe} = \frac{V_e}{U_e} \frac{\delta x/2}{\delta y} \quad (20)$$

$$F_{ys} = \frac{U_s}{V_s} \frac{\delta y/2}{\delta x} \quad (21)$$



TE88-4502

Figure 4. A typical control volume arrangement.

From equations (18) and (19), the convective part of the south coefficient  $a_s$  can be obtained as:

$$a_s = -m_e F_{xe} + m_s (1 - F_{ys}) \quad (22)$$

The coefficient becomes negative when

$$m_e F_{xe} > m_s (1 - F_{ys}) \quad (23)$$

This may lead to a lack of boundedness. Note that the presence of negative coefficient does not necessarily lead to wiggles in the numerical solution.

In MWSUDS, the coefficients are forced to remain positive (nonnegative in strict sense) under all possible conditions. This is accomplished as follows:

1. The weighting of  $\phi_s$  from the east face and south faces are linked. This coupling is affected via the choice of velocity component  $V_e$  needed for calculating the skew angle at the east face. In original SUDS,  $V_e$  is taken as the average of  $V$  at four neighboring points. In the modified skew scheme  $V_e$  is approximated as  $V_s$ .
2. The weighting factors are expressed in terms of face-skewed mass flow rate components as:

$$F_{xe} = \frac{|\rho V_s|}{|\rho U_e|} \frac{\delta x/2}{\delta y} \quad (24)$$

To ensure stability, the following condition should be satisfied:

$$m_e F_{xe} \leq m_s (1 - F_{ys}) \quad (25)$$

Combining equations (24) and (25), the following relation can be obtained:

$$\begin{aligned} 0.5 &\leq 1 - F_{ys} \\ \text{or } F_{ys} &\leq 0.5 \end{aligned} \quad (26)$$

Therefore, an upper limit of 0.5 is placed on the skewness factor.

The computational molecule for MWSUDS involves 9 points in two dimensions and 27 points in three dimensions. Because of this, the tridiagonal matrix algorithm (TDMA) may not be a suitable solver for the algebraic equations.

The modified scheme, like its original version, accounts for the flow-to-mesh skewness but not for the effect of sources and cross-stream diffusion. It reduces to the upwind scheme for one-dimensional flows.

### 2.3 PRELIMINARY EVALUATION OF THE SCHEMES

The five selected schemes were used to solve a number of model one- and two-dimensional problems. In this section, the relative performance of these schemes is evaluated. The test problems considered are the following:

1. uniform flow in a pipe with a heat source
2. solid body rotation with logarithmic temperature distribution
3. recirculating flow with a prescribed heat source

In addition to the results from the selected schemes, results from two other popular schemes, QUICK (Ref 8) and SUDS (Ref 7) have also been presented for a relative assessment. These results have been taken from Reference 4.

#### 2.3.1 Uniform Flow in a Pipe with a Heat Source

This problem consists of a uniform velocity flow in a pipe. A heat source

$$S = 1 + 2x + \pi \cos(\pi x) + [\pi^2 \sin(\pi x) - 2]/P \quad (27)$$

is prescribed such that the temperature distribution given by

$$T_{ex} = 1 + x + x^2 + \exp(-P) \exp(Px) + \sin(\pi x); 0 \leq x \leq 1 \quad (28)$$

represents an exact solution to the governing equation.

$$\frac{\partial T}{\partial x} - \frac{1}{P} \frac{\partial^2 T}{\partial x^2} = S \quad (29)$$

This problem was solved for a range of Peclet numbers (P) using 10 uniformly spaced control volumes in the computational domain. The results are presented in Figure 5 in terms of the percent average error,  $E_{av}$ , defined by

$$E_{av} = \frac{1}{N} \sum |(1 - T_c/T_{ex})| * 100 \quad (30)$$

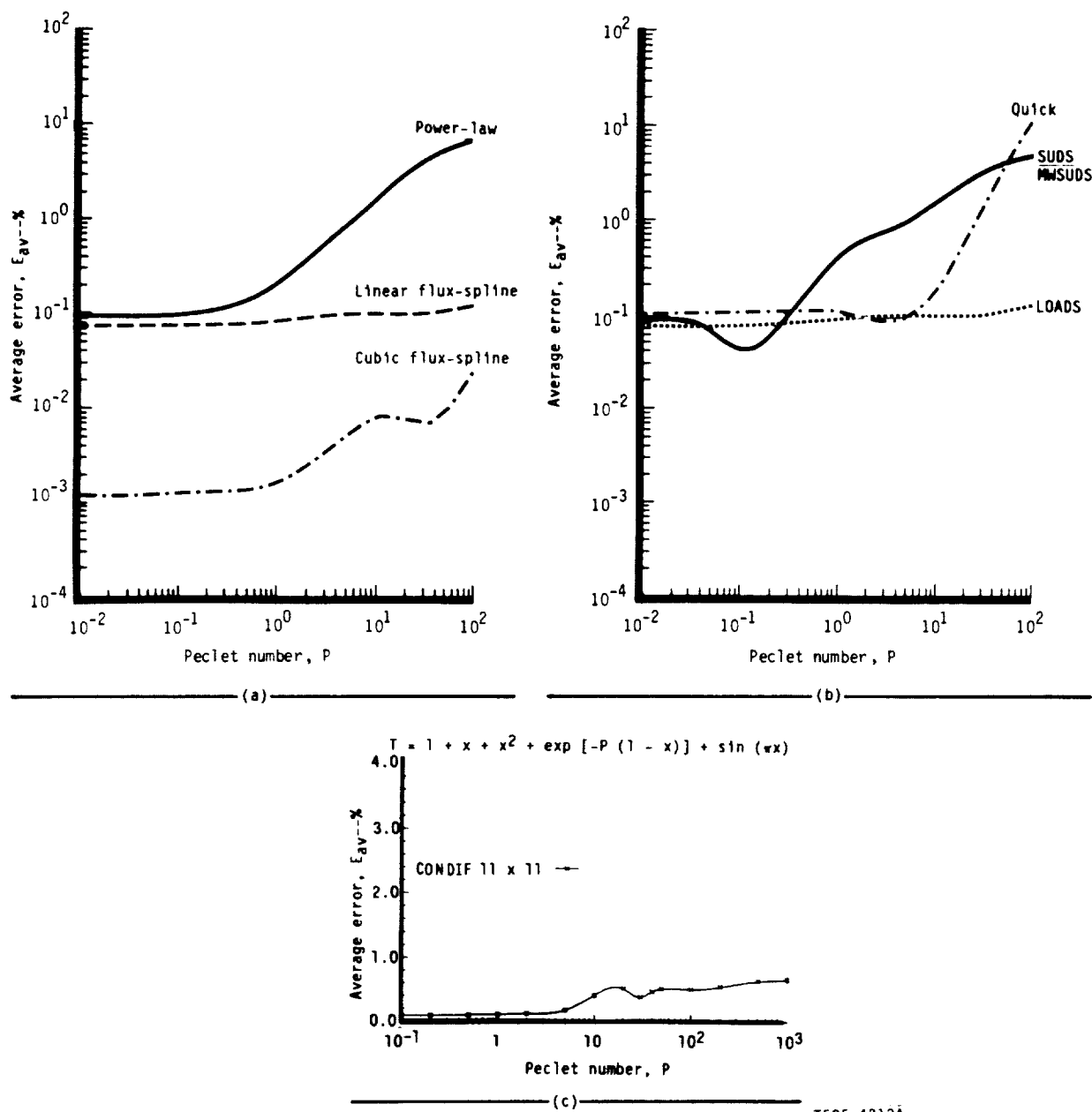


Figure 5. Average error for the one-dimensional flow with a source.

where  $T_c$  is the computed solution and  $N$  is the number of internal nodes.

In the low Peclet number range all schemes result in comparable errors with the exception of the cubic flux-spline scheme, which leads to errors that are about two orders of magnitude smaller. Also, the errors for the linear flux-spline scheme, LOADS, and CONDIF are almost constant over the Peclet number range considered. Other schemes, however, show an increase in the error as the Peclet number exceeds 2.

### 2.3.2 Solid Body Rotation with Logarithmic Temperature Distribution

This test problem, proposed by Runchal (Ref 9), involves heat conduction in a fluid in solid body rotation. The geometry flow field for the problem is shown in Figure 6. This flow situation is one-dimensional in cylindrical coordinates. However, when solved in Cartesian coordinates, the problem becomes fully two-dimensional with finite convective and diffusive contributions.

The governing transport equation for this problem is

$$\frac{\partial}{\partial x} (\rho U T - \Gamma \frac{\partial T}{\partial x}) + \frac{\partial}{\partial y} (\rho v T - \Gamma \frac{\partial T}{\partial y}) = 0 \quad (31)$$

where  $U$  and  $V$  are the velocity components in the  $x$  and  $y$  directions, respectively. For a solid body rotation, these are given by

$$U = 2y, \quad V = -2x \quad (32)$$

For a uniform diffusivity,  $\Gamma$ , given by

$$\Gamma = 1/P, \quad (33)$$

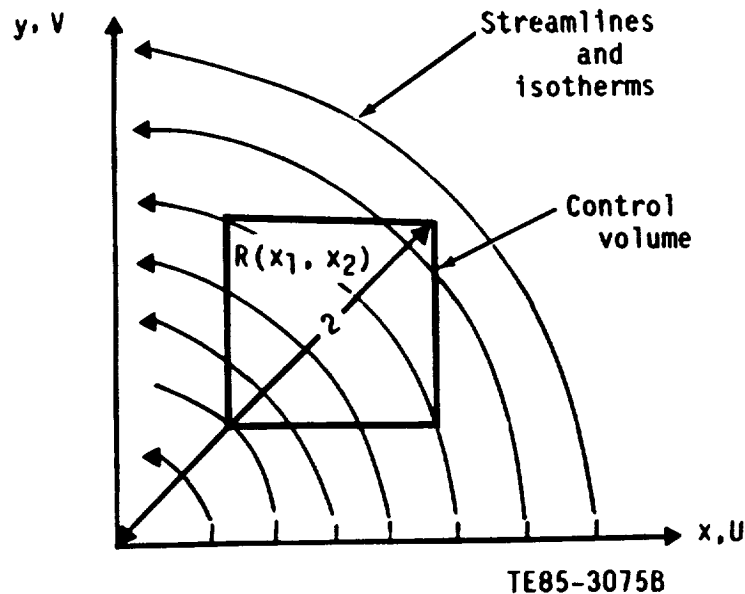


Figure 6. The solid body rotation problem: the geometry and control volume.

the exact solution to the governing equations is obtained as:

$$T_{ex} = 1 - \frac{\ln(x^2 + y^2)}{2 \ln 3} \quad (34)$$

This problem was solved using 10 x 10 uniformly spaced control volumes. The average error,  $E_{av}$ , in the numerical solution for the various schemes considered is shown in Figure 7.

All improved schemes, with the exception of MWSDS, perform considerably better than the lower-order power law differencing scheme at high Peclet numbers. The cubic flux-spline scheme performs exceptionally well, the error being almost two orders of magnitude smaller than that from other schemes. The performances of linear flux-spline, LOADS, CONDIF, and QUICK schemes are comparable over the Peclet number range considered. The use of MWSDS leads to results that are inferior to those from the Power-law scheme because of the inconsistency in the flux expressions at the control-volume faces. That is, the flux expression obtained for the east side of a control volume is not the same as the flux expression for the west side of the next control volume. The validity of the upwind mass flow approximation is also questionable for an arbitrary flow field.

### 2.3.3 Recirculating Flow with a Prescribed Heat Source

In this test problem, transport of a scalar in a prescribed flow field is considered. The velocity field represents a recirculating flow and is given by

$$U = -\bar{U}y (1 - y^2) (1 - x^2)^2 \quad (35)$$

$$V = +\bar{U}x (1 - x^2) (1 - y^2)^2 \quad (36)$$

A source  $S$ , defined as

$$S = P[4 - 2(x^2 + y^2)] \quad (37)$$

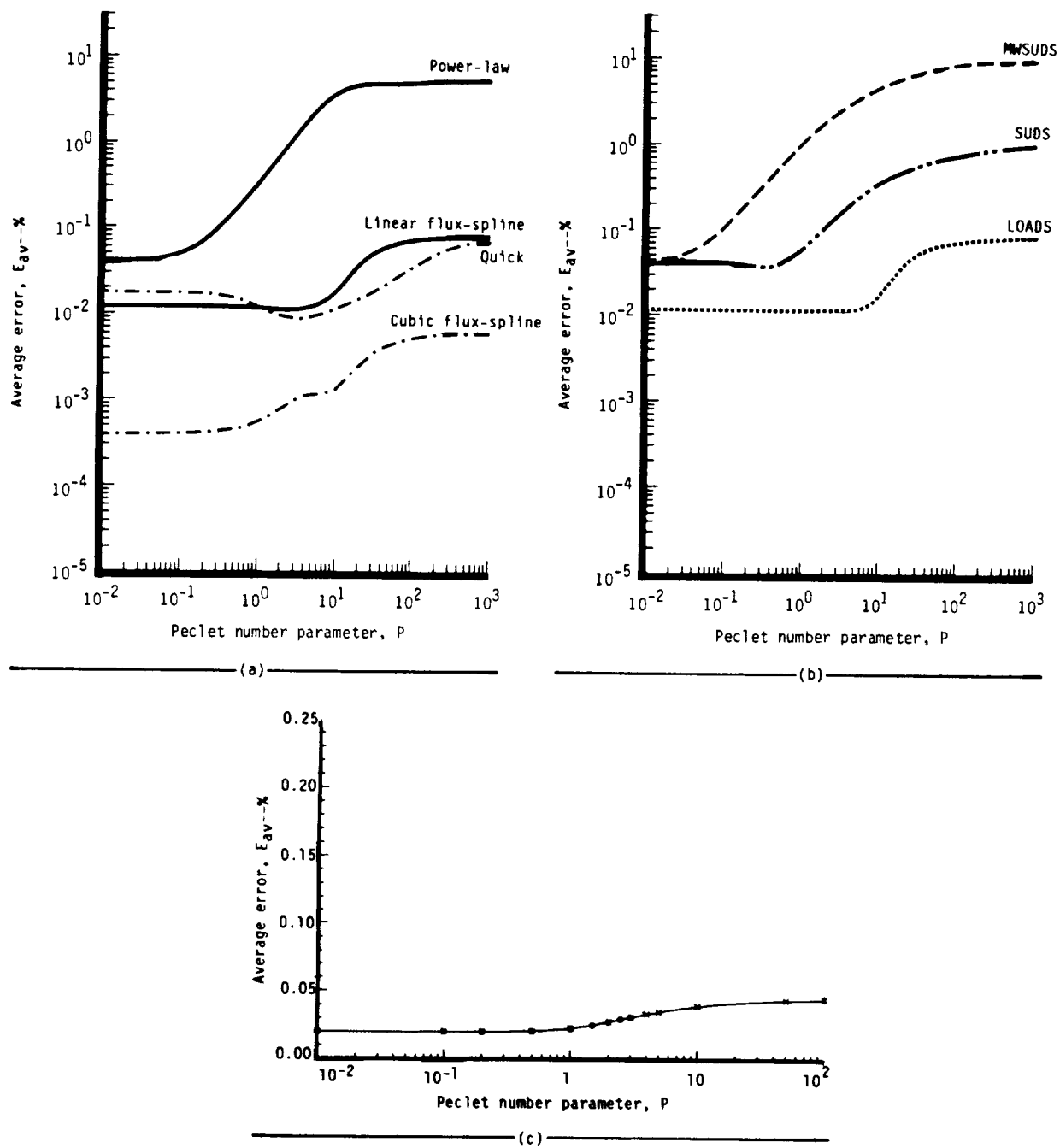
is prescribed such that the exact temperature distribution is given by

$$T_{ex} = (1-x^2) (1-y^2), \quad -1 \leq x, y \leq 1 \quad (38)$$

This problem was solved using a uniform grid with 15 control volumes in each direction.

Figure 8 shows the maximum normalized error in the computed solution from various discretization schemes. For this problem, the flux-spline schemes give results with minimum numerical error. As with the previous problems, the cubic flux-spline is slightly more accurate than the linear flux-spline scheme. The performance of LOADS is not very different from that of the Power-law scheme (PLDS).

Convergence problems were encountered with LOADS for  $P \geq 100$ . This indicates the dominance of the apparent source, which was approximated in a rather simple manner.



TE85-4214A

Figure 7. Average error for the solid body rotation problem.

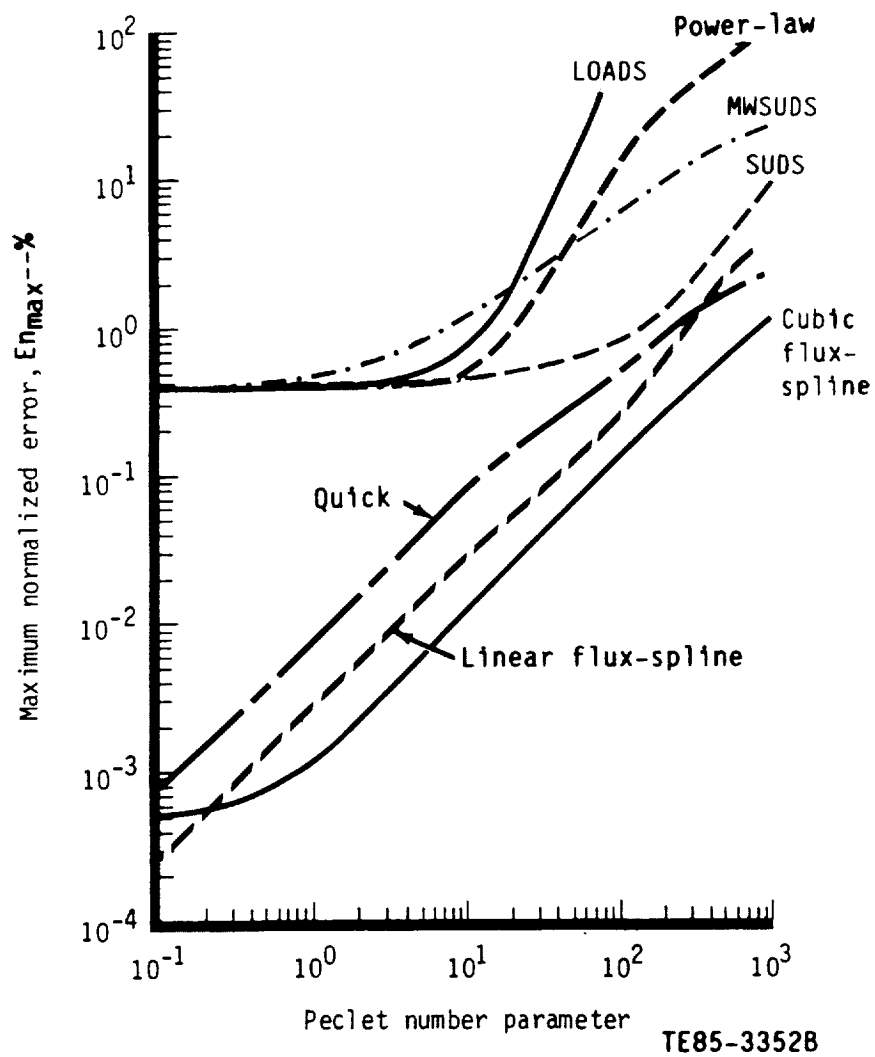


Figure 8. Recirculating flow with prescribed heat source.

The results from CONDIF are not much better than those from the Power-law scheme, especially at high Peclet numbers. The use of MWSUDS results in lower numerical error compared with PLDS for  $P > 10$ .

## 2.4 SUMMARY

The selected convection-diffusion schemes were used to solve three test problems for which analytical solutions are available. Based on the results of these problems, the following general conclusions can be drawn:

1. The improved discretization schemes, with the exception of LOADS and MWSUDS, produce more accurate results compared with the PLDS for all problems considered.
2. The simple treatment of the flux-terms in LOADS may result in lack of convergence, especially at higher Peclet numbers. The convergence behavior is expected to deteriorate as the coupling between various equations becomes stronger.
3. For the test problems considered in this study, the performance of MWSUDS was not significantly superior to that of PLDS. As stated earlier, this behavior may be a consequence of the inconsistency in the discretized flux expressions at the control-volume faces.
4. The performances of LOADS and MWSUDS appear to be problem dependent.
5. Due to mild  $\phi$ -distributions in the selected problems, none of the schemes produced spatial oscillations.

On the basis of these findings and other studies, e.g., Ref 3, 4, 5, the following three schemes were selected for an in-depth evaluation in two-dimensional flows:

1. linear flux-spline scheme
2. cubic flux-spline scheme
3. CONDIF

## 2.5 SOLUTION OF THE FLUID FLOW EQUATIONS

The solution of the fluid flow equations in the primitive variable formulation requires special consideration due to the special role of pressure. The pressure appears in the momentum equations, but there is no pressure term in the continuity equation. Thus there is no equation for an explicit evaluation of the pressure field. The commonly used iterative methods based on SIMPLE (Ref 1) or its variants rewrite the continuity equation as an equation for pressure or pressure correction and the equations are solved sequentially in a decoupled manner. The performance of such an approach depends on a proper choice of the underrelaxation factors and deteriorates as the number of grid points is increased.

An alternative to the sequential SIMPLE-based approach is to obtain a direct solution to the whole set of continuity and momentum equation using a sparse matrix variant of Gaussian elimination. Such a method implicitly retains the coupling between various equations and eliminates the need for an equation for pressure (correction). This coupled approach has been used by Vanka and co-workers (Ref 10, 11) and Braaten (Ref 12) for solving various sample flows in

conjunction with a lower-order discretization scheme (hybrid and Power-law). In all these studies the Yale sparse matrix package (YSMP) (Ref 13) was used for the LU decomposition. The use of the direct solution strategy reduced the computational times by factors of 5-10 compared with the SIMPLE algorithm. In view of its impressive performance, the YSMP-based direct solution approach was selected for improving the computational efficiency of the overall solution algorithm.

### III. DESCRIPTION OF SELECTED DISCRETIZATION SCHEMES

In this section, the three selected convection-diffusion schemes are described in detail. Since the schemes are based on the solution of one-dimensional convection-diffusion equation, most details have been restricted to a single dimension. The expressions for other directions can be obtained by an axis transformation. The derivations have been presented for a general nonuniform grid. By a proper specification of various geometrical parameters, the expressions are valid for a scalar as well as the velocity components. For fluid flow calculations, a staggered grid arrangement is used.

#### 3.1 LINEAR FLUX-SPLINE SCHEME

##### 3.1.1 One-Dimensional Convection-Diffusion

The steady-state form of the one-dimensional convection-diffusion equation is

$$\frac{dJ}{dx} = S \quad (39)$$

where  $J$  is the total flux (convection and diffusion) of the dependent variable  $\phi$ , and  $S$  is the source or sink of  $\phi$ . The total flux is given by

$$J = \rho U \phi - \Gamma \frac{d\phi}{dx} \quad (40)$$

To obtain the variation of  $\phi$  within a control volume, a profile assumption for  $J$  is required. The lower-order methods, such as the exponential scheme, assume that the total flux is uniform within a control volume. Such an assumption leads to a linear profile for  $\phi$  in the conduction-like problems and an exponential profile in convection-diffusion problems. Due to this assumption, the resulting schemes do not respond to the multidimensional effects and the presence of sources. The linear flux-spline scheme is based on the assumption that the total flux varies in a piecewise linear manner as shown in Figure 9. Thus for a control volume around the grid point  $i$ , the total flux is given by

$$J = J_i + (J_{i+1} - J_i) (x/\Delta x_i) \quad (41)$$

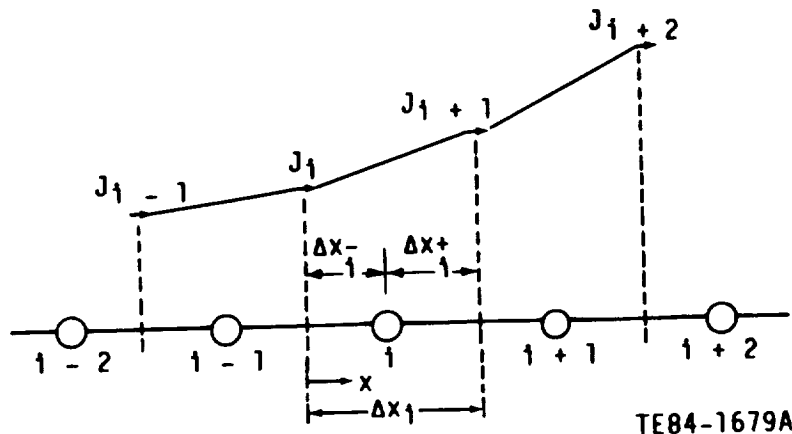


Figure 9. Piecewise linear distribution of  $J$ .

If the expression for  $J$  is substituted in equation (41), a differential equation governing the variation of  $\phi$  is obtained. The solution of the resulting equation requires the variation of the diffusivity  $\Gamma$  and the mass flux  $(\rho U)$ . These quantities are assumed to be uniform over a control volume. With this assumption, the following expression for  $\phi$  results:

$$\phi_i = A + Bx + C \exp (\rho U x / \Gamma) \quad (42)$$

where

$$A = \frac{J_i}{(\rho U)_i} + \left( \frac{J_{i+1} - J_i}{(\rho U)_i \Delta x_i} \right) \frac{\Gamma_i}{(\rho U)_i} \quad (43a)$$

$$B = \frac{J_{i+1} - J_i}{(\rho U)_i \Delta x_i} \quad (43b)$$

$$C = \left[ \phi_i - \frac{J_i}{(\rho U)_i} - \frac{J_{i+1} - J_i}{(\rho U)_i \Delta x_i} \left( \Delta x_i^- + \frac{\Gamma_i}{(\rho U)_i} \right) \right] \exp (-P_i^-) \quad (43c)$$

$$P_i^- = \frac{(\rho U)_i \Delta x_i^-}{\Gamma_i} \quad (43d)$$

Equation (42) gives the variation of  $\phi$  within a control volume. For two adjacent control volumes, the  $\phi$ -profiles are such that they imply the same total flux at the common interface. In addition, they must also give a unique value of  $\phi$  at the common interface. With reference to Figure 10, this condition is:

$$\phi_{i-1}^+ = \phi_i^- \quad (44)$$

where  $\phi_i^-$  and  $\phi_i^+$  are defined as the values of  $\phi$  at the left and right interfaces, respectively, of the control volume around the grid point  $i$ .

From equations (42) and (43)

$$\phi_i^- = \phi_i e^{-P_i^-} + \frac{1}{A(-P_i^-)} \frac{\Delta x_i^-}{\Gamma_i} J_i - \frac{(\Delta x_i^-)^2}{\Delta x_i} \frac{1}{\Gamma_i} (J_i - J_{i+1}) G(-P_i^-) \quad (45)$$

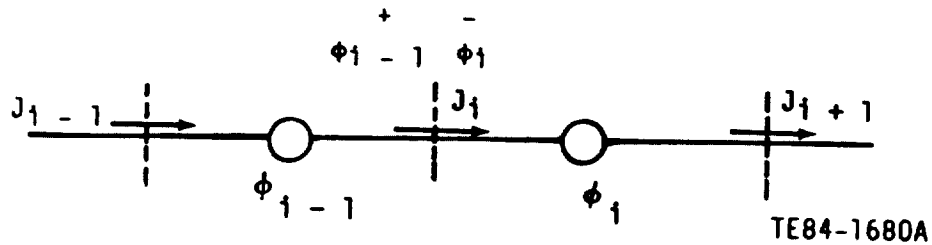


Figure 10. Two adjacent control volumes.

$$\begin{aligned}\phi_{i-1}^+ &= \phi_{i-1} e^{P_{i-1}^+} - \frac{1}{A(-P_{i+1}^+)} \frac{\Delta x_{i-1}^+}{\Gamma_{i-1}} J_i \\ &+ \frac{(\Delta x_{i-1}^+)^2}{\Delta x_{i-1}} \frac{1}{\Gamma_{i-1}} (J_i - J_{i-1}) G(P_{i-1}^+)\end{aligned}\quad (46)$$

where

$$P_{i-1}^+ = \frac{(\rho U)_{i-1} \Delta x_{i-1}^+}{\Gamma_{i-1}} \quad (47)$$

$$A(P) = \frac{P}{e^P - 1} \quad (48)$$

$$G(P) = \frac{e^P (P-1) + 1}{P^2} \quad (49)$$

Combining equations (43) to (49), the expression for flux  $J_i$  can be written as

$$J_i = (D_i \phi_{i-1} - E_i \phi_i) + B_i (J_i - J_{i+1}) + C_i (J_i - J_{i-1}) \quad (50)$$

where

$$D_i = H_i \exp(P_{i-1}^+) \quad (51)$$

$$E_i = H_i \exp(-P_i^-) \quad (52)$$

$$B_i = \frac{(\Delta x_i^-)^2}{\Delta x_i} \frac{1}{\Gamma_i} H_i G(-P_i^-) \quad (53)$$

$$C_i = \frac{(\Delta x_{i-1}^+)^2}{\Delta x_{i-1}} \frac{1}{\Gamma_{i-1}} H_i G(P_{i-1}^+) \quad (54)$$

and

$$H_i = \left( \frac{\Delta x_i^-}{\Gamma_i} \frac{1}{A(-P_i^-)} + \frac{\Delta x_{i-1}^+}{\Gamma_{i-1}} \frac{1}{A(P_{i-1}^+)} \right)^{-1} \quad (55)$$

In equation (50), the expression  $(D_i \phi_{i-1} - E_i \phi_i)$  is identical to that obtained from the lower-order exponential scheme. The terms involving  $B_i$  and  $C_i$

are additional contributions of the flux-spline scheme based on the linear variation of the total flux.

For ease of presentation, let

$$\hat{J}l_i = B_i (J_i - J_{i+1}) + C_i (J_i - J_{i-1}) \quad (56)$$

so that equation (50) may be expressed as:

$$J_i = (D_i \phi_{i-1} - E_i \phi_i) + \hat{J}l_i \quad (57)$$

In this derivation, the mass flux ( $\rho U$ ) was assumed to be uniform within a control volume. To allow for variable mass flux, a correction term is added in the flux expression. The choice of this term is such that the governing equation will be exactly satisfied for a situation in which  $\phi$  is uniform and ( $\rho U$ ) varies linearly. With this additional term, the quantity  $\hat{J}l_i$  in equation (57) is redefined as

$$\begin{aligned} \hat{J}l_i = B_i \left\{ (J_i - J_{i+1}) - [(\rho U)_i - (\rho U)_{i+1}] \phi_i \right\} \\ + C_i \left\{ (J_i - J_{i-1}) - [(\rho U)_i - (\rho U)_{i-1}] \phi_{i-1} \right\} \end{aligned} \quad (58)$$

Note that the spline contribution  $\hat{J}l_i$  to the total flux is based on the differences in the  $J$  values at the adjacent faces of a control volume. Thus, a difference in  $J$  indicates the presence of a source and/or multidimensionality (a change of flux in one direction is felt as a source term in another direction).

### 3.1.2 Discretization Equation for $\phi$

The governing equation (39) can be integrated over the control volume around the point  $i$  to yield

$$J_{i+1} - J_i = S \Delta x_i \quad (59)$$

The fluxes  $J_i$  and  $J_{i+1}$  are replaced by the corresponding expressions from the linear flux-spline scheme, e.g., equation (57). The resulting discretization equation for  $\phi$  is

$$a_p \phi_i = a_E \phi_{i+1} + a_W \phi_{i-1} + S_c \Delta x_i + \hat{S} \quad (60)$$

where

$$a_E = H_{i+1} \exp(-P_{i+1}^-) \quad (61)$$

$$a_W = H_i \exp(P_{i-1}^+) \quad (62)$$

$$a_p = a_E + a_W - S_p \Delta x_i \quad (63)$$

$$\hat{S} = (\hat{J}l_i - \hat{J}l_{i+1}) \quad (64)$$

In this last derivation, a linearized form of the source term  $S$  has been assumed, that is

$$S = S_c + S_p \phi_i \quad (65)$$

with

$$S_p < 0$$

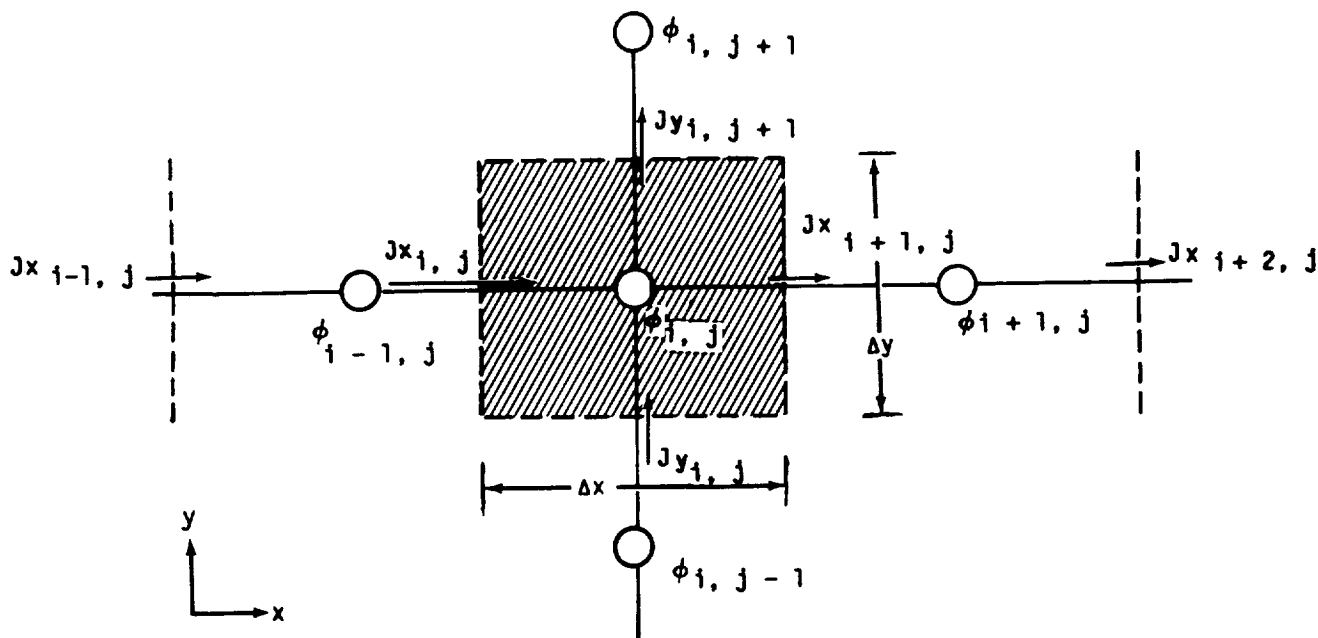
The influence coefficients  $a_E$  and  $a_W$  appearing in the discretization equation resulting from the linear flux-spline formulation are identical to those obtained from the exponential scheme. The contribution of the flux-spline is contained in the term  $\hat{S}$ .

### 3.1.3 Extension to Multi-Dimensional Situations

In this section the extension of the linear flux-spline scheme to multidimensions is presented via the two-dimensional situation. The details for three-dimensional flows are very similar.

For a two-dimensional situation, the conservation equation for the control volume around the point  $(i,j)$  (Figure 11) is:

$$\begin{aligned} & (Jx_{i+1,j} - Jx_{i,j}) \Delta y \\ & + (Jy_{i,j+1} - Jy_{i,j}) \Delta x = S \Delta x \Delta y \end{aligned} \quad (66)$$



TE84-1681A

Figure 11. Control volume in two dimensions.

The fluxes  $J_x$  and  $J_y$  are calculated using the one-dimensional flux-spline formulation in  $x$  and  $y$  direction, respectively. Thus,  $J_x$  and  $J_y$  are given by

$$J_{x_{i,j}} = (Dx_i \phi_{i-1,j} - Ex_i \phi_{i,j}) + \hat{J}_{1x_{i,j}} \quad (67)$$

$$J_{y_{i,j}} = (Dy_j \phi_{i,j-1} - Ey_j \phi_{i,j}) + \hat{J}_{1y_{i,j}} \quad (68)$$

The final expression for  $\phi$  is:

$$\begin{aligned} a_P \phi_{i,j} = & a_E \phi_{i+1,j} + a_W \phi_{i-1,j} + a_N \phi_{i,j+1} + a_S \phi_{i,j-1} \\ & + S_c \Delta x \Delta y + \hat{S} \end{aligned} \quad (69)$$

where

$$a_E = Hx_{i+1} \exp(-Px_{i+1}) \Delta y \quad (69a)$$

$$a_W = Hx_i \exp(Px_i) \Delta y \quad (69b)$$

$$a_N = Hy_{j+1} \exp(-Py_{j+1}) \Delta x \quad (69c)$$

$$a_S = Hy_j \exp(Py_j) \Delta x \quad (69d)$$

$$a_P = a_E + a_W + a_N + a_S - S_p \Delta x \Delta y \quad (69e)$$

$$\begin{aligned} \hat{S} = & (\hat{J}_{1x_i} - \hat{J}_{1x_{i+1}}) \Delta y \\ & + (\hat{J}_{1y_j} - \hat{J}_{1y_{j+1}}) \Delta x \end{aligned} \quad (69f)$$

In equation (69), the descriptors  $x$  and  $y$  have been added to various quantities to denote the appropriate directions. These quantities can easily be obtained by substituting the appropriate directional parameters in the expressions derived earlier for one-dimensional flows.

#### 3.1.4 Solution Procedure

A two-dimensional situation is governed by three field variables,  $\phi$ ,  $J_x$ , and  $J_y$ . These variables are governed by the following three sets of equations:

1. conservation equation for  $\phi$
2. spline continuity condition in the  $x$ -direction
3. spline continuity condition in the  $y$ -direction

Note that the spline-continuity conditions are one-dimensional in nature despite the multidimensional character of the whole problem.

The relationship between the dependent variable  $\phi$  and its fluxes  $J_x$  and  $J_y$  is very similar to that encountered between pressure and velocity components in fluid flow calculations. The spline-continuity conditions give equations for the evaluation of flux fields. These equations involve  $\phi$ . The  $\phi$ -field should be such that the resulting fluxes satisfy the conservation equation for  $\phi$ . Thus, the fluxes are analogous to the velocity components and the role of  $\phi$  is similar to that of pressure. Further, it should be noted that the

derivation of the  $\phi$ -equation from the conservation of  $\phi$  and the flux equations is parallel to that of pressure in SIMPLER algorithm by combining the continuity and momentum equations. Based on these similarities the following procedure can be used for a coupled solution of  $J_x$ ,  $J_y$ , and  $\phi$ .

1. The flux terms  $\hat{J}_{lx}$  and  $\hat{J}_{ly}$  are set equal to zero and the  $\phi$ -equation is solved. This solution will be identical to that from the (lower-order) exponential scheme.
2. The computed  $\phi$ -field is used to obtain the fluxes  $J_x$  and  $J_y$ .
3. These flux fields are used to compute  $\hat{J}_{lx}$  and  $\hat{J}_{ly}$ .
4. The  $\phi$ -equation is solved with the spline contribution to the source term.
5. New  $J_x$  and  $J_y$  fields are obtained from the new  $\phi$ -field and the currently available values of  $\hat{J}_{lx}$  and  $\hat{J}_{ly}$  using equations such as (57).
6. Steps 3 through 5 are repeated until convergence is achieved.

Note that a field solution for the fluxes is not performed. Instead, the fluxes are updated in an iterative manner (Jacobi update).

### 3.1.5 Fluid Flow Calculations

The derivation previously presented is valid for the momentum equations also. Apart from the appearance of an additional source term due to the linear flux assumption, the discretization equation is similar to that from a lower-order formulation.

The solution of the fluid flow equations involves a means of coupling the continuity and momentum equations. These steps are identical to those used for a lower-order formulation and hence are not presented here.

### 3.1.6 Notes on Computer Implementation

1. The expressions for coefficients in the linear flux spline formulation involve the following two functions of the Peclet number:

$$A(P) = \frac{P}{e^P - 1}$$

$$G(P) = \frac{e^P(P-1) + 1}{P^2}$$

If these expressions are used as such, the influence coefficients for linear flux-spline scheme are identical to those from the exponential scheme. To avoid the evaluation of computationally expensive exponentials, these expressions have been approximated by the following algebraic relations:

$$A(P) = \max [0, (1 - 0.1 |P|)^5] + \max [-P, 0] \quad (70)$$

$$G(P) = Q(P)/A(P) \quad (71)$$

where

$$Q(P) = 0.5 [1 + \text{SGN}(P)] - \text{SGN}(P) Q(-P) \quad (72)$$

and

$$Q(-P) = \frac{0.5 - (0.11 P)^2 - (0.25454 P)^6}{1 + P/6 + (0.25454 P)^6 P} \quad (73)$$

With these new relations, the flux-spline scheme reduces to the Power-law differencing scheme under the assumption of constant flux within a control volume.

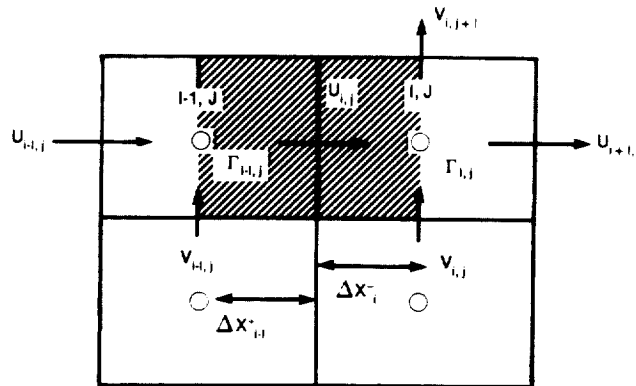
2. The derivation of the flux-spline scheme is based on the assumption of a uniform diffusion coefficient within a control volume. The diffusion coefficients are stored at the main grid points (scalar locations) and are assumed to be constant over the control-volume around the grid point. Due to the staggered location of the velocity components, an estimate of the diffusivity over a velocity control volume is required. In addition, an interpolation is needed to evaluate the mass fluxes at the faces of the velocity control volumes. The practices used in the present implementation are as follows. Consider the U-control volume shown in Figure 12.

The diffusion coefficient for  $U_{i,j}$  is taken to be:

$$\Gamma_{i,j}^U = \frac{\Delta x_i^- \Gamma_{i,j} + \Delta x_{i-1}^+ \Gamma_{i-1,j}}{\Delta x_i^- + \Delta x_{i-1}^+} \quad (74)$$

The mass flux at the west face is

$$(\rho U)_w = [(\rho U)_{i,j} + (\rho U)_{i-1,j}]/2 \quad (75)$$



TE88-4503

Figure 12. Definition of a u-control volume.

and the mass flux at the south face is

$$(\rho V)_s = \frac{(\rho V)_{i-1,j} \Delta x_{i-1}^+ + (\rho V)_{i,j} \Delta x_i^-}{\Delta x_{i-1}^+ + \Delta x_i^-} \quad (76)$$

### 3.2 CUBIC FLUX-SPLINE SCHEME

The cubic flux-spline scheme is an improvement over the linear flux-spline scheme presented in Section 3.1. Similar to the linear flux-spline scheme, the details of the cubic flux-spline scheme are first presented for one-dimensional convection-diffusion situation. This is followed by the details related to its extension to multidimensions.

#### 3.2.1 One Dimensional Convection Diffusion

In cubic flux-spline scheme, the total (convection + diffusion) flux (J) and mass flux ( $\rho U$ ) are assumed to vary according to a cubic profile within a control volume. For the control volume around point i, these are given by:

$$J = J_i + \frac{J_{i+1} - J_i}{\Delta x_i} x + [J_i \Delta x_i - (J_{i+1} - J_i)] \left[ \frac{x}{\Delta x_i} - \left( \frac{x}{\Delta x_i} \right)^2 \right] + (J'_i + J'_{i+1}) \Delta x_i - 2(J_{i+1} - J_i) \left[ \left( \frac{x}{\Delta x_i} \right)^3 - \left( \frac{x}{\Delta x_i} \right)^2 \right] \quad (77)$$

$$\rho U = (\rho U)_i + (\rho U)'_i x + \left\{ 3[(\rho U)_{i+1} - (\rho U)_i] - [2(\rho U)'_i + (\rho U)'_{i+1}] \Delta x_i \right\} \left( \frac{x}{\Delta x_i} \right)^2 + \left\{ [(\rho U)'_i + (\rho U)'_{i+1}] \Delta x_i - 2[(\rho U)_{i+1} - (\rho U)_i] \right\} \left( \frac{x}{\Delta x_i} \right)^3 \quad (78)$$

where  $J'_i$  and  $(\rho U)'_i$  are the derivatives of J and  $(\rho U)$ , respectively, at the control-volume face. For ease of presentation, these equations are rewritten as:

$$J = p_0 + p_1 x + p_2 x^2 + p_3 x^3 \quad (79)$$

$$(\rho U) = q_0 + q_1 x + q_2 x^2 + q_3 x^3 \quad (80)$$

Substituting equations (79) and (80) in the definition of total flux, J,

$$J = \rho U \phi - \Gamma \frac{d\phi}{dx} \quad (81)$$

and integrating, with uniform diffusivity  $\Gamma$ , the following expression for  $\phi$  results:

$$\phi = A - \exp(\int p(x) dx) \int (C_0 + C_1 x + C_2 x^2 + C_3 x^3) \exp(-\int p(x) dx) dx \quad (82)$$

where

$$p(x) = D_0 + D_1 x + D_2 x^2 + D_3 x^3 \quad (83)$$

$$\left. \begin{aligned} C_1 &= p_1/\Gamma, \\ D_i &= q_i/\Gamma, \quad i = 0, 1, 2, 3 \end{aligned} \right\} \quad (84)$$

The constant  $A$  in equation (82) is evaluated using the condition for  $\phi$  at the main grid point

$$\phi(x = \Delta x_i^-) = \phi_i \quad (85)$$

The expression for total flux  $J$  is obtained by imposing the continuity-of- $\phi$  condition at a control-volume interface

$$\phi_i^- = \phi_{i-1}^+ \quad (86)$$

After considerable algebra, the final expression for  $J$  can be written as (Ref 4):

$$J_i = D_i (\phi_{i-1} g_{i-1} - \phi_i g_i^{-1}) + \hat{J}_1 + \hat{J}_3 \quad (87)$$

where

$$\hat{J}_1 = B_i (J_i - J_{i+1}) + C_i (J_i - J_{i-1}) \quad (88)$$

$$\begin{aligned} \hat{J}_3 &= [B_{2,i} \left( \frac{J_{i+1} - J_i}{\Delta x_i} \right) - J_i'] \Delta x_i^- + C_{2,i} \left[ \left( \frac{J_i - J_{i+1}}{\Delta x_{i-1}} \right) - J_{i-1}' \right] \Delta x_{i-1}^+ \\ &+ B_{3,i} \left[ \frac{2(J_i - J_{i+1})}{\Delta x_i} + (J_i' + J_{i+1}') \right] \Delta x_i^- \\ &+ C_{3,i} \left[ \frac{2(J_i - J_{i-1})}{\Delta x_{i-1}} - (J_i' + J_{i-1}') \right] \Delta x_{i-1}^+ \end{aligned} \quad (89)$$

$$D_i = \left[ \frac{\Delta x_{i-1}^+}{\Gamma_{i-1}} \frac{g_{i-1}}{I_{1,i-1}} - \frac{\Delta x_i^-}{\Gamma_i} \frac{1}{I_{1,i}} \right]^{-1} \quad (90)$$

$$B_i = \frac{(\Delta x_i^-)^2 D_i I_{2,i}}{\Gamma_i \Delta x_i I_{1,i}} \quad (91)$$

$$C_1 = \frac{(\Delta x_{i-1}^+)^2 D_1 I2_{i-1} g_{i-1}}{\Gamma_{i-1} \Delta x_{i-1} I1_{i-1}} \quad (92)$$

$$B2_1 = \frac{\Delta x_1}{\Delta x_1^-} B_1 - EP_1 \quad (93)$$

$$C2_1 = \frac{\Delta x_{i-1}}{\Delta x_{i-1}^+} C_1 - EM_1 \quad (94)$$

$$B3_1 = EP_1 - \frac{(\Delta x_1^-)^3 D_1 I4_1}{(\Delta x_1)^2 \Gamma_1 I1_1} \quad (95)$$

$$C3_1 = 2EM_1 - \frac{(\Delta x_{i-1}^+)^3 D_1 I4_{i-1}}{(\Delta x_{i-1})^2 \Gamma_{i-1} I1_{i-1}} - \left( \frac{\Delta x_{i-1}}{\Delta x_{i-1}^+} \right) C_1 \quad (96)$$

$$EP_1 = \frac{(\Delta x_1^-)^2 D_1 I3_1}{\Gamma_1 \Delta x_1 I1_1} \quad (97)$$

$$EM_1 = \frac{(\Delta x_{i-1}^+)^2 D_1 I3_{i-1} g_{i-1}}{\Gamma_{i-1} \Delta x_{i-1} I1_{i-1}} \quad (98)$$

$$I1^{-1} = \int_0^1 I_0 d\eta \quad (99)$$

$$I2 = I1 \int_0^1 \eta I_0 d\eta \quad (100)$$

$$I3 = I1 \int_0^1 \eta^2 I_0 d\eta \quad (101)$$

$$I4 = I1 \int_0^1 \eta^3 I_0 d\eta \quad (102)$$

$$I_0 = \exp [-(a\eta + b\eta^2 + c\eta^3 + d\eta^4)] \quad (103)$$

$$g = \exp (a+b+c+d) \quad (104)$$

$$a_1 = \frac{(\rho U)_1 \Delta x_1^-}{\Gamma_1} \quad (105)$$

$$b_1 = (\rho U)_1' \frac{\Delta x_1^-}{2} \frac{\Delta x_1^-}{\Gamma_1} \quad (106)$$

$$c_1 = \left\{ 3 \frac{(\rho U)_{i+1} - (\rho U)_1}{\Delta x_1} - 2 [(\rho U)_1' + (\rho U)_{i+1}'] \right\} \frac{(\Delta x_1^-)^2}{3 \Delta x_1} \frac{\Delta x_1^-}{\Gamma_1} \quad (107)$$

$$d_1 = \left\{ [(\rho U)_1' + (\rho U)_{i+1}'] - 2 \left[ \frac{(\rho U)_{i+1} - (\rho U)_1}{\Delta x_1} \right] \right\} \frac{(\Delta x_1^-)^3}{4 (\Delta x_1)^2} \frac{\Delta x_1^-}{\Gamma_1} \quad (108)$$

$$a_{i-1} = (\rho U)_{i-1} \frac{\Delta x_{i-1}^+}{\Gamma_{i-1}} - (2b_{i-1} + 3c_{i-1} + 4d_{i-1}) \quad (109)$$

$$b_{i-1} = \frac{[(\rho U)_1 - (\rho U)]_{i-1}}{\Delta x_{i-1}} \frac{\Delta x_{i-1}^+}{2} \frac{\Delta x_{i-1}^+}{\Gamma_{i-1}} - 1.5 c_{i-1} - 1.5 c_{i-1} (1 - f_{i-1}^+) - 2d_{i-1} \frac{(1+f_{i-1}^+)^3}{(1+f_{i-1}^+)} \quad (110)$$

$$c_{i-1} = [(\rho U)'_1 - (\rho U)'_{i-1}] \frac{\Delta x_{i-1}^+}{6 (1 + f_{i-1}^+)} \frac{\Delta_{i-1}^+}{\Gamma_{i-1}} - 2d_{i-1} (1 - f_{i-1}^+) \quad (111)$$

$$d_{i-1} = \left\{ [(\rho U)'_{i-1} + (\rho U)'_i] - 2 \frac{[(\rho U)_i - (\rho U)_{i-1}]}{\Delta x_{i-1}} \right\} \\ 4 \left( 1 + \frac{\Delta x_{i-1}^+}{f_{i-1}^+} \right)^2 \frac{\Delta x_{i-1}^+}{\Gamma_{i-1}} \quad (112)$$

$$f_{i-1}^+ = \frac{\Delta x_{i-1}}{\Delta x_{i-1}^+} \quad (113)$$

The expressions in other directions can be derived by axis transformation. The integrals in equations (99) to (102) are evaluated numerically. These details can be found in Ref 4.

The expressions presented previously involve the derivatives of the total flux and the mass flux. These derivatives are evaluated by solving the spline relationship between a cubic function and its derivative. The derivative of the total flux is obtained from the equation:

$$\frac{J'_{i-1}}{\Delta x_{i-1}} + 2 \left[ \frac{1}{\Delta x_{i-1}} + \frac{1}{\Delta x_i} \right] J'_i + \frac{J'_{i+1}}{\Delta x_i} \\ = 3 \frac{J_{i+1} - J_i}{\Delta x_i^2} + 3 \frac{J_i - J_{i-1}}{\Delta x_{i-1}^2} \quad (114)$$

The relationship for  $(\rho)'$  is obtained by replacing  $J$  by  $(\rho U)$  in equation (114).

### 3.2.2 Discretization Equation in Two Dimensions

The discretization equation for  $\phi$  is now obtained by substituting the flux expression, equation (87), in the conservation equation for  $\phi$ , equation (66). The general  $\phi$  discretization equation is:

$$a_P \phi_i = a_E \phi_{i+1} + a_W \phi_{i-1} + a_N \phi_{j+1} + a_S \phi_{j-1} + b \quad (115)$$

where

$$a_E = DX_{i+1,j} \ 1/gx_{i+1,j} \ , \ a_W = DX_{i,j} \ gx_{i-1,j} \quad (116)$$

$$a_N = DY_{i,j+1} \ 1/gy_{i,j+1} \ , \ a_S = DY_{i,j} \ gx_{i,j-1} \quad (117)$$

$$a_P = a_E + a_W + a_N + a_S - S_P \Delta x_i \Delta y_j + B \quad (118)$$

$$b = S_C \Delta x_i \Delta y_j + b_{ad} \quad (119)$$

$$B = \max [a_W, 0] + \max [-a_E, 0] + \max [a_S, 0] + \max [-a_N, 0] \quad (120)$$

$$\begin{aligned}
b_{ad} = & JC_{i,j} \Delta x_i \Delta y_j \\
& + [(J1X_{i,j} + J3X_{i,j}) - (J1X_{i+1,j} + J3X_{i+1,j})] \Delta y_j + \\
& + [(J1Y_{i,j} + J3Y_{i,j}) - (J1Y_{i,j+1} + J3Y_{i,j+1})] \Delta x_i \\
& + \{ \max[-a_{1W}, 0] + \max[a_{1E}, 0] + \max[-a_{1S}, 0] + \max[a_{1N}, 0] \} \phi_i \quad (121)
\end{aligned}$$

$$a_{1W} = (\rho U)_{i,j} \Delta y_j - (a_{W,(i,j)} - a_{E,(i-1,j)}) \quad (122)$$

$$a_{1E} = (\rho U)_{i+1,j} \Delta y_j - (a_{W,(i+1,j)} - a_{E,(i,j)}) \quad (123)$$

$$a_{1S} = (\rho V)_{i,j} \Delta x_i - (a_{S,(i,j)} - a_{N,(i,j-1)}) \quad (124)$$

$$a_{1N} = (\rho V)_{i,j+1} \Delta x_i - (a_{S,(i,j+1)} - a_{N,(i,j)}) \quad (125)$$

where all definitions given for the x direction, equations (87) through (114), should be applied for a line of constant j and analogous expressions should be used for the y direction.

In the derivation of the flux balance over a control volume, it is generally assumed that the flux at the midpoint of a control-volume face prevails over the entire face. Further the value of the source at the grid point is assumed to prevail over the entire control volume. These approximations reduce the accuracy of the cubic flux-spline scheme. To compensate for this adverse effect on accuracy, an additional correction term  $JC_{i,j}$  (Ref 4) is added in the final discretization equation. This term is evaluated by ensuring that the conservation equation is exactly satisfied at the main grid point and involves the fluxes and their derivatives.

### 3.2.3 Solution Procedure

The main steps in the solution procedure for the cubic flux spline scheme applied to convection-diffusion problems are as follows:

1. guess a  $\phi$  field
2. set all fluxes and flux derivatives equal to zero
3. set all mass flow rate derivatives in the x and y directions equal to zero
4. solve equation similar to (114) with the TDMA algorithm to obtain the  $\rho U$ ' field
5. solve an equation analogous to (114) with the TDMA algorithm to obtain the  $\rho V$ ' field
6. calculate all flux coefficients, equations (90) through (113) for the x directions and analogous expressions for the y direction
7. form all neighbor coefficients, equations (116) and (117), where all integral functions are numerically evaluated by the use of a six point Gauss Quadrature
8. calculate  $\hat{J}1X$  and  $\hat{J}3X$ , equations (88) and (89), by using the available  $\phi$ ,  $Jx$ , and  $J'x$  fields. Proceed in an analogous way for the y direction. Form the source term b and the ap term for the  $\phi$  equation using equations (118) through (125)
9. solve the  $\phi$  equation (115) by the line-by-line TDMA algorithm

10. calculate new fluxes for the x direction from equation (87), where all neighboring  $J_x$  and  $J'_x$  values are assumed known; proceed in an analogous way for the y direction
11. solve the  $J'_x$  equation (114) by the TDMA algorithm and similarly solve for  $J'_y$
12. check convergence (If convergence has not been attained, one must repeat the process by going back to step 4. If the flow field is given and if the coefficients are constant, repeat the process going back to step 8.

If the coefficients are constant, the process must be repeated from step 8 to avoid recalculating the integral functions.

### 3.3 CONTROLLED NUMERICAL DIFFUSION WITH INTERNAL FEEDBACK (CONDIF)

CONDIF is a modified central differencing scheme (CDS) that eliminates the over- and undershoots associated with CDS but retains its accuracy even at high Peclet numbers. CONDIF modifies the CDS by introducing a controlled amount of numerical diffusion based on the local gradients. For most problems, the numerical diffusion can be adjusted to be negligibly low.

Since the CDS forms the basis of CONDIF, the development begins with a discussion of CDS. This is followed by the essential features of CONDIF. Like the derivation of other schemes, the analysis begins with one-dimensional transport of a scalar.

#### 3.3.1 Central Difference Scheme

The one-dimensional convection-diffusion equation is

$$\frac{dJ}{dx} = S \quad (126)$$

where

$$J = \rho U \phi - \Gamma \frac{d\phi}{dx} \quad (127)$$

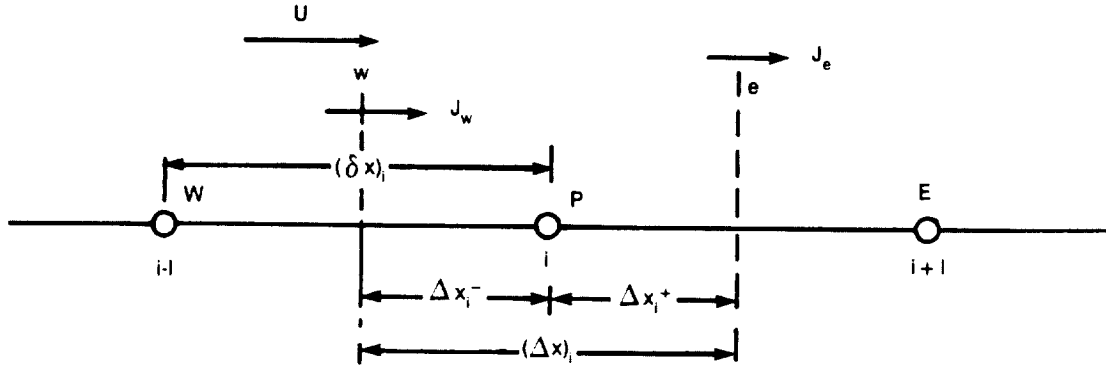
In CDS, the values at a control-volume face are obtained using a piecewise linear profile for  $\phi$ . Thus, the values of  $\phi$  and  $(d\phi/dx)$  at the west face of the control volume around point  $i$  (see Figure 13) are

$$\phi_w = \frac{\Delta x_i^-}{\delta x_i} \phi_{i-1} + \frac{\Delta x_{i-1}^+}{\delta x_i} \phi_i \quad (128)$$

$$\left(\frac{d\phi}{dx}\right)_w = \frac{\phi_i - \phi_{i-1}}{\delta x_i} \quad (129)$$

The discretized conservation equation is given by

$$J_e - J_w = S \Delta x \quad (130)$$



TE88-4504

Figure 13. A one-dimensional situation.

Substituting for the fluxes, the final  $\phi$ -equation can be written as:

$$a_P \phi_i = a_E \phi_{i+1} + a_W \phi_{i-1} + b \quad (131)$$

where

$$a_E = \frac{\Gamma_e}{\delta x_{i+1}} - \frac{\rho U_e}{2} \quad (132a)$$

$$a_W = \frac{\Gamma_w}{\delta x_i} + \frac{\rho U_w}{2} \quad (132b)$$

$$a_P = a_E + a_W \quad (132c)$$

$$b = S \Delta x \quad (132d)$$

For  $P (= \rho u \delta x / \Gamma) > 2$ , the coefficients in CDS become negative resulting in over- and undershoots in the numerical solution. CONDIF is a modified central differencing scheme that retains the essential features of CDS but ensures positivity of the coefficients.

Consider the coefficients  $a_E$  and  $a_W$ ; these may be expressed as

$$a_E = a_E^* - A_e \quad (133)$$

and

$$a_W = a_W^* - A_w \quad (134)$$

where

$$a_E^* = \Gamma_e / (\delta x)_{i+1} + [ |(\rho U)_e| - (\rho U)_e ] / 4 \quad (135)$$

$$a_W^* = \Gamma_w / (\delta x)_i + [ |(\rho U)_w| + (\rho U)_w ] / 4 \quad (136)$$

$$A_e = [ |(\rho U)_e| + (\rho U)_e ] / 4 \quad (137)$$

$$A_w = [ |(\rho U)_w| - (\rho U)_w ] / 4 \quad (138)$$

Note that  $a_E^*$  and  $a_W^*$ ,  $A_e$ , and  $A_w$  are all unconditionally positive.

Equation (131) may now be rearranged as:

$$(a_E^* + a_W^*) \phi_i = a_E^* \phi_{i+1} + a_W^* \phi_{i-1} + A_e (\phi_i - \phi_{i+1}) + A_w (\phi_i - \phi_{i-1}) + b \quad (139)$$

In equation (139), the terms involving  $A_e$  and  $A_w$  need special consideration if these terms are treated implicitly, the original CDS is recovered and oscillations are encountered in the numerical solution. Due to the dominant contribution of these terms at high Peclet number, an explicit treatment (i.e., as a source term) is also not feasible. The CONDIF scheme restructures this equation based on the local gradients of the dependent variable.

### 3.3.2 Alternate Representation of CDS

In equation (139), the term involving  $A_w$  may be expressed as

$$A_e (\phi_i - \phi_{i+1}) = A_e R (\phi_{i-1} - \phi_i); \phi_i \neq \phi_{i-1} \quad (140)$$

where

$$R = (\phi_i - \phi_{i+1}) / (\phi_{i-1} - \phi_i) \quad (141)$$

Similarly, the term involving  $A_w$  may be rearranged as

$$A_w (\phi_i - \phi_{i-1}) = A_w (\phi_{i+1} - \phi_i) / R; \phi_{i+1} \neq \phi_i \quad (142)$$

The special cases when  $\phi_i$  equals  $\phi_{i+1}$  or  $\phi_{i-1}$  are discussed later.

Equation (139) may now be written as:

$$(a'_E + a'_W) \phi_i = a'_E \phi_{i+1} + a'_W \phi_{i-1} \quad (143)$$

with

$$a'_E = a_E^* + A_w / R \quad (144)$$

$$a'_W = a_W^* + A_e R \quad (145)$$

Equation (143), for all practical purposes, is identical to equation (139) and is another representation of CDS. Also all terms in Equations (143), except  $R$ , are unconditionally positive.

### 3.3.3 Derivation of CONDIF Scheme

An examination  $R$  in equation (141) shows that, with reference to Figure 13, it may be written as

$$R \sim (\partial\phi/\partial x)_e / (\partial\phi/\partial x)_w \quad (146)$$

$R$  is proportional to the ratio of the gradient of  $\phi$  at the control-volume faces  $e$  and  $w$ . Finding the conditions under which  $R$  may become negative is now possible. For a monotonically increasing and decreasing function,  $R$  would always be positive. It is only for a function going through an extremum (a maximum or a minimum) within the control-volume around  $P$  that  $R$  becomes negative.

In most fluid dynamic calculations, the dependent variables exhibit a monotonic behavior at most of the grid points; it is comparatively at a few grid points that the variables go through an extremum. With this observation, the CDS is modified as follows.

1. For all the grid points where the grid Peclet number is less than or equal to 2, the CDS is used in the form given by equations (131) and (132).
2. For the case where the grid Peclet number exceeds 2, the CDS is used in the form given by equations (143) to (145); if the  $R$ -parameter is positive, otherwise.
3. The upwind scheme is used.

The suggested modification of CDS ensures the positivity of coefficients and hence eliminates the over- and undershoots. Note that the influence coefficients now become quasi-linear. This is because the  $R$ -parameter represents the ratio of the gradient of the dependent at the control-volume faces.

The parameter,  $R$ , may assume very high values if sharp variations in the gradient of the dependent variable exist. Conversely  $R$  may approach a value of zero if  $\phi$  is locally constant ( $\phi_i = \phi_{i-1}$  or  $\phi_{i+1}$ ). These cases represent either a singularity in the governing equation or a trivial solution ( $\phi = \text{constant}$ ). Therefore, a limit on the  $R$ -parameter is imposed so that

$$\frac{1}{R_{\max}} \leq R \leq R_{\max} \quad (147)$$

where  $R_{\max}$  is an arbitrary number. It determines the amount by which the gradient of the variable may change from one grid point to another. The parameter  $R_{\max}$  plays the role of introducing a controlled amount of numerical diffusion in the numerical diffusion.

The modified scheme previously described is named CONDIF (Controlled Numerical Diffusion with Internal Feedback). The numerical diffusion comes from the limit imposed on the R-parameter; the feedback refers to the self-adjusting feature of the scheme based on the ratio of the gradients at the adjacent control-volume faces.

#### IV. EVALUATION OF SELECTED SCHEMES

The three discretization schemes were used to solve a variety of two-dimensional test problems. The test problems included transport of a scalar, laminar flows and turbulent flows. For each case the numerical results were compared with a reference solution. In the turbulent flow test cases, emphasis was placed on the differences between the various numerical results rather than assessing their accuracy against the experimental data. Such a practice has been followed primarily because the use of a turbulence model introduces additional uncertainty in the numerical results and it is difficult to distinguish between the model-related errors and the numerical errors. Further, the differences between the experimentally and numerically realized boundary conditions make a thorough comparison between the experimental data and calculations more difficult. To circumvent this difficulty, fine-grid numerical solutions have been taken as reference solutions for some test cases.

The test problems used are

##### scalar transport (2-D)

1. recirculating flow with a prescribed heat source
2. transport of a step discontinuity in a uniform flow at an angle

##### laminar flows (2-D)

1. flow over a backward-facing step
2. flow and heat transfer in a shear-driven cavity

##### turbulent flows (2-D)

1. flow over a backward-facing step
2. flow in a shear-driven cavity

##### laminar flows (3-D)

1. flow in a shear-driven cubic cavity

##### turbulent flows (3-D)

1. annular jet-induced flow in a duct
2. row of jets in cross flow

The results for these test cases are presented in the following sections.

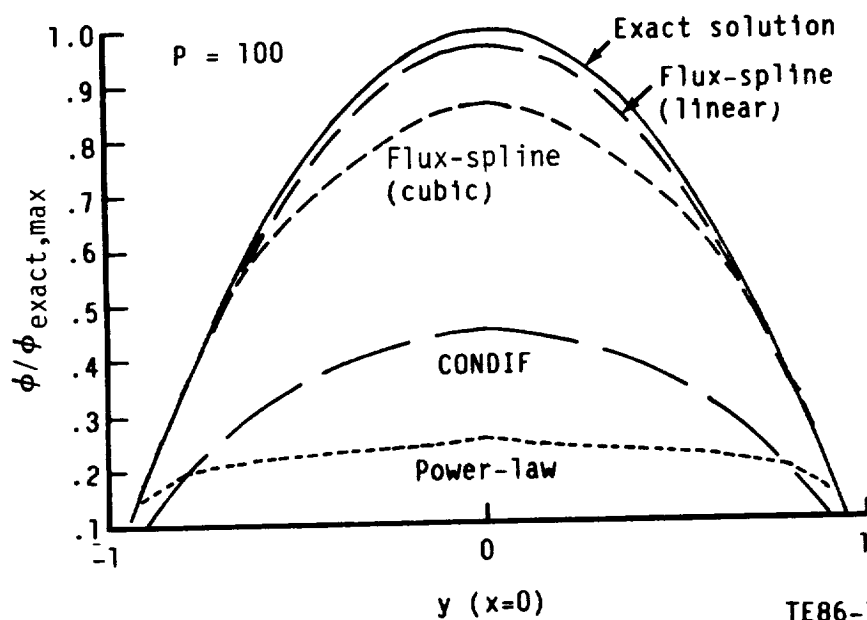
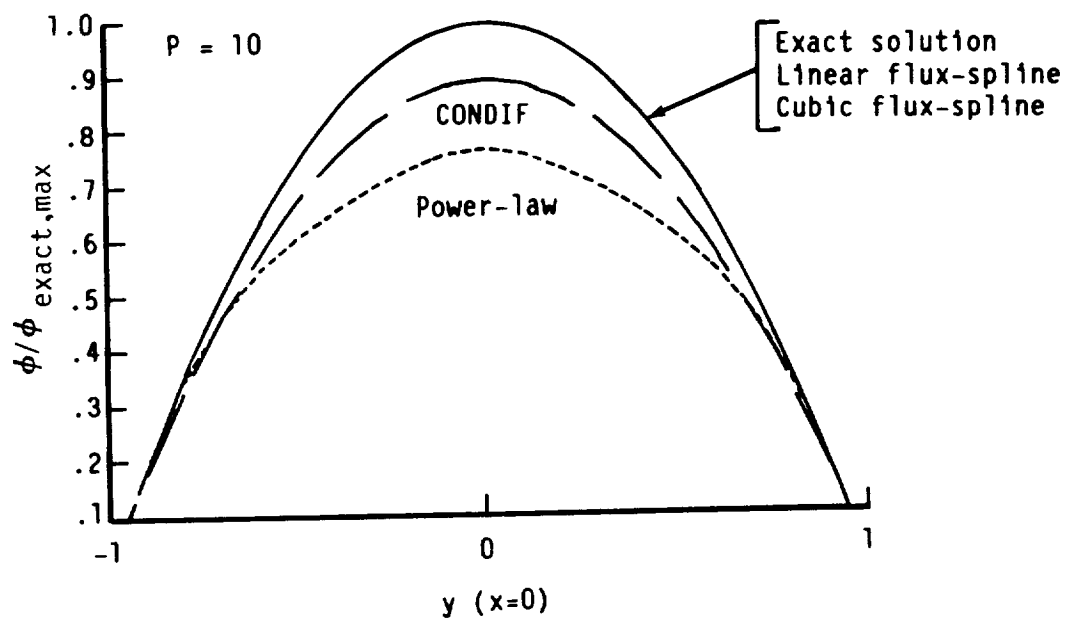
#### 4.1 TWO-DIMENSIONAL TEST CASES

##### 4.1.1 Scalar Transport

##### 4.1.1.1 Recirculating Flow with a Prescribed Heat Source (Revisited)

This test case was described in subsection 2.3.3, where the performance of various schemes was presented in terms of an error parameter. The results for this problem are now analyzed in greater detail to assess the accuracy of the selected improved discretization schemes. Specifically, these results reveal the response of the discretization schemes to a variable source.

The  $\phi$ -distributions at the vertical midsection ( $x = 0$ ) of the square domain, obtained using a uniform  $22 \times 22$  grid, are compared with the exact solution in Figure 14. At  $P = 10$ , both flux-spline schemes almost reproduce the exact



TE86-1291B

Figure 14.  $\phi$ -profiles at the midsection of the cavity; recirculating flow with a prescribed source.

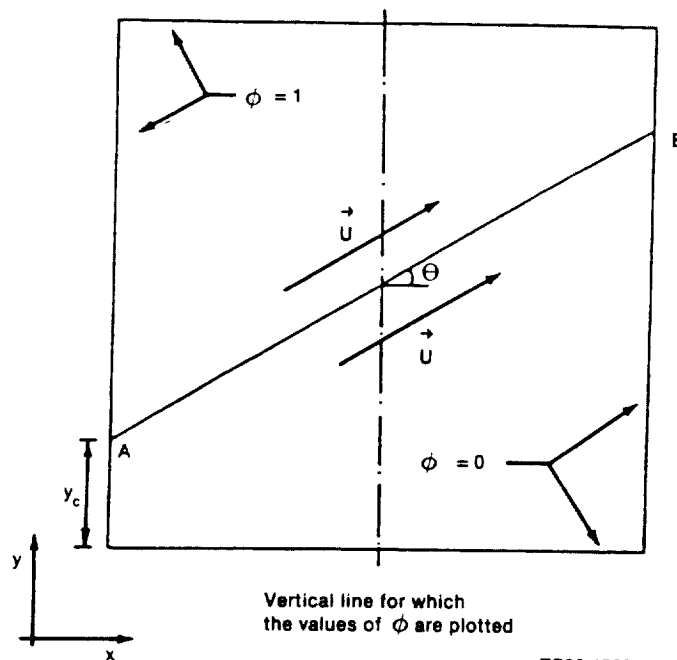
solution. CONDIF results are significantly more accurate than those from the Power-law scheme, which produces a diffused profile, indicating the presence of false diffusion.

The effect of false diffusion in the Power-law solution is much more evident at  $P = 100$ . The flux-spline schemes still give very accurate solution. CONDIF results, even though superior to those from the Power-law scheme, exhibit substantial smearing, indicating the need of excessive numerical diffusion to stabilize the central-difference scheme at this high Peclet number and in the presence of a variable source.

#### 4.1.1.2 Step Discontinuity in a Uniform Flow at an Angle

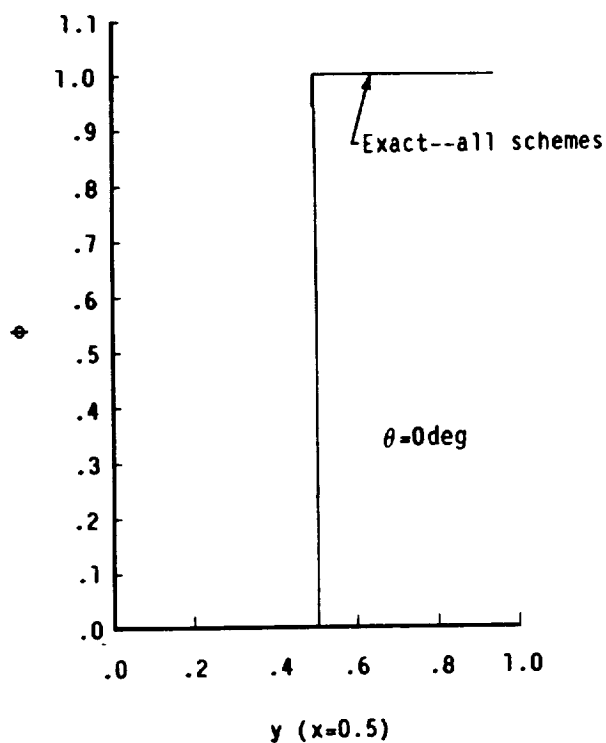
This problem is concerned with the transport of a step change in  $\phi$  in a uniform velocity field directed at angle to the x-axis as shown in Figure 15. With the diffusion coefficient  $\Gamma \rightarrow 0$ ,  $\phi$  is transported purely by convection; consequently, the step change in  $\phi$  at the upstream boundary is simply convected in the flow direction without any smearing. Even though there is no source present, this seemingly simple problem is a severe test for a convection-diffusion scheme. The flow is directed at an angle to the grid lines, and the gradient in the cross-stream direction is infinite across the line AB in Figure 15. Further, there is no physical diffusion in this problem, and any smearing of the sharp profile would be a direct consequence of the false diffusion.

For the given boundary conditions, the problem was solved using a uniform  $11 \times 11$  grid. Solutions were obtained at various flow angles,  $\theta = 0, 15, 30$ , and  $45$  deg. The calculated profiles along the vertical centerline of the domain are presented in Figure 16. These results show that the profiles from the

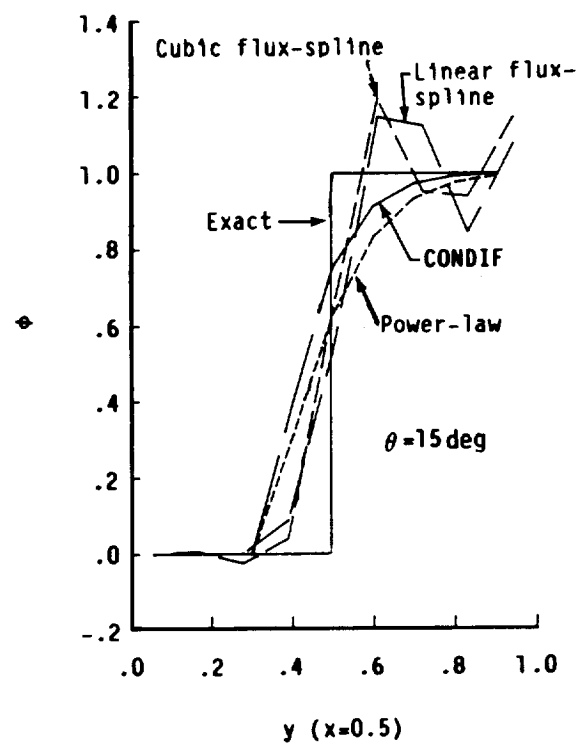


TE88-4505

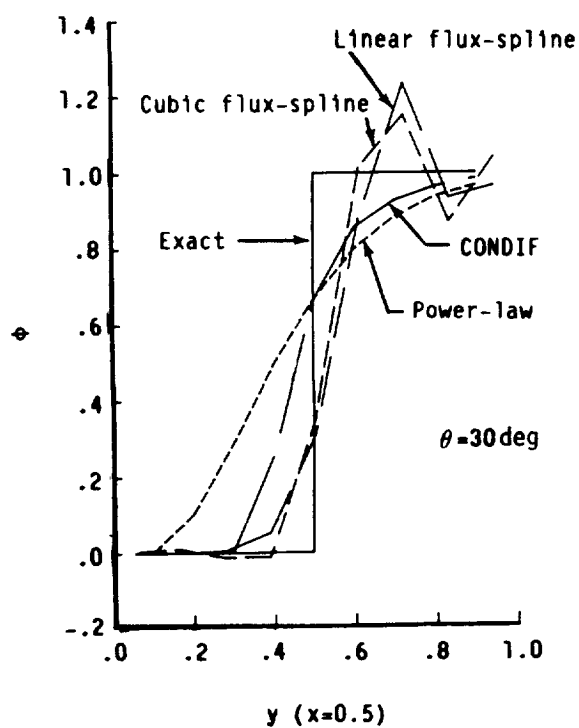
Figure 15. Transport of a step change in  $\phi$  in a uniform velocity region.



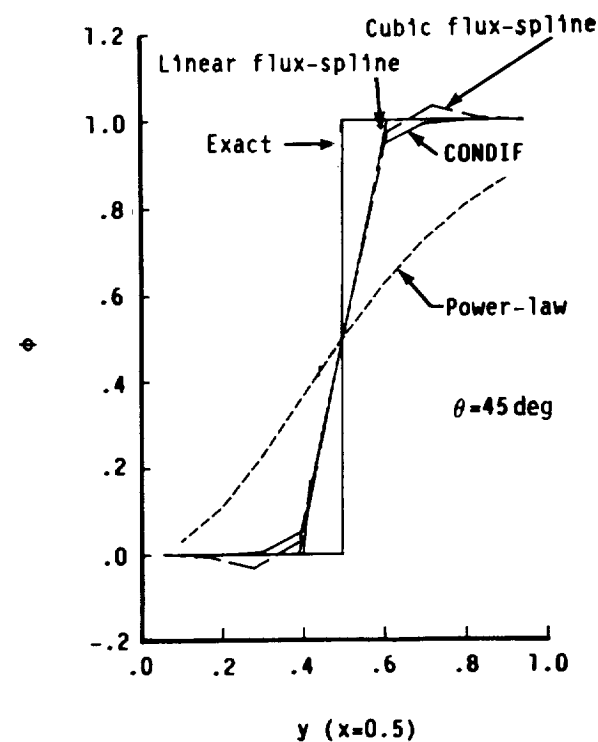
(a)



(b)



(c)



(d)

Figure 16. Convective transport of a step change in  $\phi$ ; profiles at the vertical midsection of the computational domain.

TE86-1294A

improved schemes are less smeared than those from the Power-law differencing scheme. Thus, the improved schemes introduce smaller, though finite, numerical diffusion. The linear flux-spline scheme reproduces the nodally exact solution at  $\theta = 45$  deg. For this problem, the flux-spline schemes also suffer from lack of boundedness. These oscillations are an indication of the dominance of the "flux" source terms at high Peclet numbers. The CONDIF results, on the other hand, do not show any oscillation.

The over- and undershoot problem is inherent with most higher order discretization schemes. Various bounding strategies have been proposed to eliminate the unrealistic oscillations in the numerical solution. However, there is little experience with such methods.

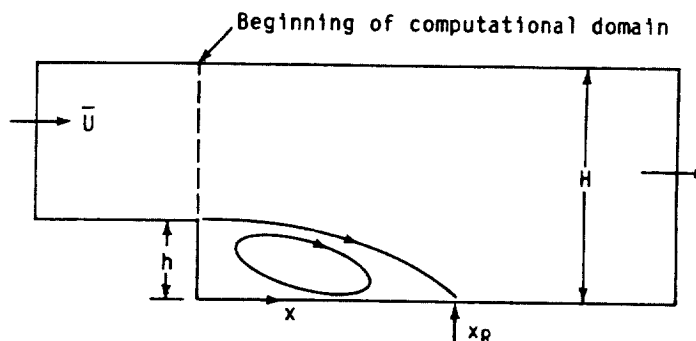
The oscillations associated with the improved schemes would diminish as the computational grid is refined. Further, in most practical problems, the presence of physical diffusion will suppress these wiggles. With these points in mind, the presence of oscillations in the solution for this purely convective flow was not considered a serious shortcoming of the improved schemes.

The next set of test problems involves the calculation of fluid flow. This requires an algorithm for the evaluation of the pressure field. For the results reported here, the SIMPLE algorithm or its improved variant SIMPLER were used. These algorithms are based on a two-point differencing for pressure. The cubic flux-spline scheme is based on a cubic profile for the mass flux ( $\rho U$ ) and the flux of the dependent variable. To preserve the accuracy characteristics of the cubic flux-spline scheme, a higher order representation of the pressure distribution is required. This calls for further research and development work, which was not undertaken in the present program. Thus, the fluid flow calculations presented next have been made using the linear flux-spline and CONDIF schemes only. Also, the linear flux-spline scheme has been simply referred to as the flux-spline scheme.

#### 4.1.2 Laminar Flows

##### 4.1.2.1 Laminar Flow over a Backward-Facing Step

The laminar flow over a backward facing step was computed using three convection-diffusion schemes--Power-law, flux-spline, and CONDIF. The configuration for this test case is shown in Figure 17. Results were obtained for two values



TE86-4099B

Figure 17. Flow over a backward facing step.

of Reynolds number, 100 and 715. The Reynolds number is based on the mean velocity in the inlet channel and the hydraulic diameter of this channel. The computed results are compared with the experimental data of Haas (Ref 14). The expansion ratio  $H/h$  is 2.

The computational domain extended from the inlet plane to eight step heights downstream for  $Re = 100$  and 32 step heights downstream for  $Re = 715$ . A fully developed velocity profile was prescribed at the inlet, and streamwise diffusion was neglected at the downstream boundary. The results were obtained using a  $22 \times 22$  grid for  $Re = 100$ , whereas a  $32 \times 22$  grid was used for  $Re = 715$ . The grid spacing was uniform in the transverse direction and increased geometrically with an expansion ratio of 1.05 in the axial direction.

Figure 18 shows the computed and measured axial velocity profiles at various streamwise locations for  $Re = 100$ . At this low Reynolds number, there is very small false diffusion, and consequently, all three schemes give results that are in good agreement with the experimental data. The results from the flux-spline scheme show slightly better agreement with the experiments. For this case, CONDIF was run with both  $R_{max} = 1$  and 10. Both values of  $R_{max}$  gave similar results, indicating, as expected, that false diffusion is negligible.

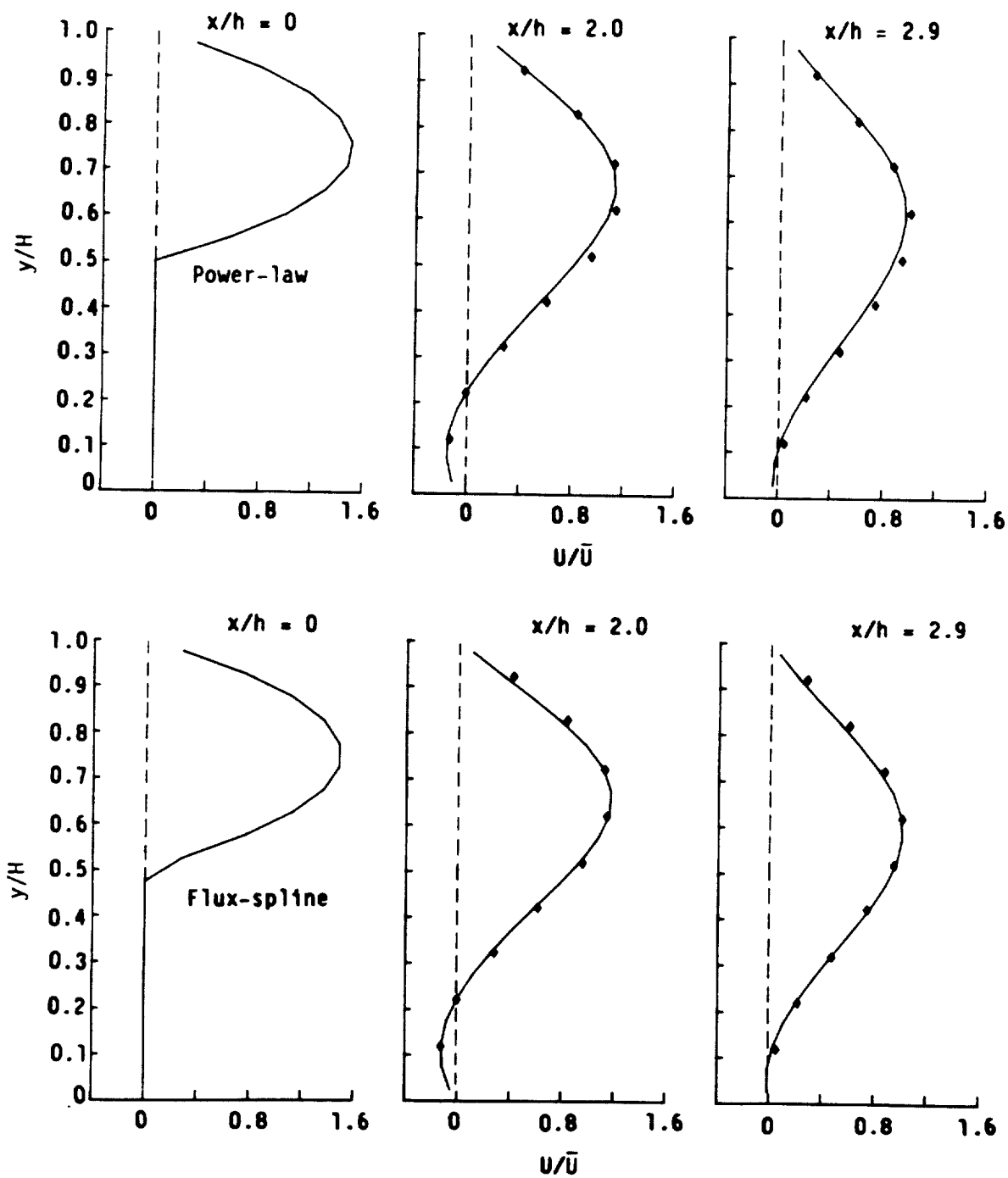
The results at  $Re = 715$  are shown in Figure 19. Notice that even though the use of improved schemes leads to better agreement between the experimental data and predictions at stations near the inlet, there is considerable discrepancy near the experimentally measured reattachment point ( $x = 13.3 h$ ). Similar behavior has also been noticed by other investigators (e.g., Ref 15) and is attributed to the deviation of the flow from two-dimensionality at this Reynolds number. However, it should be mentioned that the reattachment length predicted by flux-spline (10.6 h) and CONDIF (8.2 h) is longer than that from Power-law (7.2 h). This indicates a reduction in the false diffusion with the use of higher-order schemes. The longer reattachment length predicted by the flux-spline scheme compared with CONDIF implies that there is less numerical diffusion in the former.

#### 4.1.2.2 Flow and Heat Transfer in a Driven Cavity

The flow in a square cavity, with a moving wall (Figure 20), is a commonly used test problem for assessing the accuracy of recirculating flow calculations. Here in addition to the fluid flow, heat transfer calculations were also made. The temperature boundary conditions used were the moving wall at a temperature of unity and the remaining walls at a temperature of zero. The Prandtl number of the fluid was taken as unity.

The problem was solved for a Reynolds number, based on the wall velocity and the cavity height, of 400 on a uniform  $22 \times 22$  grid. The computed results are compared with a fine-grid ( $82 \times 82$ ) Power-law solution, which is labeled "REFERENCE" in the subsequent figures.

Figures 21 and 22 show the distributions of the  $u$  and  $v$  velocities along the vertical and horizontal midplanes of the cavity, respectively. The flux-spline solution on a  $22 \times 22$  compares very well with the REFERENCE solution. In fact, the two results are of comparable accuracy. The CONDIF results are also substantially more accurate than those from the Power-law differencing scheme.



TE86-2031B

Figure 18. Axial velocity profiles for  $Re = 100$ .

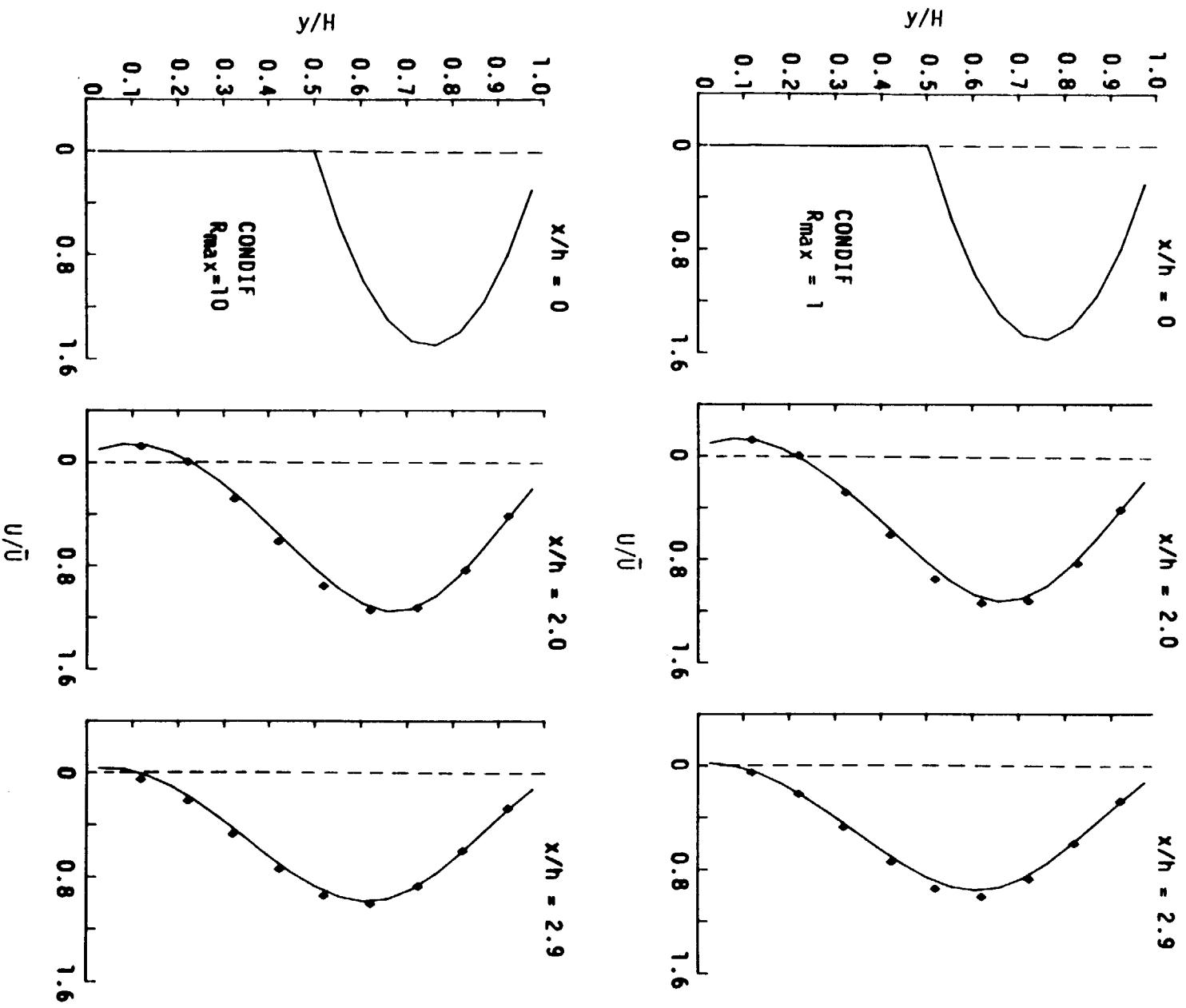
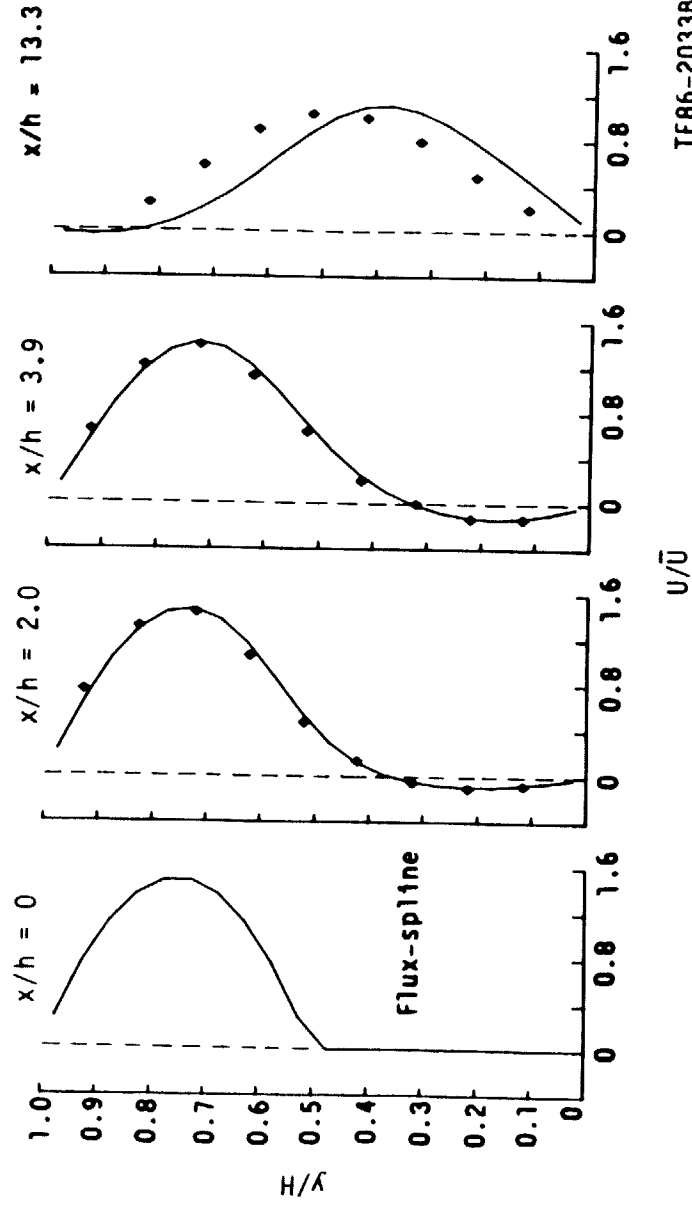
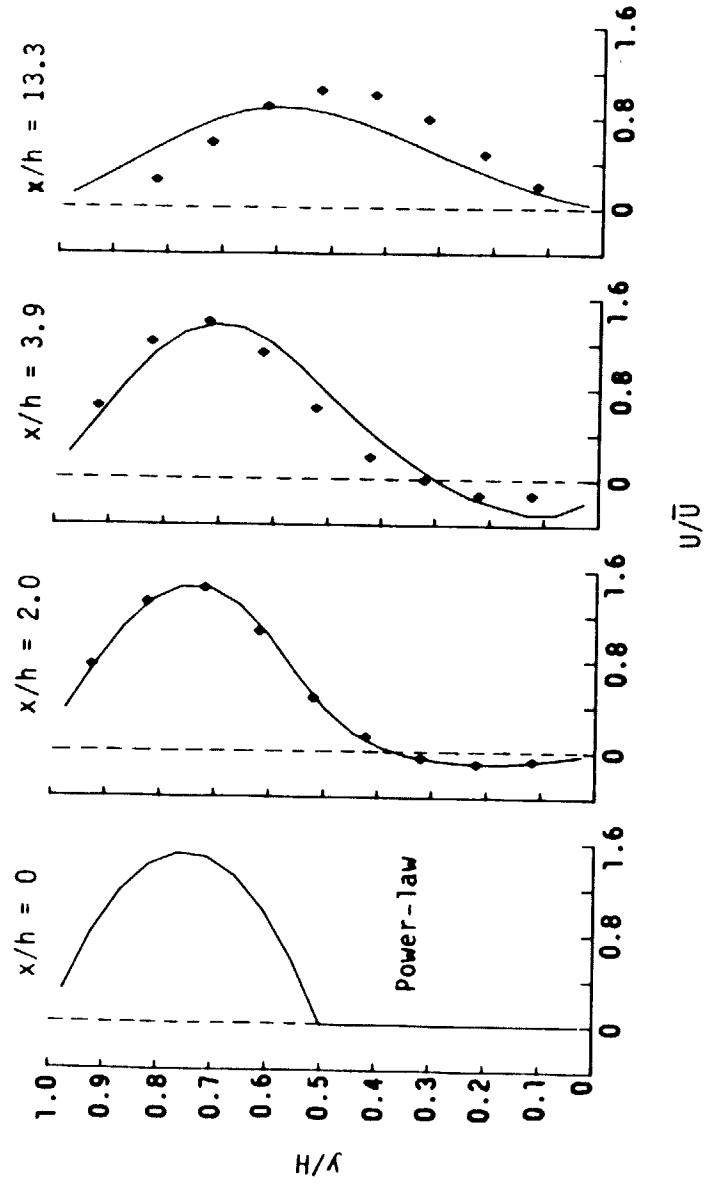


Figure 18. (continued)

TE86-2032



TE86-2033B

Figure 19. Axial velocity profile for  $Re = 715$ .

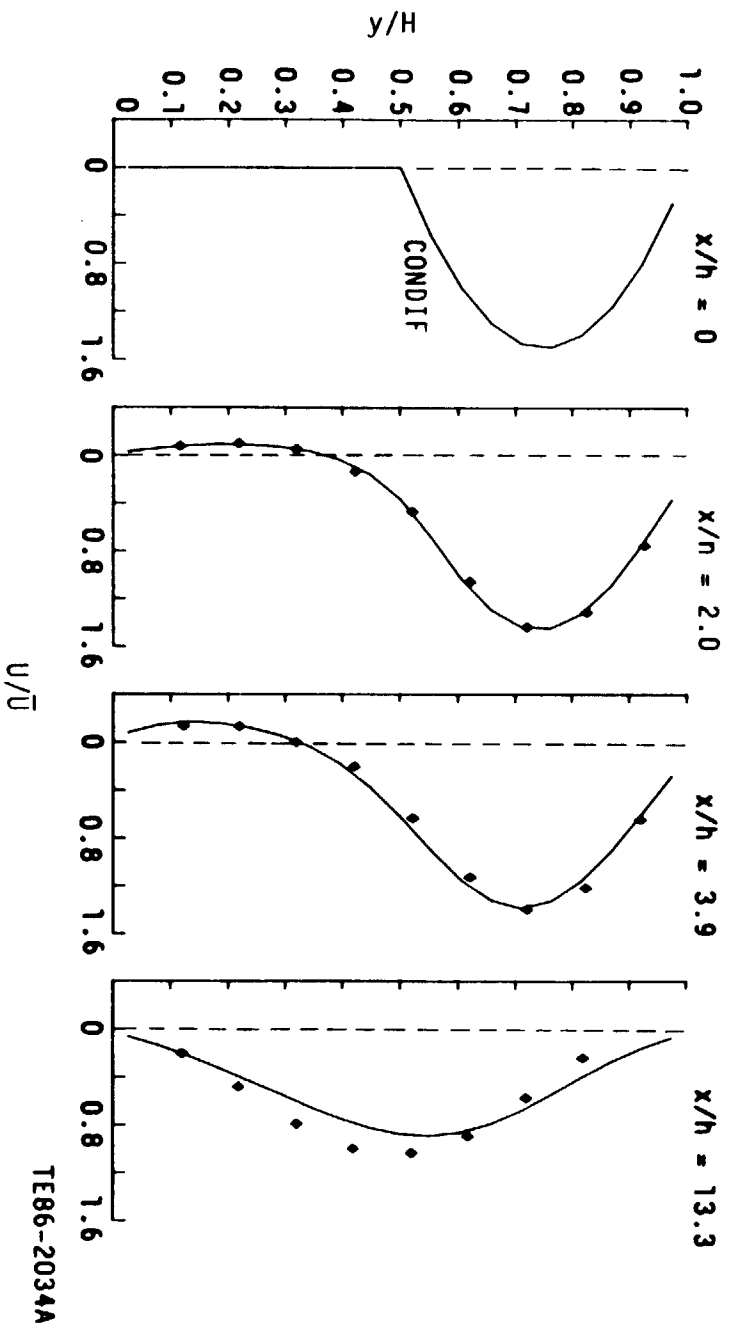
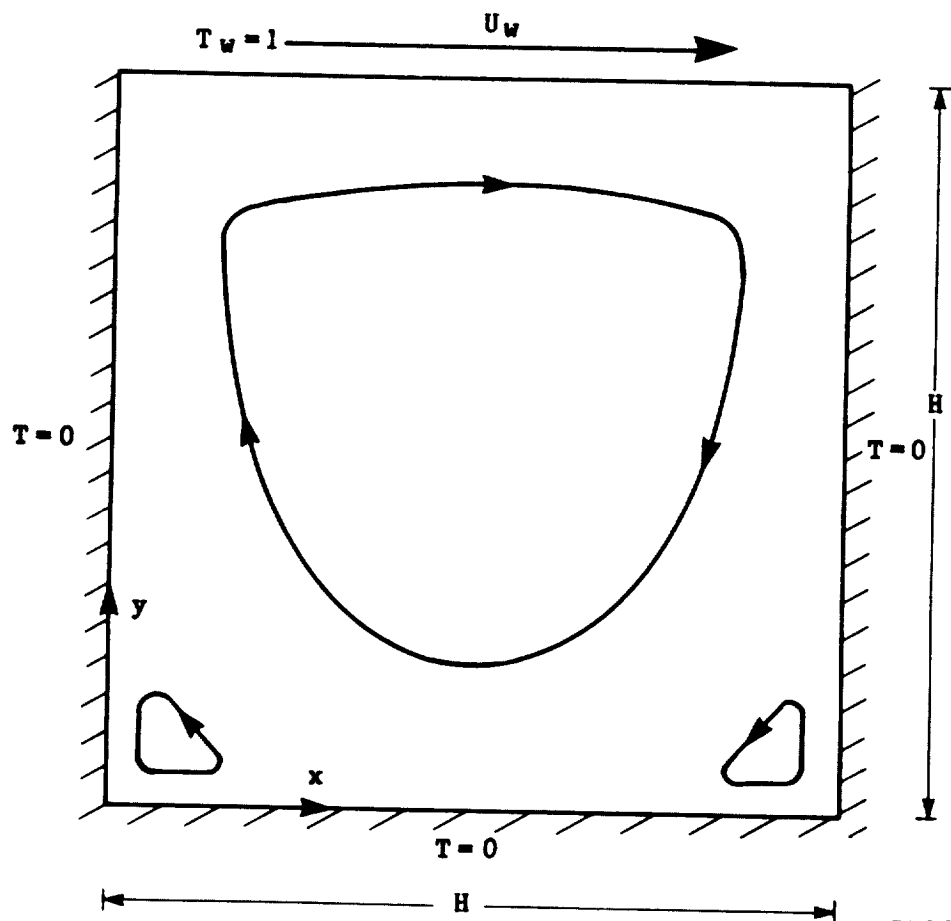


Figure 19. (continued)



TZ86-3510

Figure 20. A driven cavity.

The temperature distributions along the midsections of the cavity are shown in Figures 23 and 24. The flux-spline results are very accurate. For this problem, the CONDIF results are slightly inferior to those from the Power-law scheme (PLDS). This behavior is rather surprising since, for all other problems considered so far, CONDIF results were more accurate than PLDS results. This point needs further investigation and was considered beyond the scope of the present work.

The flow in this test case is strongly recirculating. In addition, the pressure gradients, which appear as sources in the momentum equations, are also significant. The accuracy of the flux-spline results demonstrates the capability of the scheme to respond to flow skewness and presence of sources. Use of improved schemes, which do not account for the presence of sources, such as the skew upwind differencing scheme (Ref 7), for this problem will lead to results that are only marginally better than those from the Power-law scheme.

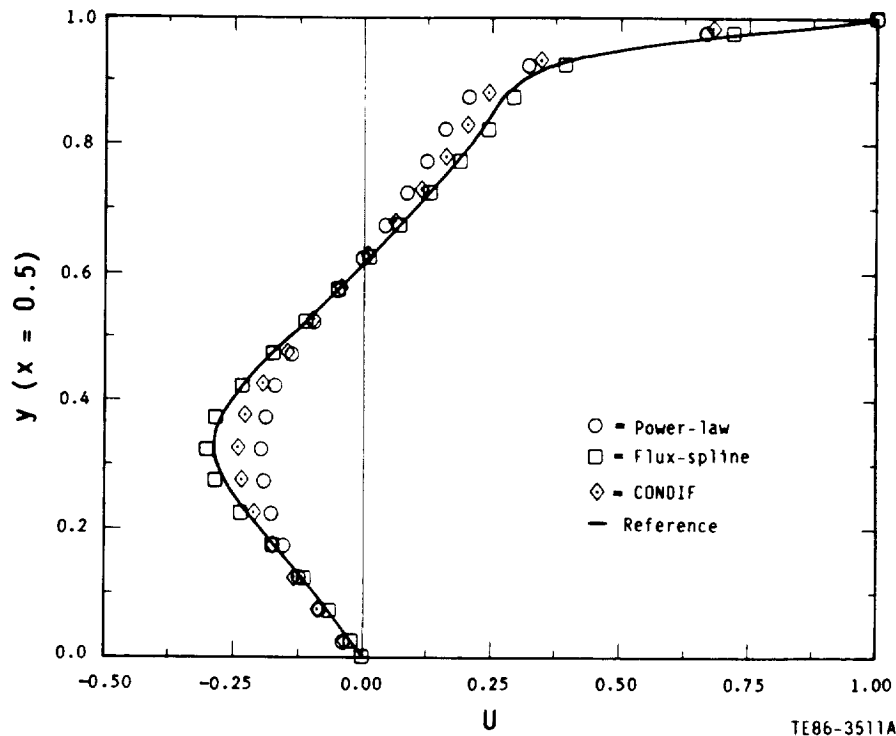


Figure 21. The  $u$ -velocity profile at the vertical midsection of the cavity.

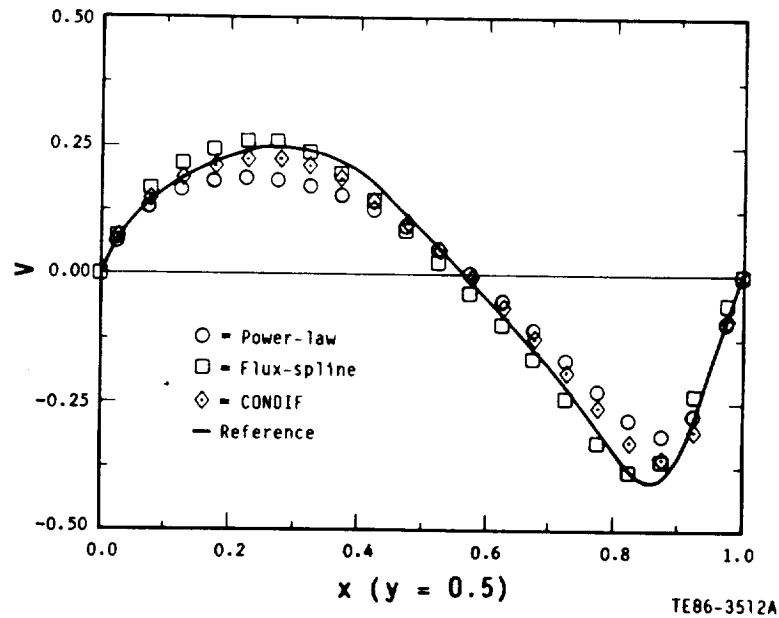


Figure 22. The  $v$ -velocity profile at the horizontal midsection of the cavity.

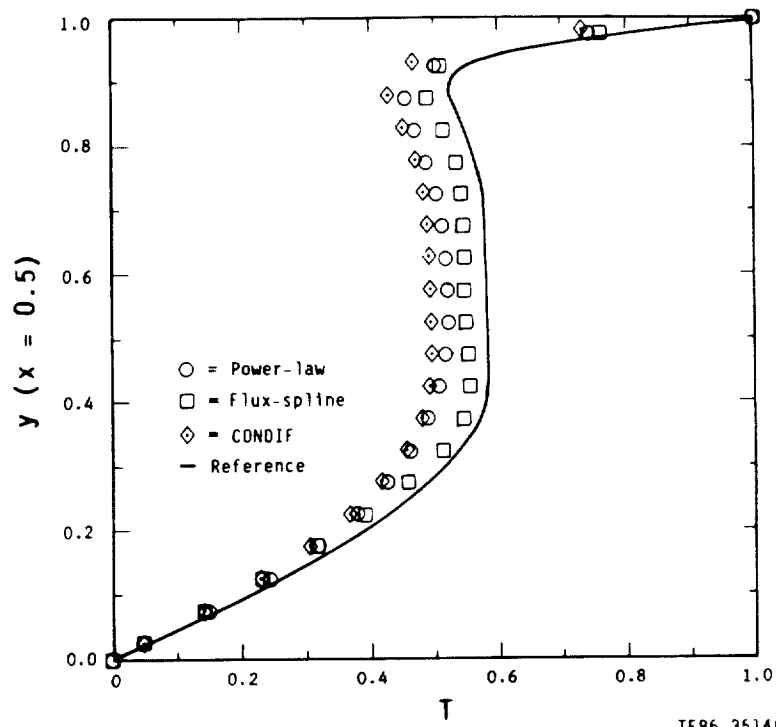


Figure 23. Temperature profile at the vertical midsection of the cavity.

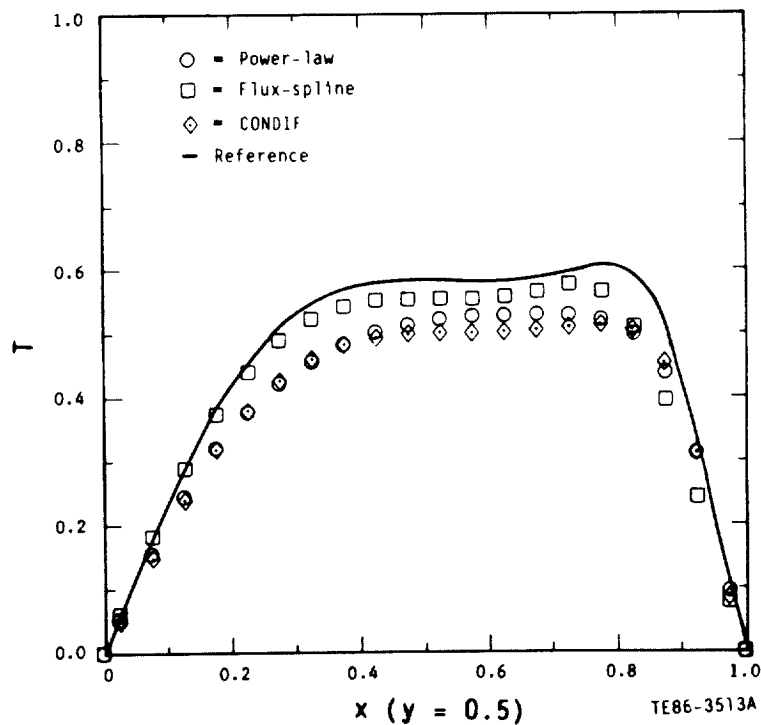


Figure 24. Temperature profile at the horizontal midsection of the cavity.

### 4.1.3 Turbulent Flows

#### 4.1.3.1 Turbulent Flow over a Backward Facing Step

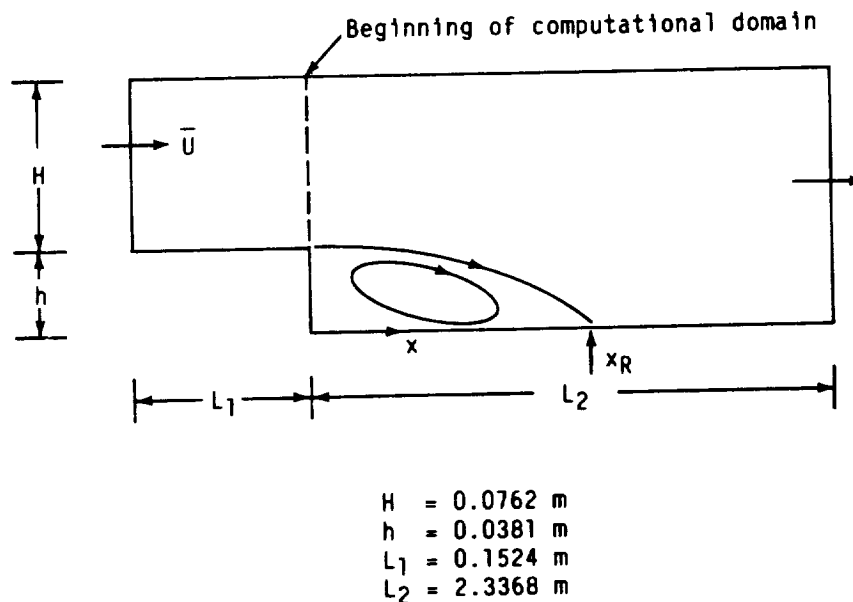
The first turbulent flow test case considered is the flow over a backward facing step designated as Stanford case 0421 (Ref 16).

The geometry of the test case is shown in Figure 25. The computational domain extended from the inflow boundary, shown dashed in Figure 25, to 20 step heights downstream. Initially, calculations were made using plug profiles at the inlet. These results were used for studying the effect of grid refinement as well as for a preliminary evaluation of the two improved differencing schemes. This was followed by calculations with inlet conditions corresponding to the experiment of Kim (Ref 17). In the experiment, velocity and turbulence data were not measured at the same locations. Velocity profiles are available at the step and at a distance four step heights upstream. Some turbulence data are also available upstream of the step. To prescribe the conditions at the step, the following approach was taken. For the Power-law scheme, the region upstream of the step was included in the computational domain. A stepwise approximation to the experimentally measured velocity profile was prescribed at the inlet, and the kinetic energy and the dissipation rates were calculated as follows:

$$k = 0.0045 \bar{U}^2$$

$$\epsilon = 3 k^{1.5}/H$$

where  $\bar{U}$  is the mean velocity in the upstream channel. The predicted profiles at the step were used as inlet conditions for the flux-spline and CONDIF schemes.



TE86-4099

Figure 25. Geometry for turbulent flow over a backward facing step.

Table II.  
Turbulent flow over a backward facing step--  
calculated reattachment lengths[ $x_R/h$ ]\*.

<u>Grid</u>	<u>Inlet profiles</u>	<u>Power-law</u>	<u>CONDIF</u>	<u>Flux-spline</u>
32 x 32	Plug	4.4	4.2	4.6
40 x 40	Plug	5.0	4.5	5.3
57 x 57	Plug	5.2	---	5.3
57 x 57	Measured	5.3	---	5.7

\*Measured value =  $7 \pm 1$

Results were obtained using three grid configurations of varying fineness. The first grid was a uniform 32 x 32 grid selected without regard to the flow gradients. The second grid was a 40 x 40 nonuniform grid with more grid points near the walls and in the shear layer. Finally, computations were made on a nonuniform 57 x 57 grid to ensure grid independence.

The overall accuracy of the computations can be judged by comparing the predicted reattachment lengths with the measured value ( $7 \pm 1 h$ ). The calculated reattachment lengths are presented in Table II. The flux-spline scheme shows an improvement over the Power-law scheme. Further, the flux-spline results reach an asymptotic value more quickly than those from the Power-law scheme, which requires further grid refinement.

The use of the CONDIF scheme results in a smaller reattachment length compared with the Power-law scheme. This behavior is contrary to that shown by other improved schemes including flux-spline. The cause for this behavior shown by CONDIF needs further investigation. Consequently, the fine grid calculations were not made using CONDIF.

The agreement between the calculated and measured results improves slightly when the measured profiles are prescribed at the inlet. Even then, considerable discrepancies remain between the two sets of results. Because the flux-spline results did not change as the grid was refined from 40 x 40 to 57 x 57, the present flux-spline results can be considered grid-independent. Some further diagnostic runs were carried out by varying the inlet turbulence kinetic energy and dissipation length scale, but these changes had no influence on the reattachment length.

The underprediction of the reattachment length for this problem has been noted in several previous studies (e.g., Ref 16, 18) and probably reflects a deficiency of the two-equation turbulence model.

The results for this test case, even though not conclusive, demonstrate the advantage of the improved discretization schemes in the evaluation of a physical model since they have the potential of providing a grid-independent solution without requiring an excessively fine grid.

#### 4.1.3.2 Turbulent Flow in a Shear-Driven Cavity

This test case was selected to evaluate the performance of the flux-spline scheme for a highly recirculating flow.

The configuration for this flow is identical to that shown in Figure 20. Calculations have been made at a Reynolds number of  $10^5$ . Results are presented for three uniformly spaced grids,  $22 \times 22$ ,  $42 \times 42$ , and  $62 \times 62$ . No comparison has been made with the available experimental data. Instead, emphasis has been placed on the differences between the flux-spline and the Power-law results.

Figures 26 and 27 show the velocity profiles along the vertical midsection of the cavity using the two differencing schemes on various grids. The flux-spline results show steeper gradients near the (stationary) lower wall. The flux spline results on the  $42 \times 42$  grid are essentially grid-independent and do not change as the grid is further refined. This is in direct contrast to the Power-law results that are more sensitive to grid refinement.

The effect of grid refinement is much more pronounced on the turbulence quantities. Figures 28 and 29 show the computed turbulence kinetic energy and turbulent viscosity profiles along the vertical midsection of the cavity ( $x = 0.5$ ), respectively. Both flux-spline and Power-law results on three grids have been included. Now the effects of grid refinement and differencing schemes are very clear. It is seen that the turbulence quantities are substantially under-predicted if the Power-law scheme is used, even on the finest grid. The flux-spline results approach the asymptotic limit with much fewer grid points. As the grid is refined from  $22 \times 22$  to  $62 \times 62$ , the turbulent viscosity resulting from the Power-law scheme increases almost seven times. A similar change in the grid for the flux-spline scheme causes the turbulent viscosity to change by less than 10%. Similar trends are observed in the behavior of kinetic energy.

The drastic changes in the levels of turbulent viscosity predicted by the Power-law scheme can be explained by examining the transport equations for  $k$  and  $\epsilon$ . In the central region, the shear is very small, and, therefore, the generation terms in the transport equations are negligible. However, the dissipation (sink) terms are finite. To adequately balance the nonzero sink terms, an accurate representation of the transport terms is needed. The numerical diffusion introduced by the use of the Power-law scheme will lead to a higher value of  $\epsilon$  since the sink term in its transport equation is proportional to the square of  $\epsilon$ . Since  $\epsilon$  also appears as the sink term in the  $k$ -equation, a low level of  $k$  will be predicted. Further, the sink term in  $\epsilon$  is proportional to  $1/k$ ; this causes overprediction of the levels of  $\epsilon$ . This double-edged effect results in very low values of turbulent viscosity.

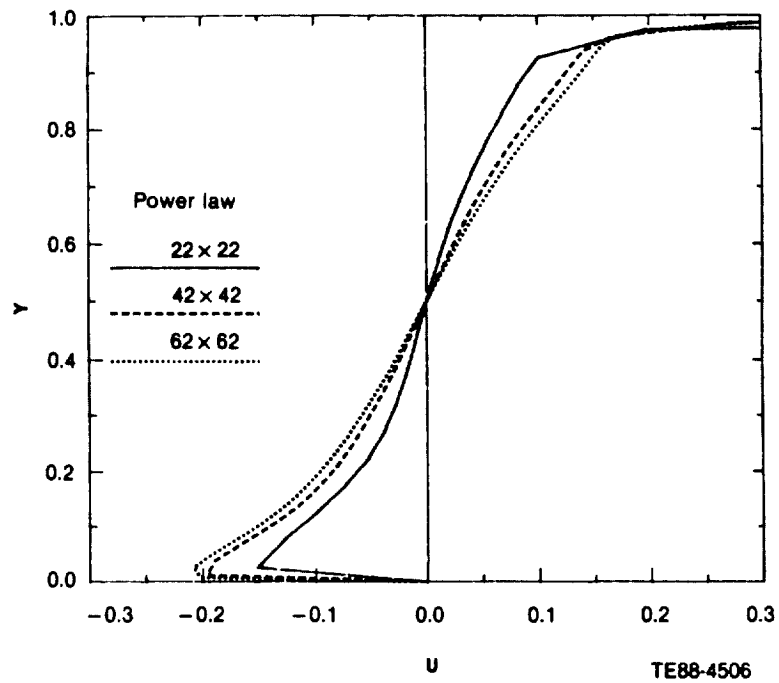


Figure 26. The u-velocity profiles along the vertical midsection of the cavity.

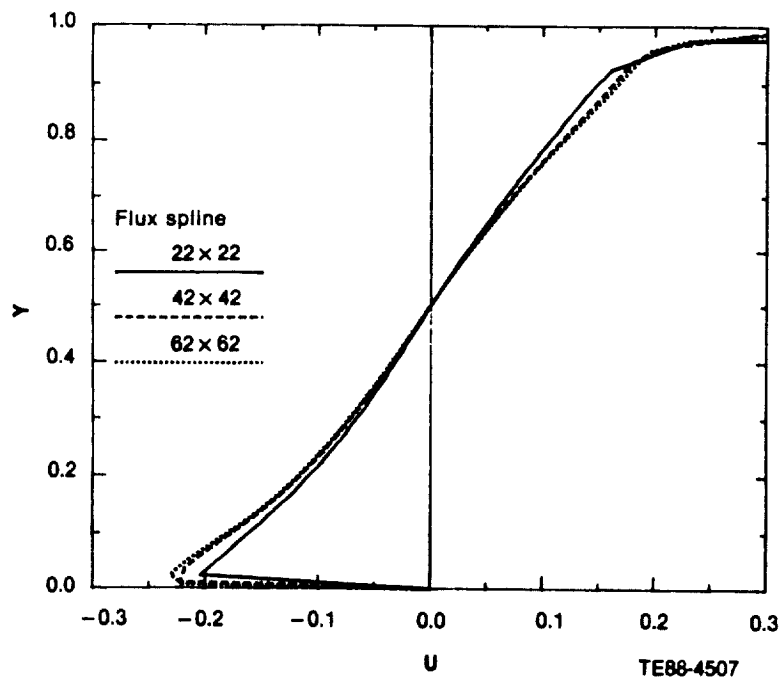


Figure 27. The u-velocity profiles along the vertical midsection of the cavity.

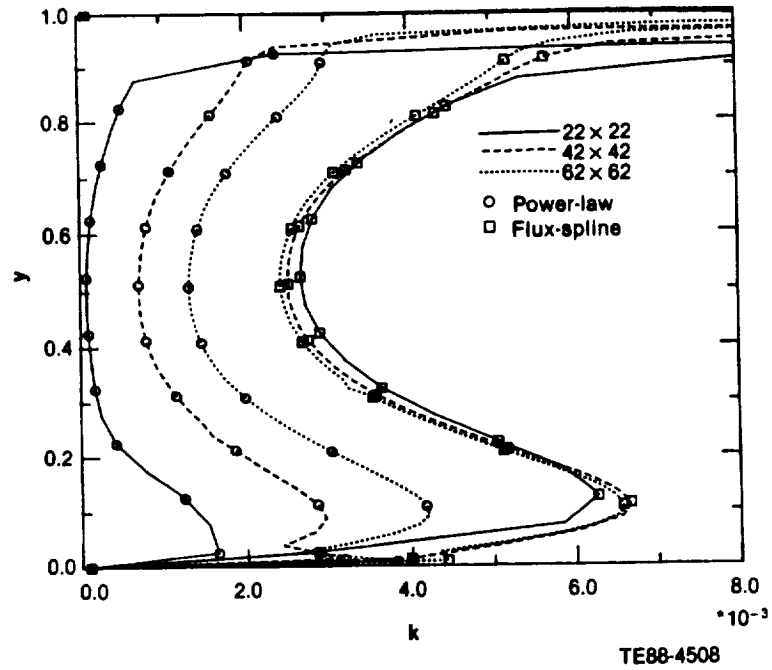


Figure 28. Turbulence kinetic energy profiles along the vertical midsection of the cavity.

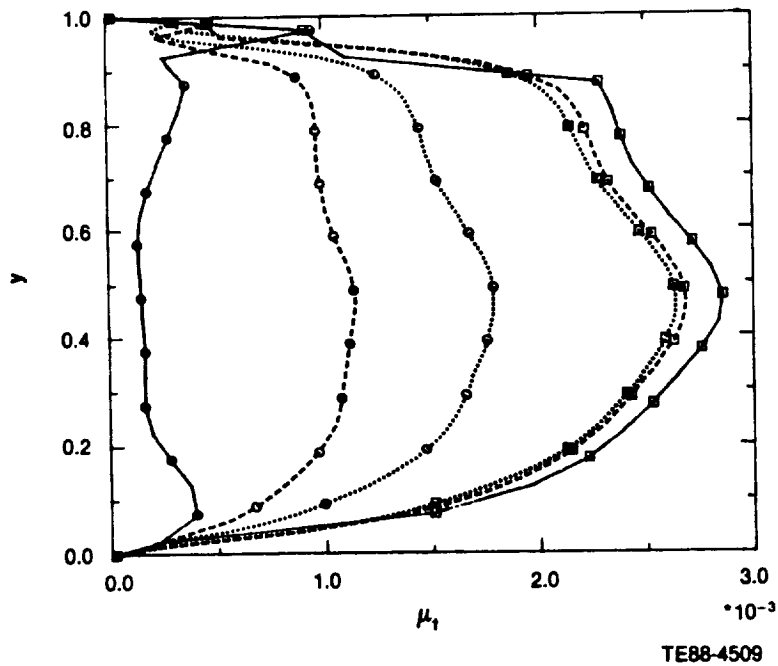


Figure 29. Turbulence viscosity profiles along the vertical midsection (for legends see Figure 28).

## 4.2 SUMMARY OF THE TWO-DIMENSIONAL TEST CASES

The performance of the three improved differencing schemes was evaluated by solving six test problems and comparing the results with available reference solutions.

For the scalar transport equations both flux-spline schemes produced very accurate results. These schemes also showed the evidence of lack of boundedness in the purely convective flow. The CONDIF results were also superior to those from the Power-law scheme. By adding a sufficient amount of numerical damping in the regions of steep gradients, CONDIF eliminated the wiggles in numerical solution. To maintain its accuracy for fluid flow calculations, the cubic flux-spline scheme would require a higher order representation for pressure also. This work was not undertaken, and the cubic flux-spline scheme was not used for fluid flow calculations.

The improved schemes showed improvement over the Power-law scheme for fluid flow calculations in both laminar flow test cases. The linear flux-spline scheme results were more accurate than those from CONDIF. A rather surprising finding was the inferior performance of the CONDIF scheme for heat transfer calculations in the shear-driven cavity. However, in an earlier problem involving the transport of a scalar in a recirculating flow, CONDIF results were more accurate than those from the Power-law scheme. This behavior of CONDIF requires further investigation.

For the turbulent flow test cases, the flux-spline scheme was superior to the Power-law scheme. For the flow over the backward facing step, the use of CONDIF resulted in a reattachment length that was shorter than that predicted by the Power-law scheme. This behavior is contrary to that shown by other improved schemes for this problem.

For the fluid flow calculations reported here, the flux-spline results were obtained using the SIMPLER algorithm (Ref 1) and the CONDIF results were obtained with the SIMPLE algorithm (Ref 1). For both schemes, the algebraic equations were solved using a line-by-line tridiagonal matrix algorithm (TDMA). No convergence difficulties were encountered with either scheme.

## 4.3 SELECTION OF A SCHEME FOR THREE-DIMENSIONAL FLOWS

For all the test problems considered so far, the linear-flux-spline scheme consistently produced more accurate results. The computational molecule for this scheme involves only seven points in three dimensions. Further, due to the one-dimensional nature of the spline-continuity conditions (even for a multi-dimensional problem), the extension of linear flux-spline scheme to three dimensions is relatively straightforward. Due to these attributes, the linear flux-spline scheme was selected for incorporation into a computer program for three-dimensional flows.

#### 4.4 THREE-DIMENSIONAL TEST CASES

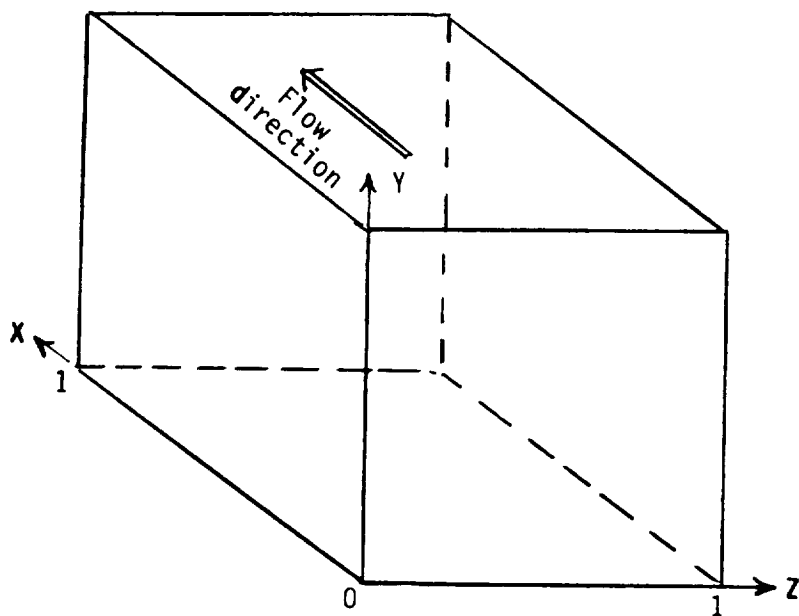
##### 4.4.1 Laminar Flow

The flow situation under consideration is shown in Figure 30. Due to symmetry considerations, the computational domain extended only half the cavity width in the lateral ( $z$ ) direction.

Computations have been made at a Reynolds number, based on lid velocity and cavity depth, of 400. Results have been obtained using a uniformly spaced  $22 \times 22 \times 12$  ( $x, y, z$ ) grid. The present numerical results have been compared with the solution of Ku et al. (Ref 19) obtained using a pseudo-spectral method ( $25 \times 25 \times 13$  modes). This solution has been designated as "REFERENCE" in the subsequent figures.

Figures 31 and 32 show the velocity profiles of the  $u$ -component on the vertical centerline and  $v$ -component on the horizontal centerline of the symmetry plane  $z = 0.5$ , respectively. The flux-spline results are in better agreement with the reference solution than the Power-law results. In particular, the flux spline results exhibit sharper peaks than the Power-law solution due to less numerical diffusion in the former.

The flow patterns in the  $y$ - $z$  plane at  $x = 0.5$  obtained using the two discretization schemes are shown in Figure 33. The flux spline scheme predicts a more intense flow in the lower section of the cavity, especially in the vicinity of the eye of the vortex.



TE87-6043

Figure 30. Three-dimensional cubic cavity.

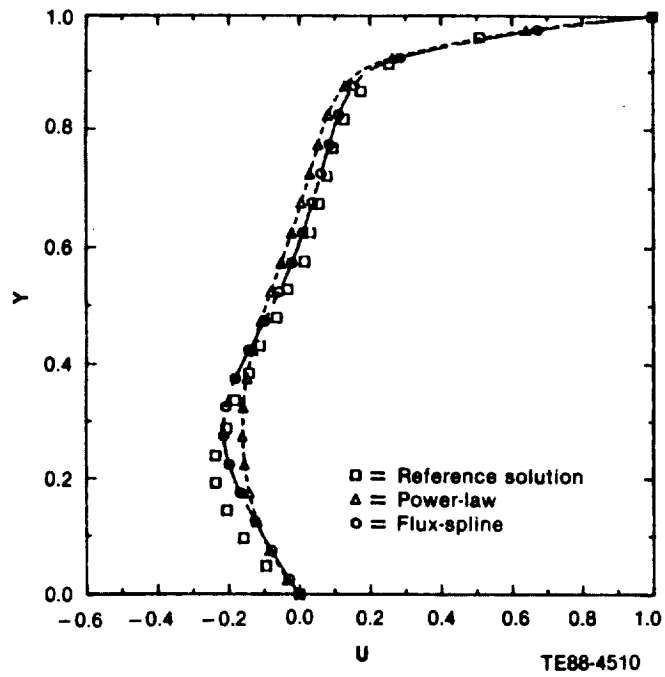


Figure 31. The  $u$ -velocity profile along the vertical centerline of plane  $z = 0.5$ .

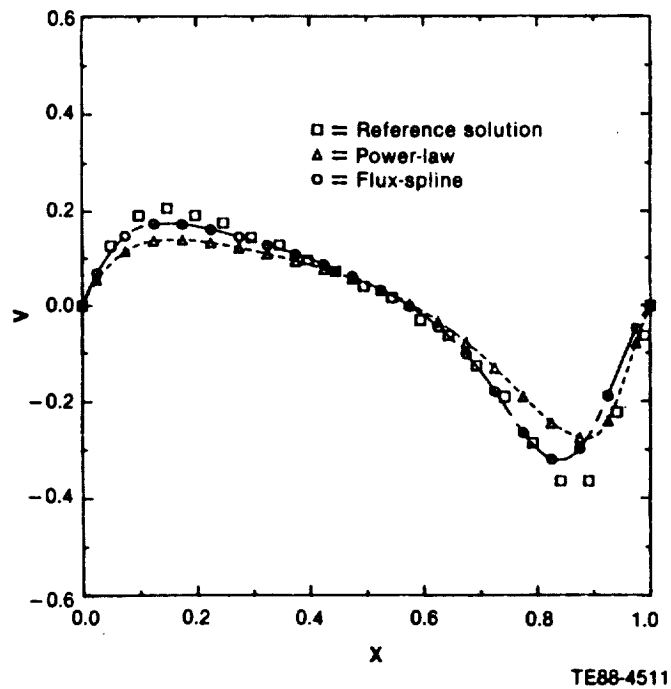
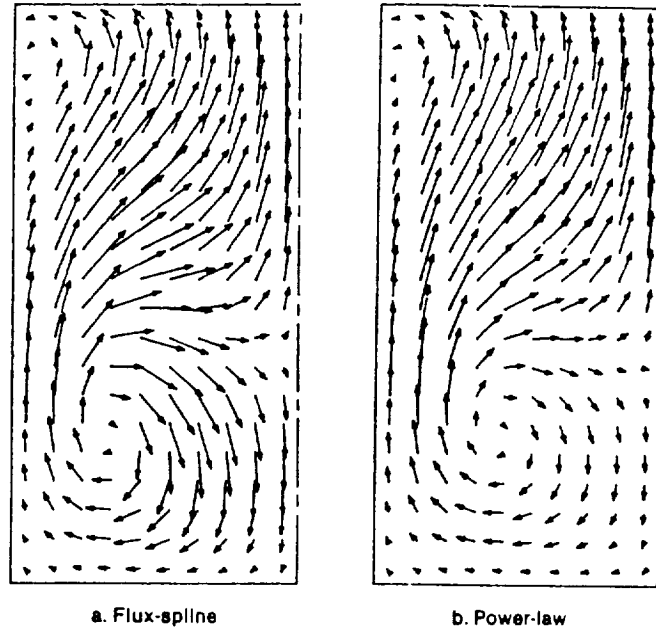


Figure 32. The  $v$ -velocity profile along the horizontal centerline of plane  $z = 0.5$ .



TE88-4512

Figure 33. Shear driven cavity: flow pattern in the y-z plane at  $x = 0.5$ .

#### 4.4.2 Turbulent Three-Dimensional Jet-Induced Flow in a Duct

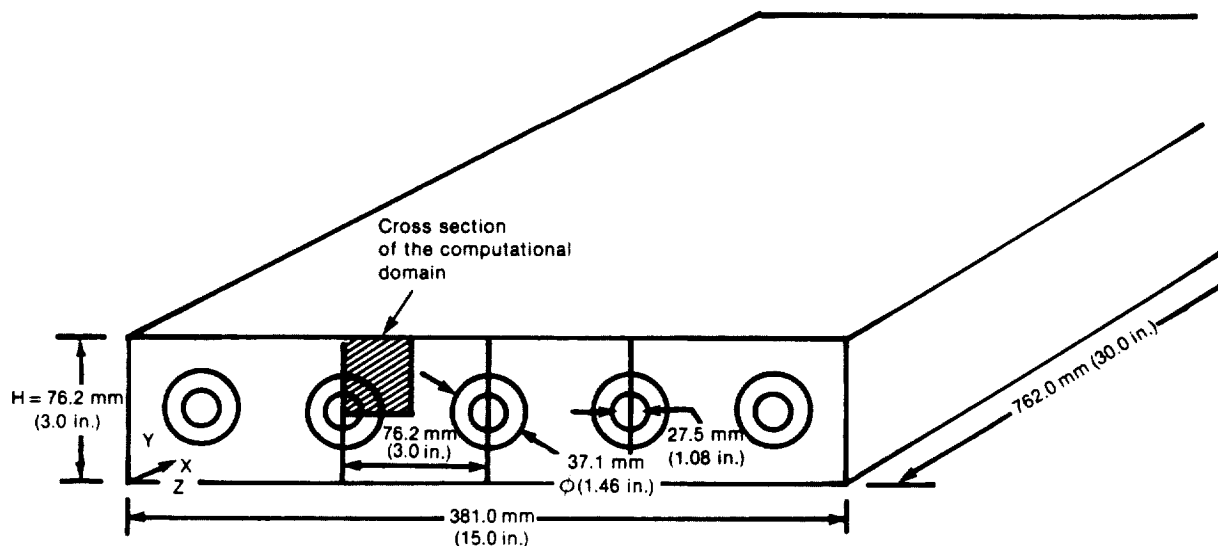
##### 4.4.2.1 Three-Dimensional Annular Jet-Induced Flow in a Duct

This test case is one of the experiments being conducted under NASA HOST Element B for turbulence model evaluation. The test rig, shown in Figure 34, consists of five annular swirling or nonswirling streams issuing into a duct of rectangular cross section. There is provision for radial jets at specified axial locations. For the present test case, all streams are nonswirling and there are no primary jets. Due to symmetry of the problem, the computational domain includes only one quarter of an annular stream. In the cross section, the computational domain is bounded by symmetry lines in the z-direction and by a symmetry line and a wall in the y-direction.

In the streamwise direction, the computational domain extended from the inlet plane to four duct widths downstream. Experiments indicated rather small changes in the velocity distributions beyond this location.

Computations were made on two grids,  $22 \times 17 \times 17$  and  $37 \times 27 \times 27$ . In the first grid, which will be referred to as "coarse," the grid spacing was uniform in the cross section. In the refined grid, to be referred to as "fine," a finer spacing was used within and near the jet. In both cases, the grid spacing in the x-direction was finer near the inlet.

This test problem was solved using the Power-law and flux-spline schemes. Like the previous turbulent flow test cases, the emphasis has been placed on the differences between the results from these schemes, and very limited comparison has been made with the experimental data. This has been done primarily because



TE88-4513

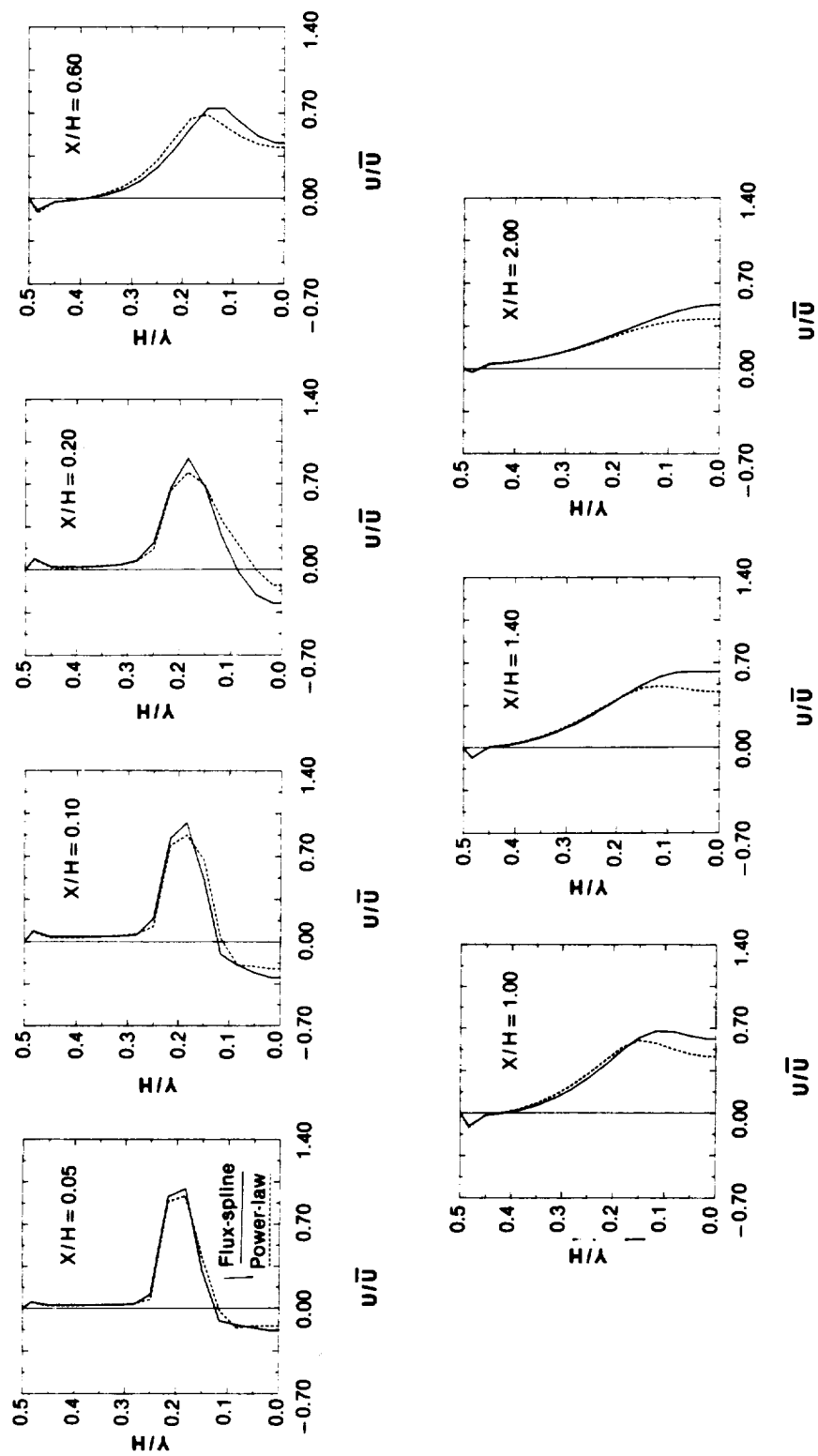
Figure 34. Geometry for an annular jet-induced flow in a duct.

there is still considerable uncertainty about the adequacy of the turbulence model for such flows. Thus, the disagreement between the numerical and experimental results may be due to the numerical inaccuracy or the inadequacy of the turbulence model. However, for a given turbulence model,  $k-\epsilon$  model in this study, the flux-spline results are more accurate.

Figure 35 shows the axial velocity profiles on the  $z = 0$  plane (containing the centerline of the annular stream) at selected streamwise locations obtained using the coarse grid. For this calculation, plug profiles were prescribed at the inlet plane because the grid in the cross section was too coarse to allow for a distribution of various quantities. The use of the flux-spline scheme results in sharper peaks and a longer recirculation zone at the center. At all streamwise locations, the profiles resulting from the Power-law scheme are more smeared than those from the flux-spline scheme. This trend indicates the presence of excessive numerical diffusion in the Power-law solution.

Figure 36 shows the comparison of the predicted centerline velocity distribution with the experimental data. The flux-spline results are in better agreement with the experimental data at locations near the inlet. However, further downstream the velocity is considerably underpredicted.

The results for the fine grid are displayed in Figure 37. For this calculation, the experimentally measured profiles of axial velocity and kinetic energy were prescribed at the inlet. The trends observed in the coarse-grid solutions are also noticed in this grid. The flux-spline scheme is able to preserve the peaks and produces profiles that are less smeared. Both schemes respond to grid refinement, especially near the inlet. To ensure grid-independence, calculations on a still finer grid would be required.



TE88-4514

Figure 35. Axial velocity profiles at  $z = 0$  plane, coarse grid.

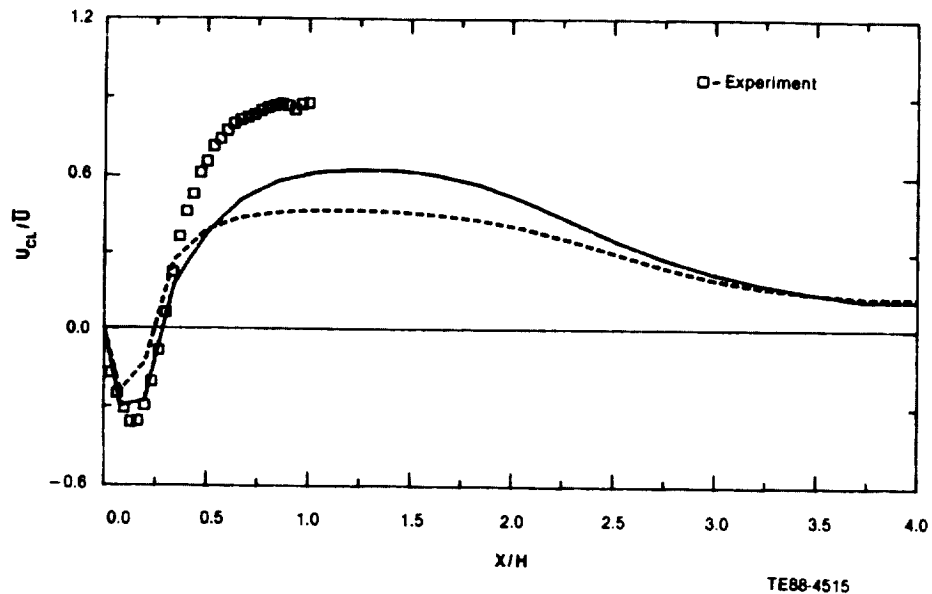


Figure 36. Variation of the centerline axial velocity, coarse grid (for legend see Figure 35).

Due to the limitations of the resources, a further grid refinement was not undertaken. However, based on the experience with two-dimensional flows, the flux-spline results are not expected to change significantly as the grid is further refined.

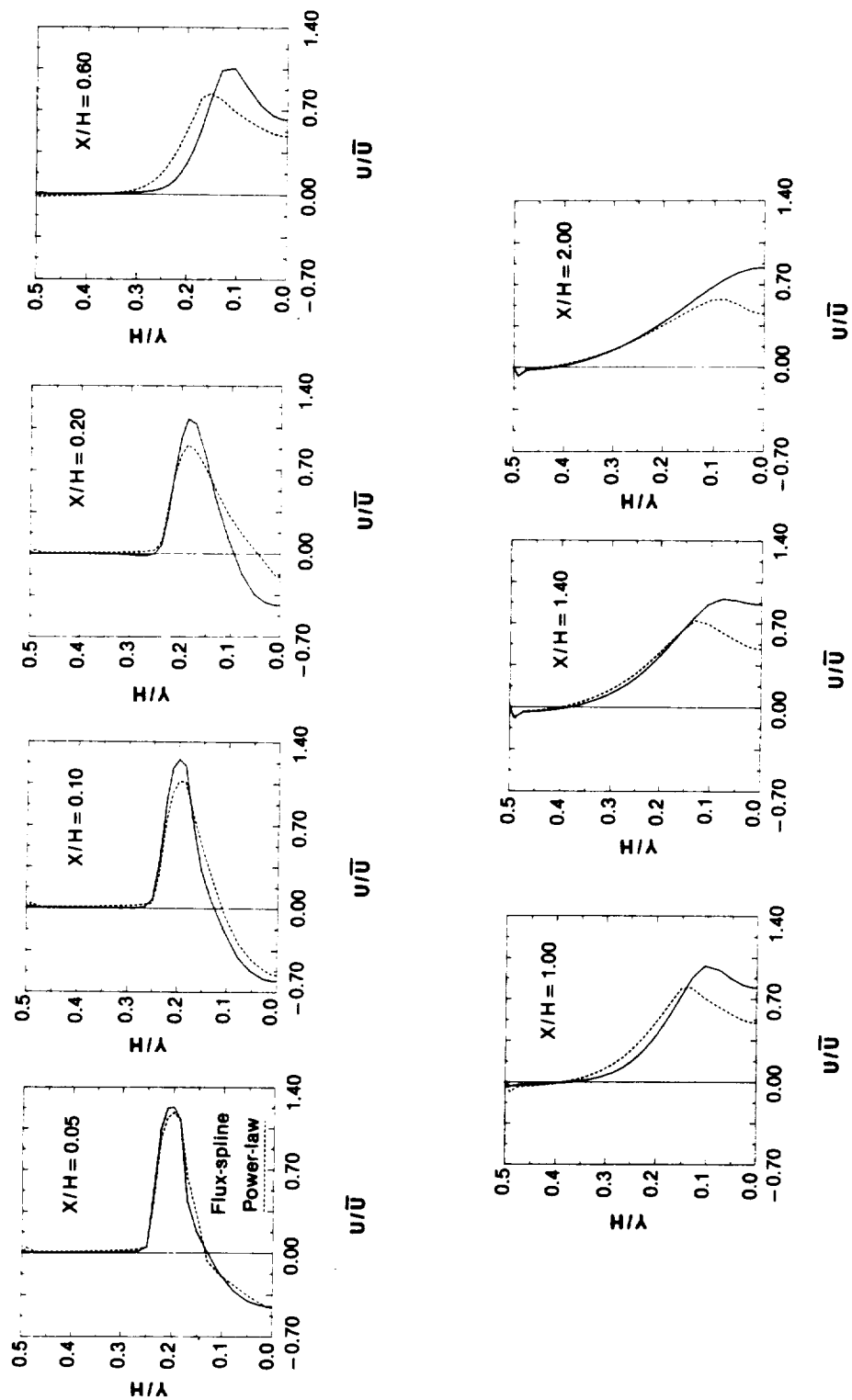
Figure 38 shows the computed centerline velocity variation on the fine grid. The flux-spline results are in good agreement with the experimental data. Both sets of calculations, however, now predict a stronger recirculation zone.

#### 4.4.2.2 Row of Jets in Crossflow

This three-dimensional turbulent flow test case, based on the experiments of Khan (Ref 20), involves a row of jets injected normal to the main flow in a duct of rectangular cross section. The physical situation for the particular case under consideration is shown in Figure 39. The jet diameter is 0.0254 m. The pitch (jet centerline-to-centerline distance) is four jet diameters and the height of the test section is also four jet diameters.

The symmetry of the flow in the lateral ( $z$ ) direction allows the computations to be confined between the jet centerline and the centerline between the jets. In the axial direction, the computational domain extends from 5 jet diameters upstream of the leading edge of the jet to 24 jet diameters downstream of the trailing edge of the jet. In the  $y$ -direction, the computational domain extends from the floor of the wind tunnel to the roof, or four jet diameters.

At the inflow boundary ( $x/D = -5.5$ ), plug profiles were assigned for all variables. The streamwise diffusion was neglected at the outflow boundary. The



TE88-4516

Figure 37. Axial velocity profiles at  $z = 0$  plane, fine grid.

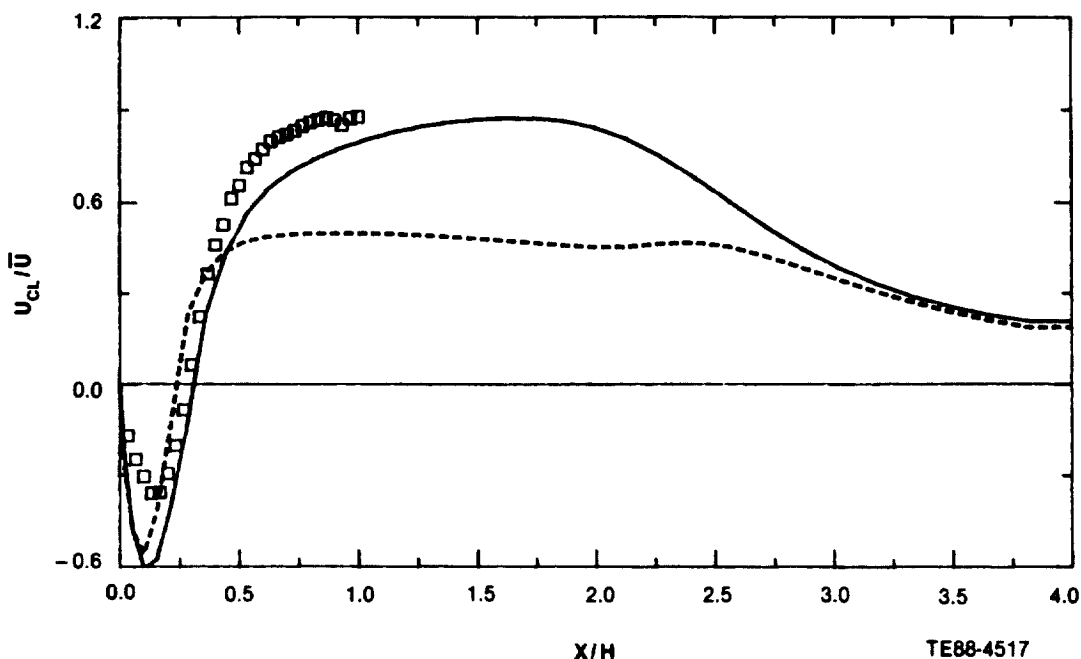


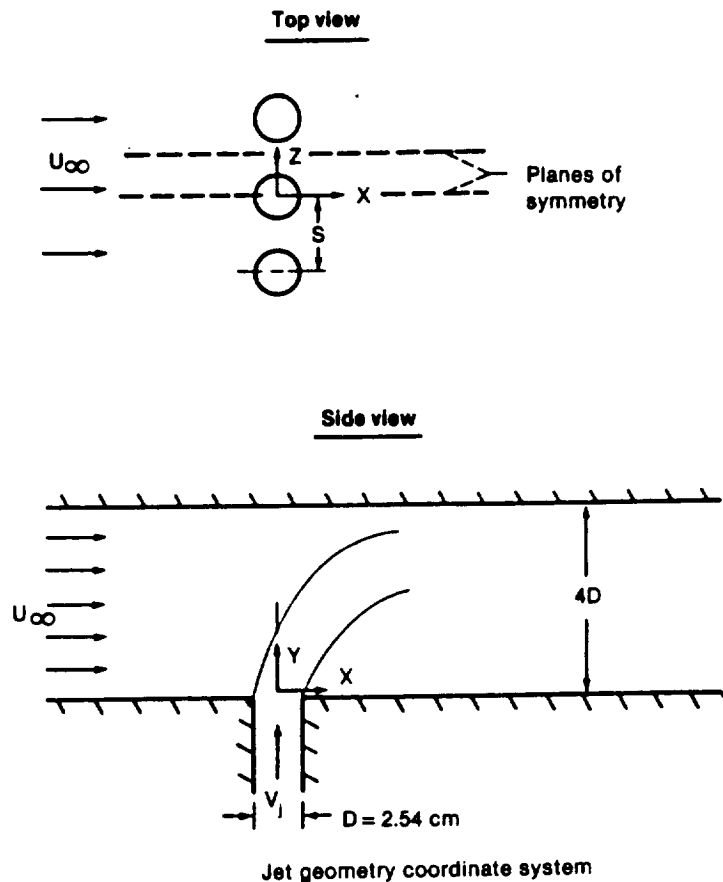
Figure 38. Variation of centerline axial velocity, fine grid.

circular jet was approximated by an equivalent area rectangle with the longitudinal side equal to the jet diameter. The profiles at the exit of the jet were also taken as uniform. These assumptions may influence the degree of agreement between the experimental data and numerical predictions. Since the primary objective of these calculations is to stress the accuracy consideration without analyzing the consequences of the turbulence model being used, these simplified boundary conditions are considered adequate.

Computations were made on two grids of varying fineness--32 x 17 x 12 (coarse) and 37 x 22 x 17 (fine). Both grids were nonuniform with finer grid spacing near the jet.

The results on the coarse grid are presented in Figure 40 in the form of the axial velocity profiles at four streamwise locations. These calculations show that both differencing schemes yield results that are significantly different from the experimental data. The numerical results, however, indicate that flux-spline calculations contain less numerical diffusion and hence are less smeared compared with those from the Power-law scheme. This is evident from the profiles at  $x/D = 4$ . The differences between the predictions and the experimental data may be due to the coarseness of the mesh used and/or the inadequacy of the turbulence model. To reduce the numerical errors, calculations were repeated on a finer grid. These results are shown in Figure 41.

The use of the fine grid reduces the differences between the results from the two differencing schemes. The smeared Power-law profile indicates the presence of excessive numerical diffusion even on this grid. Although differences between the calculated and experimental results are significant, further grid refinement may still be necessary to ensure grid independence of the present



TE88-4518

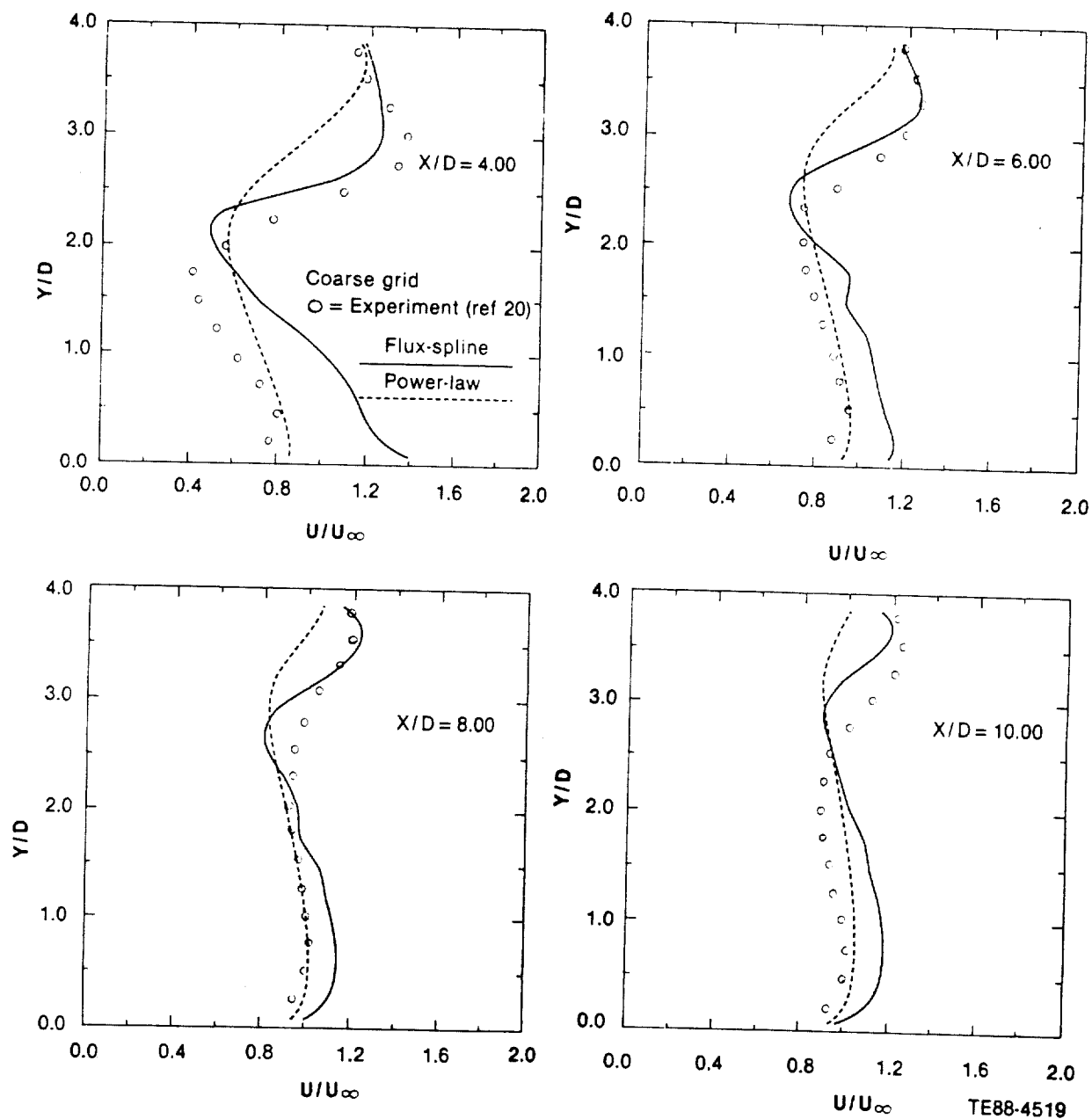
Figure 39. Flow geometry for "a row of jets in crossflow."

calculations. Calculations for the same geometry using the bounded skew upwind differencing scheme BSUDS2 (Ref 21) indicate that even a  $74 \times 42 \times 22$  grid may not be sufficient to achieve grid independence, although the use of such a fine grid was not considered in this study.

The effect of grid refinement is more pronounced on the flux-spline results, especially at  $x/D = 4$ . The Power-law scheme responds slowly to the change in grid. Such behavior is to be expected due to higher order of accuracy for the flux-spline scheme. Even on the fine grid, the Power-law solution is dominated by the false diffusion that may completely overwhelm the physical diffusion.

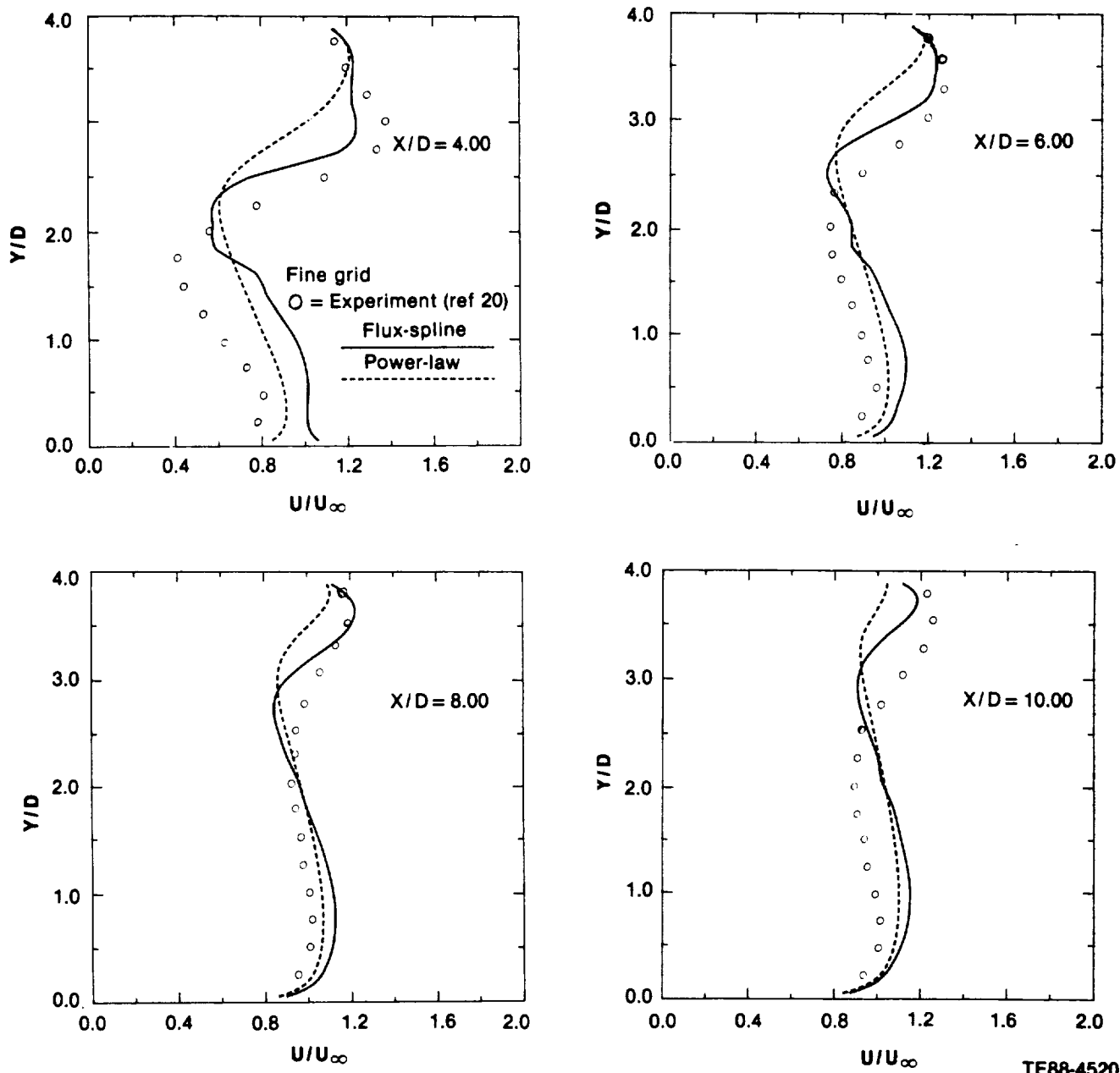
Even though there are considerable differences between the experimental results and calculations presented here, the effects of grid refinement and change of differencing scheme are very similar to those seen in an earlier study (Ref 22) for the same test case.

This test case revealed some interesting issues related to the evaluation of the differencing schemes as well as the turbulence models. These primarily concern the specification of the inlet boundary conditions for the turbulence quantities. If a diffusive scheme, such as the Power-law scheme, is used for discretizing the equations and if the flow is recirculating, i.e., there is sufficient internal generation of turbulence, the results are insensitive to



TE88-4519

Figure 40. Axial velocity profiles for coarse grid.



TE88-4520

Figure 41. Axial velocity profiles for fine grid.

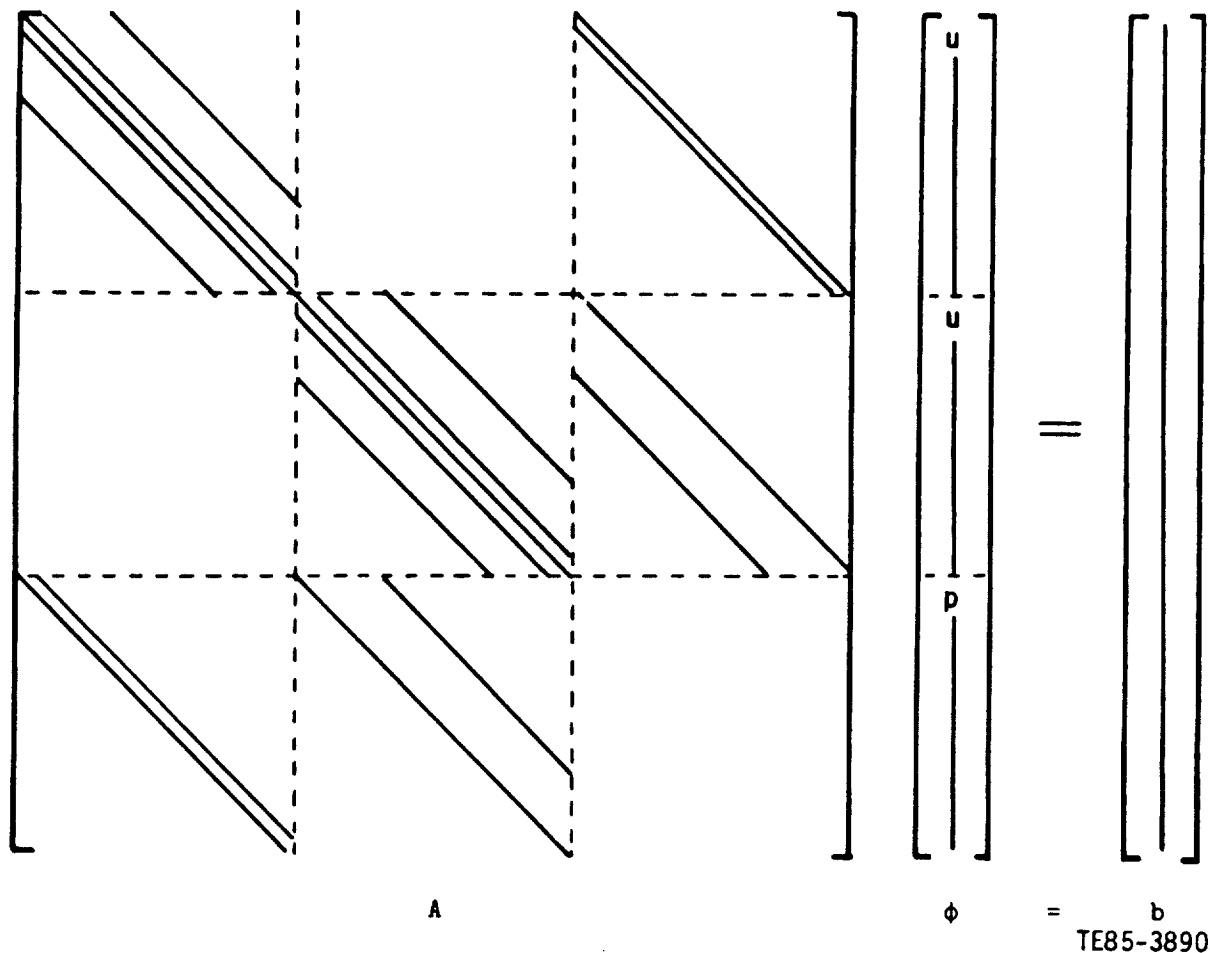


Figure 44. Structure of the coefficient matrix.

The matrix equation (148) is nominally linear because the elements of matrix A depend on the velocity components themselves, and also the source term b may be function of the dependent variables. In the present implementation, the nonlinearities are handled using the successive substitution (Picard) technique, in which the coefficients and the source terms (including those arising from the flux-spline formulation) are calculated from the values of the dependent variables from the previous iteration.

The direct solution of equation (148) was accomplished by the use of the Yale Sparse Matrix Package, YSMP (Ref 13). It solves the linear system  $A\phi = b$  by a sparse matrix variation of the LU decomposition procedure, where L and U are the lower and upper triangular matrices. YSMP selects the elements of the main diagonal of the matrix as the pivots during the decomposition process. It is, therefore, necessary that the original coefficient matrix not contain any zero element on the main diagonal. As shown in Figure 44, the absence of pressure in the continuity equation leads to zeros along the main diagonal. This difficulty can be overcome in several ways, e.g., by rearranging the equations. In the present study, small nonzero elements are introduced along the main diagonal in the continuity equation, and equation (148) is recast in terms of update vector  $\Delta\phi$  as follows:

$$A(\Delta\phi) = b - A\phi^* \quad (149)$$

where  $\Delta\phi = \phi - \phi^*$  and  $\phi^*$  is the value from the previous iteration or initial guess. Now, equation (149) is replaced by:

$$A'(\Delta\phi) = b - A\phi^* \quad (150)$$

where  $A'$  is the perturbed matrix that contains small nonzero elements along the main diagonal. Since  $A'$  is not used on the right side, the converged solution of equation (150) represents the solution of equation (148) with the continuity equation properly satisfied. An added advantage of solving the equations in terms of changes ( $\Delta\phi$ ) is that it reduces the round-off errors.

Since the repeated numeric factorization of the coefficient matrix  $A$  is an expensive process, considerable execution time can be saved by not decomposing the coefficient matrix at each iteration. Instead, the decomposed matrix from a previous iteration is used. In effect, equation (150) is replaced by

$$A^*(\Delta\phi) = b - A\phi^* \quad (151)$$

where  $A^*$  is the old matrix decomposed at an earlier iteration, but  $A$  is the current coefficient matrix. In each iteration of this type, the right side is updated and the solution is obtained by forward and backward substitution using the previously computed decomposition. The cost of such an iteration is only 10-15% of a full decomposition iteration.

## 5.2 TREATMENT OF THE TURBULENCE QUANTITIES

The turbulent flow calculations in this study are based on the  $k$ - $\epsilon$  model, which requires the solution of two additional partial differential equations, after every iteration of the flow equations, to provide a new viscosity field.

The two turbulence equations are highly coupled and nonlinear, due to their source terms, and difficult to solve. Due to these features, a direct coupled solution of these equations does not prove satisfactory and causes instabilities. Vanka (Ref 11) solves the  $k$  and  $\epsilon$  equations in a decoupled line-by-line manner by holding the other variable fixed. In the present work a slightly different approach was taken. Instead of solving the equations along a line and marching through the domain, the equations are solved sequentially over the entire computational domain using a line-by-line TDMA. The equations are solved repeatedly (typically 7 or 8 times) with updated source terms until  $k$  and  $\epsilon$  are sufficiently well converged. Such a procedure is expected to readily account for the ellipticity of the recirculating flows.

## 5.3 PERFORMANCE OF THE ALGORITHM

The coupled solution approach combined with the flux-spline scheme was applied to laminar flows in a square cavity and a planar sudden expansion and turbulent flow over a backward facing step. The details of these test cases are given in Table III. The number of iterations required for convergence and the execution times for the coupled approach are compared with those for the sequential SIMPLER algorithm in Table IV.

The performance of the coupled algorithm is nearly independent of the Reynolds number and the mesh aspect ratio. For the test problems considered, a coupled

Table III.  
Test cases.

<u>Case No.</u>	<u>Flow</u>	<u>Reynolds number</u>	<u>Grid (uniform)</u>
<u>Laminar flows</u>			
1	Cavity	400	22x22
2	Cavity	1000	22x22
3	Cavity	400	40x40
4	Cavity	1000	40x40
5	Expansion	400	22x12
6	Expansion	400	22x22
7	Expansion	400	42x22
<u>Turbulent flows</u>			
8	Backward facing step	$5.6 \times 10^5$	22x22
9	Backward facing step	$5.6 \times 10^5$	42x22

Table IV.  
Number of iterations required and execution times.

<u>Case No.</u>	<u>No. of iterations</u>		<u>Execution times*</u>	
	<u>SIMPLER</u>	<u>Direct</u>	<u>SIMPLER</u>	<u>Direct</u>
1	62	17	18	6
2	84	30	24	8
3			130	21
4			140	40
5	106	47	16	5
6	122	48	35	10
7			152	42
8	800	39	400	80 <sup>1</sup>
9			224	58 <sup>1</sup>

<sup>1</sup> Convergence criteria for the turbulent flow cases are not same.

\* IBM 3084 cpu seconds

solution of the continuity and momentum equations reduces the execution times by a factor of 3-5 compared with the SIMPLER algorithm. These findings are similar to those in earlier studies (Ref 10-12) where a lower-order convection-diffusion scheme was employed.

The combination of a coupled solution approach and an improved discretization scheme offers a twofold advantage over the use of a sequential approach with a lower-order discretization scheme. For comparable accuracy, an improved scheme requires fewer grid points than a lower-order scheme. In addition, on a grid

the use of a coupled solution approach reduces the execution times compared with the sequential solution algorithms. Thus, when the two are combined, a significant reduction in execution times results. The advantage is expected to increase at high Peclet numbers and on finer grids.

#### 5.4 PLANE-BY-PLANE MARCHING PROCEDURE FOR 3-D FLOWS

The coupled solution approach for fluid flow calculations presented previously in a two-dimensional context can easily be extended to three-dimensional flows. Such a procedure, however, will require a large amount of computer storage for LU factorization due to the increased number of nonzero elements in the coefficient matrix. These memory requirements are beyond the capacity of the currently available computers. Hence, an alternate strategy needs to be devised for the extension of the coupled solution approach to three dimensions. In the present study, the equations are solved in a plane-by-plane manner.

The predominant flow direction is selected as the marching direction. The equations in the planes normal to the marching direction are solved in a coupled manner using YSMP. There are two options available as to which variables should be solved simultaneously. The three velocity components and pressure can be solved in a coupled manner or only the cross-stream (in-plane) velocities and pressure are solved implicitly and the axial velocity is solved separately. The first approach involves more nonzero elements in the coefficient matrix and hence the cost of factorization is high. In the present implementation, the second approach has been followed; however, note that no comparative study was conducted to evaluate the performance of these two alternate strategies.

In the present plane-by-plane solution procedure, the treatment of in-plane velocities and pressure is identical to that in a two-dimensional problem. The additional features are related to the solution of the velocity component along the marching (axial) direction. It is necessary to ensure that the axial velocity component satisfies the axial momentum and continuity equations simultaneously. This has been accomplished by following the procedure described in Ref 25. The essential steps in this method are as follows.

The axial momentum equation for any cross-stream plane can be written as:

$$a_p U_p = \sum a_{nb} U_{nb} + b - \Delta v \left( \frac{\partial \bar{p}}{\partial x} \right) \quad (152)$$

where nb refers to the neighbors in the cross section and  $\Delta v$  is the volume of a control volume.

In equation (152), b includes the physical source, the net transport in the axial direction and the axial pressure gradient given by the currently available pressure field.  $(\partial \bar{p} / \partial x)$  is the correction that must be applied to the calculated pressure gradient so that the axial velocity field at any plane yields the correct cross-sectional flow rate M:

$$M = \int \rho U_p dA \quad (153)$$

The pressure gradient  $(\partial \bar{p} / \partial x)$  should be such that both equations (152) and (153) are simultaneously satisfied. This is accomplished as follows.

For a fixed set of coefficients, there is a linear relationship between  $U_p$  and  $(\partial p / \partial x)$ . At a given cross-sectional plane, equation (152) can be written as:

$$U_p = \hat{U}_p + d_p \left( \frac{\partial \bar{p}}{\partial x} \right) \quad (154)$$

The constants  $\hat{U}_p$  and  $d_p$  can be evaluated by solving equation (152) with two different values of  $(\partial \bar{p} / \partial x)$ . With known values of these parameters, the required pressure gradient is calculated by enforcing equation (153). That is

$$M = \int \rho U_p dA = \int \rho \hat{U}_p dA + \left( \frac{\partial \bar{p}}{\partial x} \right) \int \rho d_p dA \quad (155)$$

or

$$\left( \frac{\partial \bar{p}}{\partial x} \right) = \frac{M - \int \rho \hat{U}_p dA}{\int \rho d_p dA} \quad (156)$$

The final  $U$ -field is obtained by substituting the calculated value of  $(\partial \bar{p} / \partial x)$  in equation (154). The pressure values at all locations downstream of the plane under consideration are also corrected using the calculated pressure gradient.

The plane-by-plane solution procedure is supplemented by the solution of a three-dimensional pressure equation. This pressure field provides a means by which the elliptic effects are transmitted over the entire three-dimensional domain. In the present implementation, the pressure equation is identical to that in the SIMPLER algorithm. The pressure equation is solved after each sweep of the computational domain.

## 5.5 EVALUATION OF THE PLANE-BY-PLANE SOLUTION TECHNIQUE

The solution procedure described previously was applied to two model laminar flow problems. For these calculations, the Power-law differencing scheme was used. The flow situations considered are sketched in Figure 45. They are the following:

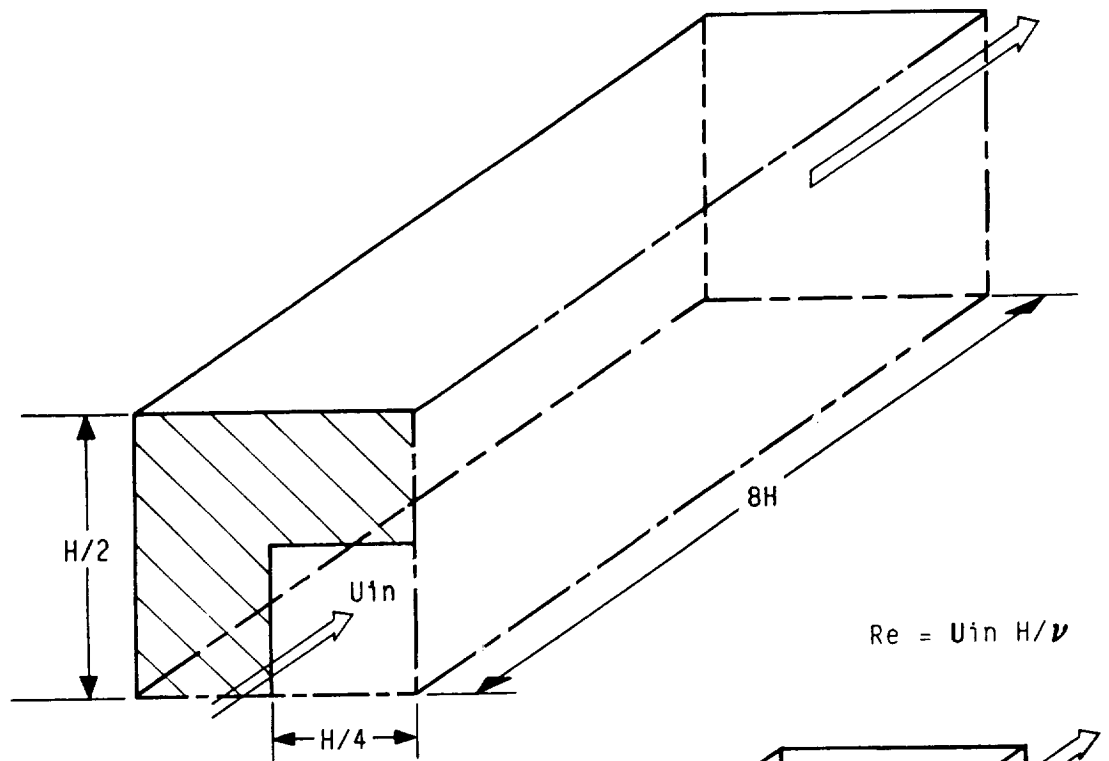
1. flow in a three-dimensional sudden expansion
2. flow in a rectangular box with a transverse jet

These situations represent, in a simplified manner, the flow in a gas turbine combustor.

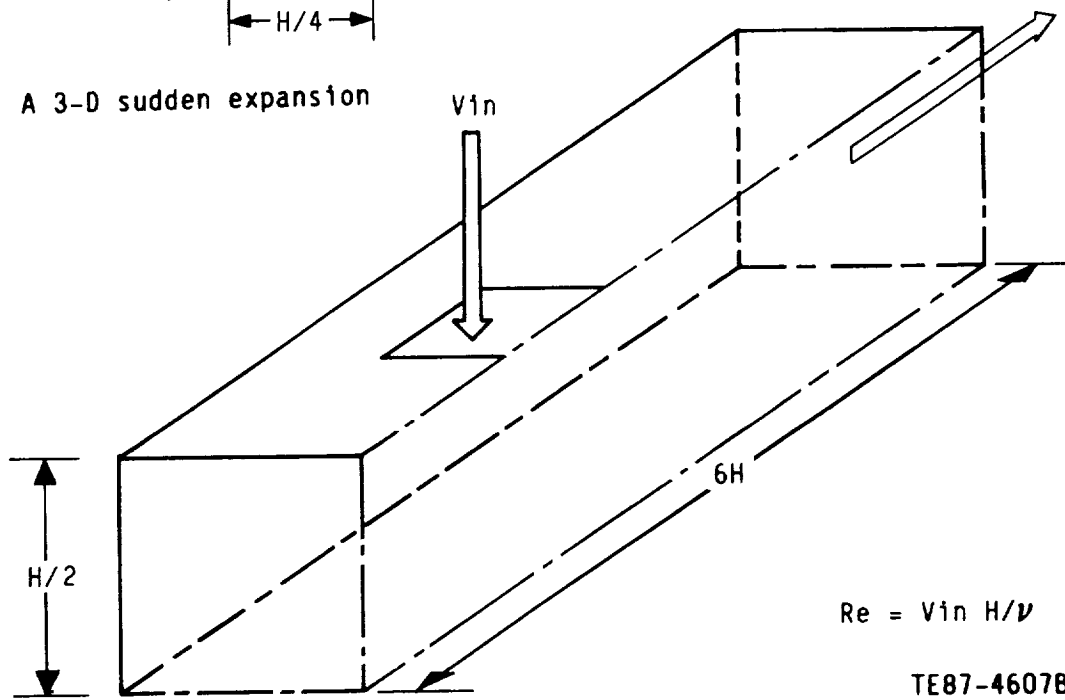
The calculations presented here were started from zero initial guess for the velocity components and pressure.

### 5.5.1 Three-Dimensional Sudden Expansion

For the flow in a three-dimensional expansion, a 4:1 area ratio is considered. Due to symmetry considerations, computations have been restricted to a quarter



a. A 3-D sudden expansion



b. A jet in a box

Figure 45. Test cases for 3-D flows.

section of the duct. Two values of Reynolds number, defined as  $Re = U_{in} H/\nu$ , of 100 and 1000 are considered. Figures 46a and 46b show the convergence rate of the solution procedure for Reynolds numbers of 100 and 1000, respectively, on a uniform  $22 \times 12 \times 12$  grid. In these figures the absolute sum of residuals at all internal points for each equation are plotted against the number of iterations, which refer to the number of sweeps of the computational domain.

#### 5.5.2 Flow in a Box with Transverse Jets

This flow was computed for a Reynolds number,  $Re = V_{in} H/\nu$ , of 500 using a uniform  $22 \times 12 \times 12$  grid. The convergence behavior of the solution procedure is shown in Figure 47.

Both the flow situations considered here involve significant recirculation zones similar to that in a gas turbine combustor. On the grid used, the plane-by-plane procedure leads to convergence in 10 to 15 iterations. This indicates that the proposed procedure is robust. This solution technique was also used for solving the 3-D jet in cross flow turbulent test case described in section 4.4.2 on the coarse grid. Again, convergence was achieved in about 20 iterations. In all these calculations the Power-law scheme was used.

### 5.6 COST COMPARISON

The plane-by-plane solution procedure is rapidly convergent and robust. A cost comparison with the iterative SIMPLER algorithm, however, revealed that the proposed procedure was not cost-effective, at least on the grids used. This high cost of solution is attributed to need to factorize the coefficient matrix at each cross-sectional plane, which is necessary to the rapidly changing nature of flow in the axial (marching) direction. Under specialized conditions, the factorized coefficient matrix at an upstream plane can be used for computations at a particular plane. Such a practice, however, cannot be used for a general flow.

### 5.7 NOTE ON THE USE OF FLUX-SPLINE SCHEME

The objective in this program was to combine the plane-by-plane strategy with the flux-spline scheme. Initial exploratory runs indicated that for sample problems considered, such a combination did not lead to convergence except on very coarse grids. It should be mentioned that no such difficulty was encountered in two-dimensional flows where all equations were treated in a fully coupled manner. The only new feature in three-dimensional flows is the use of the plane-by-plane solution strategy. It is therefore likely that the decoupling in the marching direction is responsible for the lack of convergence when the flux-spline discretization scheme is used.

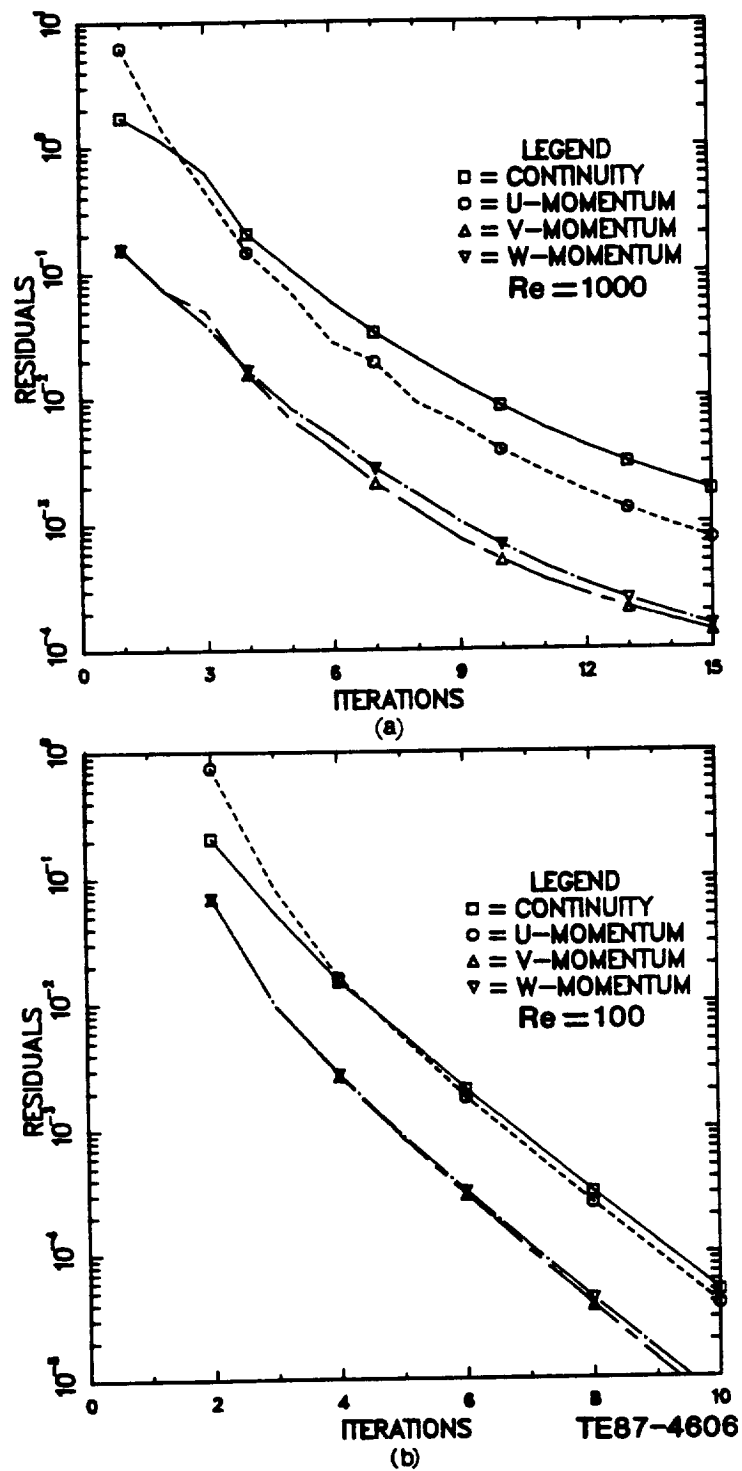


Figure 46. Rate of convergence for 3-D sudden expansion.

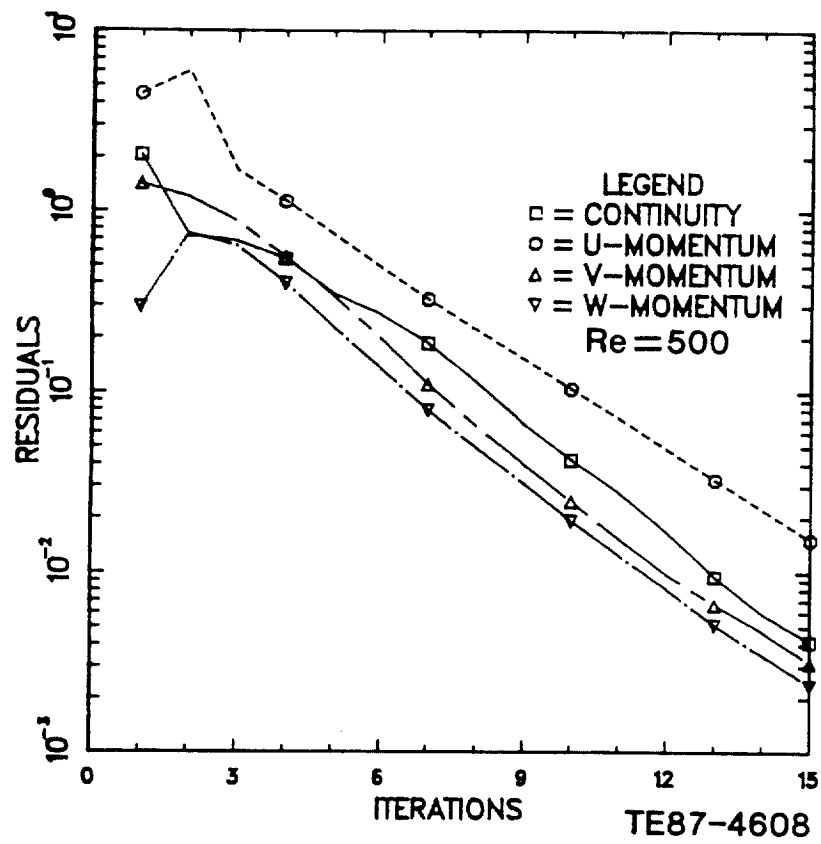


Figure 47. Rate of convergence for a jet in a rectangular box.

## VI. CONCLUDING REMARKS

### 6.1 SUMMARY OF THE PRESENT WORK

The objective of the present program was to develop accurate and efficient numerical schemes for predicting the flow field in gas turbine combustors.

To improve the numerical accuracy various discretization schemes available in literature were evaluated on the basis of several criteria. Three schemes, linear flux-spline, cubic flux-spline, and CONDIF, were incorporated into a computer program for two-dimensional flows and were used to solve a series of test problems. The test problems included scalar transport, laminar flows, and turbulent flows. The numerical solutions were compared with available analytical solutions, experimental data, or fine grid numerical solutions. For all problems considered, the linear flux-spline scheme was consistently superior to other schemes and was selected for incorporation in a computer program for three-dimensional flows.

The linear flux-spline scheme was used to solve several three-dimensional flows. For a given number of grid points, the flux-spline scheme produces results that are far superior to those from the (lower-order) Power-law differencing scheme. Further, it has the potential of providing a grid independent solution without requiring an excessive number of grid points.

To improve the computational efficiency of the overall solution procedure, a coupled solution approach for the fluid flow equations was adopted. In this approach, the discretized continuity and momentum equations are solved simultaneously using a sparse matrix inversion technique. The coupled approach, when used in conjunction with the linear flux-spline scheme, reduced the execution times by factors of 3 to 5 compared with the currently used sequential (SIMPLE-based) algorithms.

The memory restrictions of the present computers do not allow a coupled solution of all fluid flow equations in three-dimensional flows. To circumvent this difficulty, a plane-by-plane solution strategy was developed. In this procedure the cross stream velocities and pressure in a plane normal to the predominant flow direction are solved in a coupled manner and the streamwise velocity is solved separately. The plane-by-plane technique worked satisfactorily when used with the Power-law discretization scheme. However, convergence could not be attained with the flux-spline scheme except on very coarse grids. This aspect needs further consideration.

### 6.2 RECOMMENDATIONS FOR FURTHER WORK

The linear flux-spline scheme used in this work for majority of calculations is susceptible to spatial oscillations for highly convective flows on coarse grids. Such a behavior may cause difficulties when the scheme is used to discretize the transport equations of the "always positive" quantities such as the turbulence kinetic energy. It would be desirable to develop a bounded scheme that is free of the oscillations.

The CONDIF scheme performed satisfactorily except for the heat transfer problem in the shear driven cavity and turbulent flow over a backward facing step. The causes for this anomaly should be identified and the scheme should be

tested for more problems involving fluid flow. An attractive feature of CONDIF is its simplicity and ease of programming.

For the test problems considered here, the cubic flux-spline scheme performed very well. It should be extended to fluid flow equations.

The causes leading to the lack of convergence of the plane-by-plane solution strategy when used with the flux-spline scheme should be identified. In addition, the use of other solution algorithms, such as the multigrid techniques, should be explored.

## REFERENCES

1. Patankar, S. V., "Numerical Heat Transfer and Fluid Flow," Hemisphere, 1980.
2. Wong, H. H., and Raithby, G. D., "Improved Finite Difference Methods Based on a Critical Evaluation of the Approximation Errors," Numerical Heat Transfer, Vol 2, 1979, pp 139-163.
3. Varejao, L. M. C., "Flux-Spline Method for Heat, Mass, and Momentum Transfer," Ph.D. thesis, Department of Mechanical Engineering, University of Minnesota, 1979.
4. Nieckele, A. O., "Development and Evaluation of Numerical Schemes for the Solution of Convection-Diffusion Problems," Ph.D. thesis, Department of Mechanical Engineering, University of Minnesota, 1985.
5. Runchal, A. K., "CONDIF: A Modified Central-Difference Scheme for Convective Flows," International Journal for Numerical Methods in Engineering, Vol 24, 1987, pp 1593-1608.
6. Hassan, Y. A., Rice, J. G., and Kim, J. H., "A Stable Mass Flow Weighted Two-Dimensional Skew Upwind Scheme," Numerical Heat Transfer, Vol 6, 1983, pp 395-408.
7. Raithby, G. D., "Skew Upwind Differencing Scheme for Problems Involving Fluid Flow," Computer Methods in Applied Mechanics and Engineering, Vol 9, 1976, pp 153-64.
8. Leonard, B. P., "A Stable and Accurate Convective Modeling Procedure Based on Quadratic Interpolation," Computer Methods in Applied Mechanics and Engineering, Vol 19, 1979, pp 59-98.
9. Runchal, A. K., "Convergence and Accuracy of Three Finite-Difference Schemes for a Two-Dimensional Conduction and Convection Problem," International Journal for Numerical Methods in Engineering, Vol 4, 1972, pp 541-550.
10. Vanka, S. P., and Leaf, G. K., "A Fully Coupled Solution of Pressure-Linked Flow Equations," ANL-83-73, Argonne National Laboratory, IL, 1983.
11. Vanka, S. P., "Block Implicit Calculation of Steady Turbulent Recirculating Flows," International Journal of Heat and Mass Transfer, Vol 28, 1985, pp 2093-2103.
12. Braaten, M. E., "Development and Evaluation of Iterative and Direct Methods for the Solution of Equations Governing Recirculating Flows," Ph.D. thesis, Department of Mechanical Engineering, University of Minnesota, 1985.
13. Einsentat, S. C., Gursky, M. C., Shultz, M. H., and Sherman, A. H., "Yale Sparse Matrix Package II--The Non-Symmetric Codes," Research Report 114, Department of Computer Sciences, Yale University, 1977.
14. Haas, W., "Warmeubertragung in einer Kanalstromung mit Plotzlicher Querschnittserweiterung," Institut fur Hydromechanik, Sonderforschungsbericht 80, University of Karlsruhe Report, 1981.
15. Durst, F., and Pereira, J. F. C., "The Calculation of Some Steady Laminar Flows using Various Discretization Finite-Difference Schemes," Taylor, C., Olson, M. D., Gresho, P. M., and Habashi, W. (eds.), Numerical Methods in Laminar and Turbulent Flow, Proceedings of the Fourth International Conference, Swansea, 1985, pp 551-562.
16. Kline, S. J., Cantwell, B. J., and Lilley, G. M., (eds.), "The 1980-81 AFOSR-HTTM Stanford Conference on Complex Turbulent Flows," Stanford University, Vol I, II, and III.
17. Kim, J. J., "Investigation of Separation and Reattachment of a Turbulent Shear Flow: Flow over a Backward Facing Step," Ph.D. thesis, Stanford University, 1978.

18. Nallaswamy, M., "A Critical Evaluation of Various Turbulence Models as Applied to Internal Fluid Flows," NASA Technical Paper 2474, 1985.
19. Ku, H. C., Hirsch, R. S., and Taylor, T. D., "A Pseudo-Spectral Method for Solution of the Three-Dimensional Incompressible Navier-Stokes Equations," Journal of Computational Physics, Vol 70, 1987, pp 439-462.
20. Khan, Z. A., "Opposed Jets in Crossflow," Ph.D. thesis, Department of Mechanical Engineering, Imperial College, University of London, 1982.
21. Sturgess, G. J., "Calculation of Aerospace Propulsion Combustors--A View from Industry," in So, R. M. C., Whitelaw, J. H., and Mongia, H. C. (eds.), Calculations of Turbulent Reactive Flows, ASME AMD, Vol 81, 1986, pp 185-232.
22. Syed, S. A., Chiappetta, L. M., and Gosman, A. D., "Error Reduction Program," Final Report, NASA CR-174776, 1985.
23. Van Doormal, J. P., and Raithby, G. D., "Enhancement of the SIMPLE Method for Predicting Incompressible Fluid Flows," Numerical Heat Transfer, Vol 7, 1984, pp 147-163.
24. Issa, R. I., "Solution of the Implicitly Discretized Fluid Flow Equations by Operator-Splitting," Journal of Computational Physics, Vol 62, 1986, pp 40-65.
25. Raithby, G. D., and Schneider, G. E., "Numerical Solution of Problems in Incompressible Fluid Flow: Treatment of the Velocity-Pressure Coupling," Numerical Heat Transfer, Vol 2, 1979, pp 417-440.